Methods and Applications of Structural Health Monitoring on Bridges

BY

ELIAS ABDOLI OSKOUI
B.Sc. University of Tabriz, Tabriz, Iran, 2010
M.Sc. University of Tehran, Tehran, Iran, 2012

THESIS

Submitted as partial fulfillment of the requirements
for the degree of Doctor of Philosophy in Civil Engineering
in the Graduate College of the
University of Illinois at Chicago, 2019

Chicago, Illinois

Defense Committee:
Farhad Ansari, Chair and Advisor
Didem Ozevin
Eduard Karpov
Craig Foster
Danilo Erricolo, Electrical and Computer Engineering Department

I dedicate my thesis to my parents, Kazem and Parvin. No words can describe their unconditional love and endless support.

ACKNOWLEDGEMENTS

Firstly, I would like to express my sincere gratitude to my advisor, Professor Farhad Ansari, whose continuous support and encouragement made this journey possible for me. His immense knowledge in structural engineering and his patience and motivation always pushed me into coming up with new ideas and solutions during the course of my PhD studies. His mentorship taught me how to think critically and not to be afraid of thinking out of box.

I would like to thank Todd Taylor and Emad Norouzzadeh, my colleagues and friends who spent their valuable time with me in the fields for experimental test and instrumentations and brainstorming through ideas. Their insightful help and support made a big difference in my studies.

Finally, I would like to thank my dear committee members Dr. Didem Ozevin, Dr. Eduard Karpov, Dr. Craig Foster and Dr. Danilo Erricolo for always providing me with insightful comments and supports and taking their time to read my thesis as well as training me through the courses I have taken with them.

CONTRIBUTION OF AUTHORS

Authors' contributions in the below citation:

Abdoli Oskoui, E., Taylor, T., & Ansari, F. (2019). Method and monitoring approach for distributed detection of damage in multi-span continuous bridges. Engineering Structures, 189, 385-395. doi:10.1016/j.engstruct.2019.02.037

E. Oskoui proposed the method indicated in the paper for detection of micro cracks using BOTDA technology. T. Taylor was in charge of all of the instrumentation and experiments in the field and E. Oskoui help him with the field tests. All the calculation and preparation of tables and figures as well as the data analysis of the paper was performed by E. Oskoui. F. Ansari supervised and managed the process of analysis with E. Oskoui. F. Ansari was also in charge of all the coordination with authorities involved in experimental tests.

TABLE OF CONTENTS

CHAPTER PAGE

Chapter 1 . INTRODUCTION 1
1.1. Background 1
1.2. SHM Techniques 3
1.2.1 Local SHM techniques 3
1.2.1.1 Visual Inspection 3
1.2.1.2. Chain drag method 4
1.2.1.3. Coin tap test 4
1.2.1.4. Acoustic emission (AE) 5
1.2.1.5. Impact echo method (IE) 5
1.2.1.6. Ultrasonic pulse velocity (UPV) 6
1.2.1.7. Impulse response (IR) 6
1.2.1.8. Ground penetrating radar (GPR) 7
1.2.1.9. Electromagnetic conductivity 7
1.2.1.10. Half-cell potential 7
1.2.2 Global SHM techniques 8
1.3. Structural health monitoring sensors 10
1.3.1 Piezoelectric Sensors 10
1.3.2 Electromechanical Sensors 10
1.3.3 Fiber Optic Sensors 11
1.3.3.1 Fiber Bragg Grating (FBG) Sensors 14
1.3.3.2 Distributed fiber optic sensors 16
1.4. Application of fiber optic sensors 20
1.4.1 Bridge weigh in motion system 21
1.4.2 Application of distributed sensing using FOS 24
1.5. Research outline 27

Chapter 2 . METHOD AND MONITORING APPROACH FOR DISTRIBUTED DETECTION OF DAMAGE IN MULTI-SPAN CONTINUOUS BRIDGES 29
2.1. Introduction 29
2.2. Analytical Approach 30
2.3. Evaluation of the Method 38

2.3.1. Instrumentation 40
2.3.2. Static Load Tests 42
2.3.3. Finite Element Model 45
2.4. Results 46
2.5. Summary of the chapter 62

Chapter 3 . METHODS FOR MICRO-CRACKS DETECTION OF BRIDGES USING DISTRIBUTED SENSORS SUBJECTED TO DYNAMIC LOADS 64
3.1. Introduction 64
3.2. Method Introduction 65
3.3. Test Programs 71
3.3.1 Description of the bridges 71
3.3.1.1 Kishwaukee bridge 71
3.3.1.2 Thornton quarry bridge 72
3.3.2 Instrumentation 74
3.3.3 Dynamic load test 78
3.3.3.1 Kishwaukee bridge 78
3.3.3.2 Thornton quarry bridge 79
3.3.4 Finite Element Model 80
3.4. Test Results 80
3.4.1 Kishwaukee Bridge 80
3.4.1.1 Modal Shapes and Frequencies 80
3.4.1.2 Strain measurements 83
3.4.2 Thornton Quarry bridge 90
3.4.2.1 Strain measurements 90
3.5. Summary of the chapter 102

Chapter 4 . METHOD AND SENSOR FOR MONITORING WEIGHT OF TRUCKS IN MOTION BASED ON BRIDGE GIRDER END ROTATIONS 104
4.2 Methodology 104
4.2.1. Axle Spacing, Individual Axle Weights and GVW Calculation 106
4.2.2. Monitoring of Rotations Using the Rotation Sensor 111
4.2.2.1. Relating the end moments and forces to the center section strain 117
4.2.2.2. Temperature compensation of the rotation sensor 119
4.3. Calibration of the rotation sensor 120

4.4. Field Tests 122
4.4.1 Description of the Bridge 123
4.4.2 Sensors and Instrumentation 125
4.4.3 Test Program 129
4.4.4 Field Test Results 130
4.5. Summary of the chapter 137

Chapter 5 . CONCLUSIONS 138

CITED LITERATURE 141

APPENDIX 149

VITAE 150

LIST OF TABLES

TABLE PAGE

Table 1.1 FIBER OPTIC SENSORS TYPES AND TYPICAL PERFORMANCES 13

Table 2.1 DESIGNED LOAD CASES 44

Table 2.2 AVERAGE COMPUTED ERRORS (%) 56

Table 2.3 DAMAGE INDEX VALUES OF PROBABLE CRACK LOCATIONS 59

Table 4.1 CALIBRATION TRUCKS AXLE WEIGHTS 130

Table 4.2 VALIDATION RESULTS OF THE TEST TRUCKS FOR FIRST AXLES 132

Table 4.3 VALIDATION RESULTS OF THE TEST TRUCKS FOR SECOND AXLES 133

Table 4.4 VALIDATION RESULTS OF THE TEST TRUCKS FOR THIRD AXLES..... 134

Table 4.5 VALIDATION RESULTS OF THE TEST TRUCKS FOR GROSS VEHICLE WEIGHTS 135

Table 4.6 AXLE SPACING AND SPEED DETECTION RESULTS 136

LIST OF FIGURES

FIGURE PAGE

Figure 1.1 Classifications of fiber optic sensors 12

Figure 1.2 Reflected wavelength in Fiber Bragg Grating 15

Figure 1.3 Multiplexing in FBG sensors 16

Figure 1.4 Neubrescope 6055 device 20

Figure 2.1 Moment influence line of point Pi 33

Figure 2.2 Theoretical strain profile for point Pi due to a specific truck load 34

Figure 2.3 Measured strain profile for point Pi due to truck load 36

Figure 2.4 Kishwaukee River Bridge – Southbound 39

Figure 2.5 Plan and elevation views of the Kishwaukee bridge (units in meter) 39

Figure 2.6 Sectional view of the Kishwaukee River bridge (units in meter) 40

Figure 2.7 Location of the glued optical fiber on the section 41

Figure 2.8 PPP-BOTDA device at the Bridge site (Neubrescope NBX-6055) 42

Figure 2.9 Axle configuration of the calibrated truck 43

Figure 2.10 Typical loading locations of position 2 in all cases 45

Figure 2.11 Three dimensional finite element view of the Kishwaukee River bridge 46

Figure 2.12 Sectional view of the finite element model of the Kishwaukee River bridge 46

Figure 2.13 BOTDA strain measurement comparison with FEM for Case 1 – Position 1 47

Figure 2.14 BOTDA strain measurement comparison with FEM for Case 1 – Position 2 48

Figure 2.15 BOTDA strain measurement comparison with FEM for Case 1 – Position 3 48

Figure 2.16 BOTDA strain measurement comparison with FEM for Case 1 – Position 4 49

Figure 2.17 BOTDA strain measurement comparison with FEM for Case 1 – Position 5 49

Figure 2.18 BOTDA strain measurement comparison with FEM for Case 2 – Position 1 50

Figure 2.19 BOTDA strain measurement comparison with FEM for Case 2 – Position 2 50

Figure 2.20 BOTDA strain measurement comparison with FEM for Case 2 – Position 3 51

Figure 2.21 BOTDA strain measurement comparison with FEM for Case 2 – Position 4 51

Figure 2.22 BOTDA strain measurement comparison with FEM for Case 2 – Position 5 52

Figure 2.23 BOTDA strain measurement comparison with FEM for Case 3 – Position 1 52

Figure 2.24 BOTDA strain measurement comparison with FEM for Case 3 – Position 2 53

Figure 2.25 BOTDA strain measurement comparison with FEM for Case 3 – Position 3 53

Figure 2.26 BOTDA strain measurement comparison with FEM for Case 3 – Position 4 54

Figure 2.27 BOTDA strain measurement comparison with FEM for Case 3 – Position 5 54

Figure 2.28 BOTDA strain measurement comparison with FEM for Case 4 – Position 1 55

Figure 2.29 BOTDA strain measurement comparison with FEM for Case 4 – Position 2 55

Figure 2.30 BOTDA strain measurement comparison with FEM for Case 4 – Position 3 56

Figure 2.31 Damage Index for each load case 58

Figure 2.32 Detected crack in the fifth span (point 5) 60

Figure 2.33 Detected crack in the third span corresponding to point 4 61

Figure 2.34 Connection joints corresponding to points 1, 2 and 3 61

Figure 2.35 Elevation difference in connection joints 62

Figure 3.1 Example of distributed strains in distance and time domain 67

Figure 3.2 Kishwaukee River Bridge - Southbound 72

Figure 3.3 Thornton Quarry bridge 73

Figure 3.4 Cross section of the Thornton Quarry bridge 73

Figure 3.5 Location of the glued optical fiber on the Kishwaukee bridge 75

Figure 3.6 Installation of optical fiber on the Kishwaukee bridge 75

Figure 3.7 Initial setup for installation of optical fiber on the Thornton Quarry bridge 76

Figure 3.8 Installation of optical fiber on the Thornton Quarry bridge 77

Figure 3.9 Location of the glued optical fiber on the Thornton Quarry bridge 78

Figure 3.10 Calibrated truck 79

Figure 3.11 Modal shapes and frequencies of Kishwaukee bridge 81

Figure 3.12 Fast Fourier Transform of the first accelerometer 82

Figure 3.13 Fast Fourier Transform of the second accelerometer 82

Figure 3.14 Fast Fourier Transform of the third accelerometer 83

Figure 3.15 Distributed strain data of the Kishwaukee bridge over time 84

Figure 3.16 Sectional stresses under truck axle (kPa) 85

Figure 3.17 Filtered distributed strains of the entire bridge in time 86

Figure 3.18 Linear regression formula for load path derivation 87

Figure 3.19 Strain sets while the trucks are located at the middle of each span 88

Figure 3.20 Crack index for all the sampling points along the bridge 88

Figure 3.21 Detected crack in the fifth span (point 4) 90

Figure 3.22 Filtered distributed strain profile of the deck for run number 5 91

Figure 3.23 Filtered distributed strain profile of the bottom flange for run number 5 92

Figure 3.24 Strain diagram of the cross section 94

Figure 3.25 Variances of strains differentials through time along the deck for run 1 95

Figure 3.26 Variances of strains differentials through time along the deck for run 2 96

Figure 3.27 Variances of strains differentials through time along the deck for run 3 96

Figure 3.28 Variances of strains differentials through time along the deck for run 4 97

Figure 3.29 Variances of strains differentials through time along the deck for run 5 97

Figure 3.30 Variances of strains differentials through time along the deck for run 6 98

Figure 3.31 Variances of strains differentials through time along the deck for run 7 98

Figure 3.32 Variances of strains differentials through time along the deck for run 8 99

Figure 3.33 Detected micro-cracks on the surface of the deck 100

Figure 3.34 Detected micro-cracks on the surface of the deck 101

Figure 3.35 Detected micro-cracks on the surface of the deck 102

Figure 4.1 Deflection of a simple span beam due to a point load 105

Figure 4.2 Rotational influence line of support at j 106

Figure 4.3 Bridge weigh in motion calculation steps 108

Figure 4.4 Rotation Sensor and FBG locations 112

Figure 4.5 Rotation Sensor Layout 113

Figure 4.6 Curved member with positive moments and forces 114

Figure 4.7 Cycloidal arch form 116

Figure 4.8 Rotation sensor displacements and free half-body diagram 118

Figure 4.9 Rotation sensor calibration setup 121

Figure 4.10 Rotation sensor calibration results 122

Figure 4.11 The subject bridge located in LaGrange, GA 124

Figure 4.12 Bridge elevation and sectional view 125

Figure 4.13 Rotation sensor installed on the bridge 126

Figure 4.14 Rotation and wheel sensors 127

Figure 4.15 Location of wheel sensors 128

Figure 4.16 Site interrogation unit and processor within the NEMA enclosure 129

Figure 4.17 Recorded data from rotation and wheel sensors for a passing truck 131

SUMMARY

Civil engineering infrastructures such as bridges are subjected to deterioration and damage throughout their service life due to aging of construction materials, oversized loading, fatigue, harsh climate conditions and excessive usage. Maintaining a safe and reliable infrastructure is essential for an operational transportation system. Structural health monitoring (SHM) as a fast developing field in the civil engineering world has provided the means to effectively assess the condition of the structures and investigate their behavior under various scenarios. Condition assessment of the civil engineering infrastructures can be divided in to two steps; Determination of applied loads on the structures, and assessment of the structural behavior under the measured loads. The invention of fiber optic sensors provided the opportunities for large scale structural health monitoring resulting in assessment of the severity of the applied loads and structural response to the respective loads.

In this research, application of fiber optic sensors in structural load determination in addition to damage assessment of superstructures has been investigated. In the first phase, an approach for distributed damage detection along the entire length of multi-span continuous bridges of various constructions is introduced. This method is based on monitoring the distributed strains measured by the Brillouin scattering based optical fiber sensing technology. Identification of enhanced strains corresponding to the cracked regions beyond signal to noise ratio limits is accomplished by normalization of measured and theoretical strains differentials. A damage index for identification of microcracks is

then introduced based on the formulation of the method. Validation of the proposed method is achieved by static load testing of a five span prestressed and post tensioned box girder concrete bridge. Visual inspection is used to located and verify the location of probable micro cracks detected by the proposed method. The method is further developed for the experiments subjected to dynamic loading. Incorporation of dynamic loads into the formulation of the proposed method enables the micro crack detection of structures using regular traffic loads without lane closures. Two bridges were experimented for verification purposes under dynamic loads and visual inspection was also performed after the probable crack locations were indicated.

The final stage of this research pertains to the development of a new bridge weigh in motion system for assessment of dynamic loads applied to the bridge. The proposed method is based on measurement of bridge abutment rotations and its correlation to the passing truck loads by means of rotational influence lines. Measurements of changes of girder rotations at the abutments are achieved by introducing a new rotation sensor. This sensor is an FBG based fiber optic sensor that correlates the changes of wavelength in the Bragg grating of the sensor to the rotational displacements of the sensor ends. The rotation sensors are then utilized in the BWIM system for individual axle weight detection in addition to GVW and truck speeds. Applicability and verification of the proposed system were put into test by a series of experiments on a four-span steel girder bridge and the accuracy of the system was evaluated by comparison of individual axle weights and gross vehicle weights of multiple calibrated trucks weighed at a nearby weighing station.

Chapter 1 . INTRODUCTION

1.1. Background

Inspection and testing the performance of structures such as bridges and dams have been achieved since larger structures have been constructed by humans. Airplane and space industry are where Structural Health Monitoring (SHM) has been originated. The idea is based on the continuous monitoring of the behavior of vital mechanical parts and get early warnings for maintenance depending on the problem's severity. Structural health monitoring in civil engineering field is a relatively new phenomenon. However, decreasing cost of sensors and latest developments in technologies have made SHM more appealing in civil engineering applications.

One of the main goals of the structural health monitoring in civil engineering is to investigate the development of specific structural response or parameters, depending on the type of loads applied to the structure. Examples of these parameters are forces, stresses, rotations, displacements and strains. Environmental parameters can also influence the response of the structures such as temperature, humidity, wind and traffic (Aktan et al 2003). Maintaining reliable performance of bridges as key components of transportation infrastructures also play an important role for economic growth and safety of commuters. According to a report from US Federal Highway Agency (FHWA), 15 percent of around 595,000 bridges in unites states are rated as structurally deficient and they need to be repaired (Wardhana and Hadipriono 2003; Spencer and Cho 2011; Yi et al 2013). In addition to safety issues, degradation of infrastructures like bridges decreases the service quality and increases costly repairs, replacements and generally infrastructure

maintenance. Therefore, it is important to ensure that these infrastructures are maintained well and proper function of them is the priority to avoid major failures. To accomplish this, it is vital to monitor and inspect structures frequently with optimum efficiency.

Frequency of health monitoring of structures are categorized in four groups. Short-term monitoring, long-term monitoring, periodic and triggered monitoring. The selected strategy is dependent on the parameter of the structure to be studied. For example, if the formation of cracks in the structure are the main concern, long term monitoring is suggested. However, damping of the structures is of concern, short term or manually triggered monitoring is enough. Short term monitoring can be utilized if the structure is needed to be examined at a specific point of time. Examples of applicability of short term monitoring are changes of traffic loads, changes of structural system and rehabilitation of structure.

Mufti el al (2006) stated that a structural health monitoring is considered to be long term if the monitoring is carried over a period of years to decades. Preferably, long-term monitoring should be conducted over the life time a structure. Recent development of sensor technology, acquisition systems and processing units have enabled the researchers to carry out long-term monitoring over the life span of structures.

While the frequency of the health monitoring is important, strategies to move forward with it make an important role for performance evaluation of structures. Monitoring strategies fall into two groups of local structural health monitoring and global structural health monitoring.

1.2. SHM Techniques

Structural health monitoring of infrastructures such as bridges can be categorized into two main groups: local health monitoring and global health monitoring. Global health monitoring refers to the techniques that only detect the existence of damages or cracks, however, local health monitoring identifies, severity and location of the damage in structures (Chang et al, 2003). Both local and global structural health monitoring methods are essential and important for reliable operation of structures.

1.2.1 Local SHM techniques

Nod-destructive testing (NDT) and non-destructive evaluation (NDE) of structures offer assistance to engineers to effectively monitor and examine the aging structures. These methods are utilized for detection of damage and are used in local structural health monitoring (Chang et al, 2003). Furthermore, NDT can be used to prevent unpredictable failure of various structures. Many researchers have written guidelines for these methods in structural evaluation (Rens et al, 1997; Hola et al, 2010)

1.2.1.1 Visual Inspection

One of the most popular and useful non-destructive methods for inspection of visible surfaces is visual inspection. However, the efficiency of this method relies on the knowledge and experience of the inspectors which includes structural materials and construction. This method is most commonly utilized for monitoring of cracks and damages in reinforces concrete structures (Park et al 2001; Estes and Frangopol 2003). This method is considered to be the preliminary stage through evaluating reinforced

concrete structures. Visual inspection is a fast method for detecting superficial damages. It is a considered to be a cheap and quick technique, however it never offers quantitative and detailed information about the extent of the damage in the structure. This method is generally used to identify cracking, spalling, element delamination, reinforcement corrosion and concrete deterioration (Kilic 2014). Some of the tools used in this method are stereo microscopes, borescopes and magnifiers.

1.2.1.2. Chain drag method

This method is utilized to detect the spalled regions of the deck of reinforced surfaces (Scott 2003). For this method to work in the first stage a mesh is drawn on the surface of the deck then a chain is dragged over the indicated surface. The areas corresponding to hollows are sound differently. These areas are then indicated as delaminated regions (Barnes and Trottier 2000)

1.2.1.3. Coin tap test

This test is the most simplified form of impulse echo method. Coin tap test as one of the oldest techniques of nondestructive testing methods is used for crack detection of concrete structures (Cawley and Adams, 1988). This technique was mostly used in United Kingdom for detection of defects through tunnel lining. In the application of bridges or walls, when the surface is hit by coin or a hammer which is lightweight, an echo is heard. If the response or the echo is significantly different, it might be an indication of cavity in that region of the structure. Since human ears are sensitive to changes of frequency of sound, this method can be used as a cheap technique for a rapid investigation.

1.2.1.4. Acoustic emission (AE)

Acoustic emission method is utilized for detection of defects or damages in infrastructures specifically in transportation industry (Rens et al, 1997; Holford et al, 2001). This technique is used in three different categories including detection of damage areas, location of the damage source and the severity of the defect (Holford et al 2001). The method is capable of detection the location of the damage automatically. This feature of the method distinguishes the AE among other NDT methods. Transient elastic waves are the basics of acoustic emission method. These waves are generated from quick release of energy due to internal cracks and are received by transducers installed on various location of the monitored structure. Based on the differences in times of arrival to the transducers, the location of the crack or damage in the structure is revealed.

1.2.1.5. Impact echo method (IE)

Impact echo method is one the common methods used in detection of cracks and determination of deck thickness in reinforced concrete structures. It is a stress wave based method. The stress pulse which is passed through the structural material with a specific speed, generates waves such as surface waves, shear waves and P waves. These waves are then reflected by internal layers of defects in the structure. Multiple transducers are installed on the surface of the structure to receive the reflected waves form the internal damaged areas. To convert the signal from time domain to frequency domain, the fast Fourier transform is utilized on the signal. Following formula is then used to calculate the location of the crack (Scott et al, 2003):

$$T = C_p/2f \quad (1.1)$$

In this formula, T is the location of the crack, f is the frequency of the wave and C_p is the speed of the P or compression wave.

Grosse et al. 2013, developed a new idea for impact echo method. They illustrated that this method has capabilities of detecting concrete structures thickness and relatively large holes in the structure accurately. Sensitivity of IE method to various parameters such as slab thickness was investigated by Azari et al. (2014) and it was depicted that the method is affected by the slab panel dimensions.

1.2.1.6. Ultrasonic pulse velocity (UPV)

This method is considered to be one of the main techniques in non-destructive testing methods for investigating concrete condition. This is achieved by measuring the traveling time of ultrasonic wave in the defined path. UPV method can be utilized to localize the defected areas in the structural member (Azari et al. 2014). Ultrasonic pulse velocity device includes two transducers. One transducer is dedicated for transmitting the signal and the other transducer is designed for receiving the signal. Once the signal is sent by the first transducer, it penetrates in the concrete and it is then received by the second transducer. As the propagated waves reach to a defect or crack, a portion of the emitted energy is returned to the surface. Identification of damages are achieved by evaluating the anomalies in the acoustic impedance.

1.2.1.7. Impulse response (IR)

Impulse response method is used to detect anomalies in deep foundations. Compressive waves are emitted through the concrete when the hammer hits the surface

of the element. Frequency of these waves can vary between 0 to 3000 Hz based on the material of the hammer. Load cells measure the force generated by hammer and receivers measure the speed of the waves.

1.2.1.8. Ground penetrating radar (GPR)

Ground penetration radar method is the most famous among NDT methods for detection of damages and anomalies in bridge decks (Alani et al. 2013). This method is utilized in health monitoring of reinforced concrete structures, such as bridges, tunnels and buildings (Cruz et al 2010). Ground penetration radar is considered to be a fast method for investigation the multiple layers of structures and for detection of defects and damages in the structures (Yehia et al 2007). The capability of the method extends to identifying thickness of layer, diameter of reinforcement and strain induced deformations (Maser and Roddis 1990)

1.2.1.9. Electromagnetic conductivity

This method provides electrical and geometrical information about the testing materials. Damages in the concrete is identified by changes in conductivity (Garboczi et al. 1995)

1.2.1.10. Half-cell potential

This technique is used for investigating the corrosion in the reinforcements of concrete structures (Elsener et al. 2003)

1.2.2 Global SHM techniques

One of the main techniques in the global health monitoring of structures is vibration testing. This method is used by many researchers to investigate the condition on infrastructures such as bridges (Ismail et al 2011; Hashim et al 2013). Vibration tests are conducted by subjecting the structure under forces and recording the response of the structure by transducers (Salawu 1997). Modal parameters such as modal shapes, modal frequencies and damping of the structure are usually measured in global structural health monitoring using vibration testing. If the structure is damaged, the modal parameters change. Therefore, changes of modal frequencies can be an indication of damage in the structure. It should be noted that, location, severity and type of damage directly influence the changes in modal parameters. Vibration testing includes forced and ambient vibration methods. No control is on the applied load or forces in the ambient vibration experiments (Hashim et al 2013). However, applied loads on the structure is controlled in the forced vibration tests.

Brownjohn et al (2011) investigated the vibration based technique for monitoring civil engineering structures. Dynamic performance of the infrastructures are studied in Vibration based monitoring or VBM method. This technique provides the information for the next stage of structural investigation called vibration based damage detection techniques. Detection of degradation in properties of materials and changes in support conditions can be detected in addition to modal parameters in this method. Vibration based tests are not relatively expensive and are easy to be performed.

Robert-Nicoud et al. (2005) developed a calibration method based on the structural behavior. This method takes into account of material characteristics and support boundary conditions. Gentile (2006) introduced a method based on dynamic assessment by utilizing ambient vibration tests and applied them to reinforced concrete bridges. Modal frequencies and modal shapes were calculated using dynamic experiments by Brencich and Sabia (2008). Brick material characteristics were investigated by conducting compressive tests. By using ambient and forced vibration testing, dynamic parameters were also developed in these experiments.

Bedon and Morassi (2014) investigated the effect of harmonically induced forced vibrations on a two-span post-tensioned concrete bridge which is located in Italy with high seismic activity. Low level excitations with a series of forced-based vibrations which were applied to the structure were used to carry out the frequency response function (FRF). Subsequently, bridge's acceleration response was calculated and the FRF was determined based on acceleration time histories.

Latest developments of vibration testing of structures were reviewed by Cunha et al (2013). They showed that there are some disadvantages to forced vibration testing when it is applied to long span bridges. Exciting the natural modal frequencies of these structures with low range frequencies of adequate energy were the source of the problem. However, development in technology makes it easier these days to measure low levels of dynamic response due to ambient vibrations like traffic loads accurately. Ambient and forced vibration tests can be applied during every stage of structures including construction and retrofitting stage.

1.3. Structural health monitoring sensors

Advanced structural health monitoring sensors include Piezoelectric Sensors, Electrochemical Sensors and Fiber Optic Sensors. A brief introduction to these sensors with an emphasis on fiber optic sensors are provided in the next few sections.

1.3.1 Piezoelectric Sensors

Piezoelectric sensors are used in numerous applications of civil engineering. These sensors can measure the changes in structural parameters such as strain, force, temperature and pressure. The measured parameters are then converted to readable electrical charge. Electrical energy can be transformed into mechanical energy and vice versa by piezoelectric materials. These materials can function as different roles such as sensors, transducer, and actuators. As an example, passive acoustic emission methods and piezoelectric sensors can be utilized for detection of cracks which generate stress waves through impulsive energy release (Dumoulin et al 2014; Qin et al. 2010). There are multiple piezoelectric materials including ceramics, composites and polymers. The most common used material is ceramic type in piezoelectric sensors. Their behavior under various temperatures are stable and they can bear up to 350 degrees of Celsius without giving up any conversion capacity between mechanical and electrical energy.

1.3.2 Electromechanical Sensors

There are three main electromechanical sensors including conductometric, aerometric and potentiometric sensors. The response of these sensors is related to the

quantity or composition of a specific element, ion of particular chemical element (Stradiotto et al 2003).

The quality of measurements is directly related to the stability of reference electrode in electromechanical sensors. Cheap sensors are no reliable in this matter and their performance can change over time, however, sensors like ERE20 are expensive. These sensors are popular in monitoring of corrosion in reinforced concrete structures. An example of electromechanical sensors application in SHM of civil engineering structures is the open circuit measurement which measures electromechanical potential between a reference electrode and sacrificial working electrode (Duffo and Farina 2009).

1.3.3 Fiber Optic Sensors

The invention of fiber optic sensors provided the opportunities for large scale structural health monitoring. Fiber optic sensors have been widely used as means of structural health monitoring (Ansari 2009; Glisic and Inaudi 2010). These sensing technologies have several advantages like being immune to electromagnetic fields, low signal to noise ratio and delivering low signal loss which enables long distance and therefore remote monitoring. It was illustrated that optical fiber sensors are relatively more expensive to be used in structural health monitoring while they can provide better and more reliable approaches where it is required. In a situation where the structural health monitoring is performed to save lives or prevent a catastrophic event, expenses can be of no concern. In commercial applications where the optical fiber sensors are utilized in multiple locations, the use of sensors can then be cost effective. Fiber optic sensors can be used in the applications where the only solution is a long term monitoring system.

Figure 1.1 classifies fiber optic sensors based on their measurement principles and table 1.1 depict a summary of various types of fiber optic sensors and their performances (Glisic and Inaudi 2007).

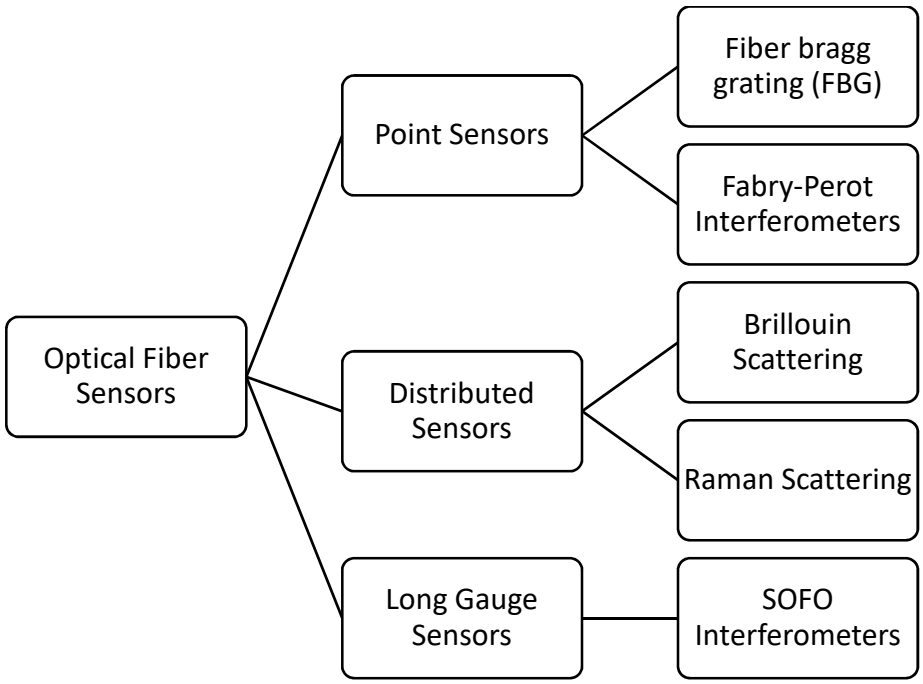

Figure 1.1 Classifications of fiber optic sensors

Table 1.1 FIBER OPTIC SENSORS TYPES AND TYPICAL PERFORMANCES

		Point sensors		Long gauge	Distributed Sensors	
		Fabry-Perot interferometric	**Fiber Bragg Grating**	**SOFO Interferometers**	**Raman Scattering**	**Brillouin Scattering**
Measurable Parameters		Strain	Temperature	Deformation	Temperature	Temperature
		Temperature	Acceleration	Strain		Strain
		Pressure	Water Level	Tilt		
				Force		
Multiplexing type		Parallel	In line and Parallel	Parallel	Distributed	Distributed
Number of measurement points		1	10-50	1	10000	30000
Typical Accuracy	**Strain (με)**	1	1	1		20
	Displacement (μm)	100	1	1		
	Tilt (μrad)			30		
	Temp (C)	0.1	0.1		0.1	0.2
	Pressure (% full scale)	0.25				
Range				20 m gauge	8 km	30-150 km
Fiber Type		Multi Mode	Single Mode	Single Mode	Multi Mode	Single Mode

1.3.3.1 Fiber Bragg Grating (FBG) Sensors

Point or discrete sensors have been widely utilized in structural health monitoring. They are fabricated in two main groups, Fiber Bragg grating (FBG) and Fabry-Perot interferometric. Fiber Brag Grating sensors provide better resolution and performance because of their capability of multiplexing. They can line up and installed in one line of fiber in addition to giving out higher strain resolutions. Periodic alterations in the refraction index of optical fiber's core create the Bragg Grating in the sensor. This process is finalized by exposing the fiber to an intense UV light which created these alterations. When the tunable light is emitted through the optical fiber with grating, all of the wavelengths of the light passes throughout the fiber except the wavelength matching with the grating pitch specific wavelength. Therefore, based on the reflected wavelength which is recorded by the data acquisition devices, measurement of induced strains or temperatures can be possible through the grating technology (Glisic and Inaudi 2007). Figure 1.2 illustates the bragg grating in the optical fiber and the reflected wavelength.

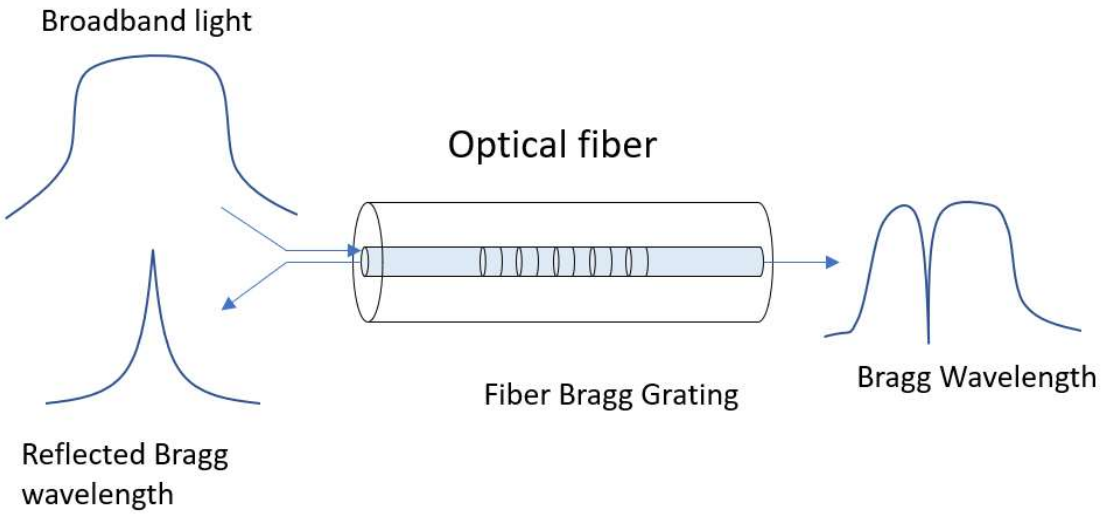

Figure 1.2 Reflected wavelength in Fiber Bragg Grating

Bragg grating wavelength is defined as follows:

$$\lambda_B = 2n_{eff}\Lambda \tag{1.2}$$

Where λ_B is the Bragg Grating wavelength, n_{eff} is the effective refraction index and Λ is the period of grating. The shift of wavelength is changes directly with respect to temperature and induced strains. Multiplexing is one of the main features of the FBGs. This capability enables to use multiple strain sensors in one channel of interrogator which is shown in figure 1.3. However, it should be noted that the sensors installed in one line of fiber in a channel should not inherit the same grating wavelength.

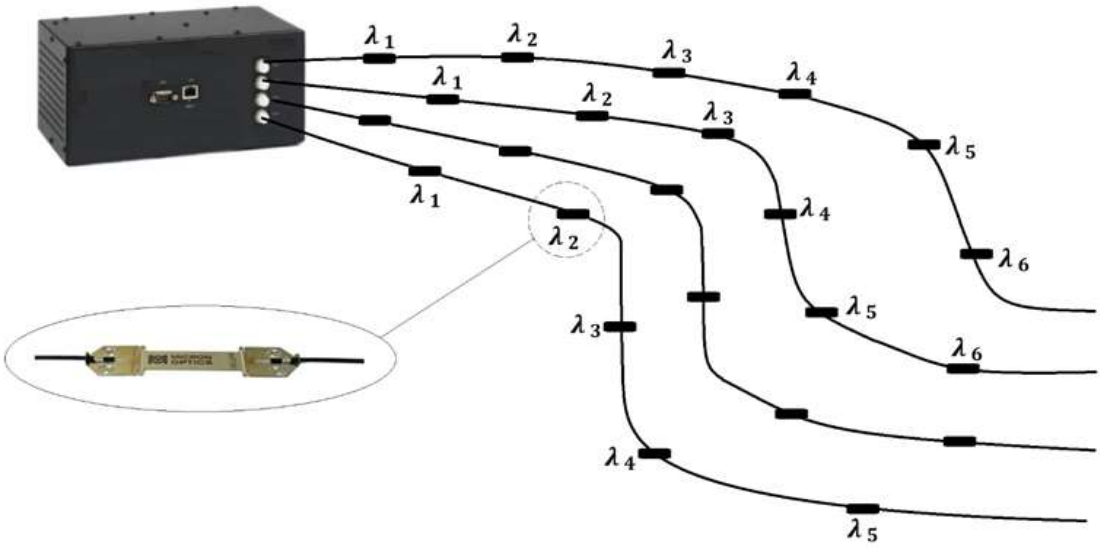

Figure 1.3 Multiplexing in FBG sensors

1.3.3.2 Distributed fiber optic sensors

In structural health monitoring, location of cracks, buckling and extensive deformations are often unknown, and it is almost impossible to install FBGs or strains gauges without prior knowledge of damaged locations. Therefore, distributed fiber optic sensors can be an excellent replacement in providing continuous data in a spatial domain instead of point and FBG sensors. Distributed fiber optic sensors are mostly suitable for large-scale structures like bridges, oil and gas pipelines and dams. Since the optical fiber itself is the sensor in the distributed sensing technology, any fluctuation and disturbance in the structure along the fiber is recorded. A single line of an optical fiber in distributed sensing technologies can overcome disadvantages of FBGs such as a multitude of sensors needed in an installation, high labor costs and huge amount of data for analysis.

Distributed sensing technology measures temperature and strains along the entire length of the installed optical fiber with range of measurements close to 30 kilometers. The spatial resolution defined in the distributed sensors varies based on the interrogating technology and usually is set between 2 cm to 1 meter with the strain measurement accuracy of 5 to 10 micro strains.

Distributed optical fiber sensors are fabricated based on the various scattering effects such as Raman, Rayleigh and Brillouin. Brillouin based optical fiber sensors achieve higher performance practically since measurements over 100 km is possible with an acceptable spatial resolution with this technology (Bao 1993). The phenomenon of Brillouin scattering is generated when the injected light through the optical fiber interacts with the density changes of the core due to external strains of the optical fiber which results in a shift in the frequency of the injected light (Motamedi et al. 2012).

Strain and temperature variations in a single mode optical fiber is proportional to the Brillouin frequency shift (BFS) of the fiber. Therefore, distributed measurements of strain and temperature simultaneously is made possible with this technology. The shifts in frequencies have linear relationships with strain and temperature in the fiber. These relationships are provided as

$$\nu_B(T_r, \varepsilon) = C_s(\varepsilon - \varepsilon_r) + \nu_{Br}(T_r, \varepsilon_r) \tag{1.3}$$

$$\nu_B(T, \varepsilon_r) = C_T(T - T_r) + \nu_{Br}(T_r, \varepsilon_r) \tag{1.4}$$

Where C_s and C_T = strain and temperature coefficient respectively; T_r and ε_r are temperature and strain related to a reference Brillouin frequency, ν_{Br}.

There are multiple analysis methods generated from the Brillouin phenomenon such as Brillouin Optical Time Domain Reflectometry (BOTDR), Brillouin Optical Time Domain Analysis (BOTDA), Brillouin Optical Frequency domain analysis (BOFDA) and Brillouin optical correlation domain analysis (BOCDA).

Convolution of pump and probe waves in every sampling point along the fiber is used for measurements in BOTDA technology. Spatial resolution (SR) of the BOTDA technology relies on the duration of the pump signal. T stimulate enough photons for strain and temperature measurements, the duration of the emitted pump signal needs to be more than 10 nano-seconds which puts a limitation on the spatial resolution of the BOTDA to be 1 meter (Bao and Chen 2011). It was concluded that the spatial resolution of one meter is not accurate enough for detection of micro crack locations in large structures (Feng et al. 2013). A newer version of BOTDA known as Pulse-Pre pump Brillouin Optical Time Domain Analysis or PPP-BOTDA was developed which employs a pulse shaped signal that leads to an enhanced data acquisition with smaller spatial resolutions for longer distances (Kishida et al. 2005a; Kishida et al. 2008). Moreover, Raman distributed amplification-BOTDA (Angulo 2012), Self-heterodyne-BOTDA (Zornoza 2012) and Simplex coded-BOTDA (Taki 2013) have been developed to increase the measurement distances. With the developments of BOTDA methods such as PPP-BOTDA, it was possible to achive smaller spatial resolutions with the accuracy of centimeters over 1 km of monitoring distances (Kishida et al. 2009).

A new BOTDA technique was developed recently by Li et al (2010) and was referred to as Amplitude Transfer (AT) BOTDA. This method is capable of dynamic measurements of strain and temperature. By the new technique, measurement of single

frequency was enough for the estimation of central frequency of the installed fiber and this feature decreased the measurement time to the orders of 10 micro seconds. Therefore, instead of instead of utilizing the sweeping frequency, this method uses pump pulse and probe wave at a fixed optical frequency individually. This method is based on two main assumptions, first, the shape of BGS spectrum does not considerably change while the strains is applied. Secondly, the measurements need to hold the BGS level. The first assumption limits the strain changes to smaller values corresponding to a 6 dB value of BGS, however the second assumption is used for calculation of central frequency (Li et al. 2010).

Measurements of strains over 100 m distances in AT-BOTDA mode were conducted with improved spatial resolutions of less than 20 cm in dynamic mode. These measurements were achieved over 1 KHz rate of acquisition frequency. Figure 1.4 shows the commercial Neubrescope 6055 device which is developed by Neubrex Company for dynamic BOTDA measurements.

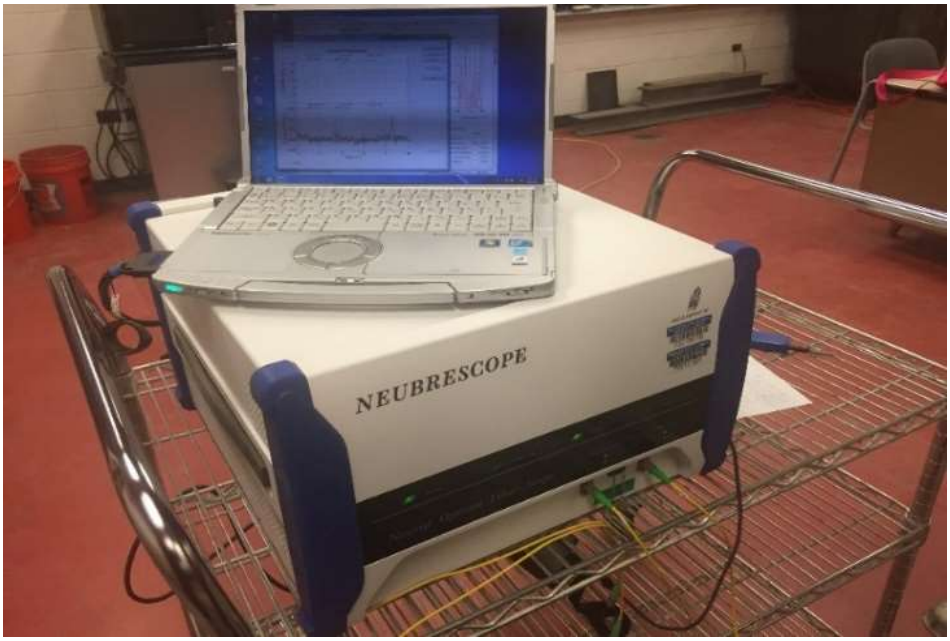

Figure 1.4 Neubrescope 6055 device

1.4. Application of fiber optic sensors

The technologies used in the structural health monitoring are is discussed in the previous sections. Various sensor types and their advantages and disadvantages are also been investigated thoroughly. In the next section application of fiber optic sensors in the assessment of infrastructures are discussed. This discussion is divided into two main categories. First one relates to measurements of applied loads to the bridges using point fiber optic sensors and bridge weigh in motion system and the second category is the investigation in the application of distributed fiber optic sensors on strain measurement of structures.

1.4.1 Bridge weigh in motion system

Accurate determination of moving loads on bridges provides for proper assessment of structural integrity, estimation of remaining life, improvements in future designs, enforcement of weight limits and planning for cost effective maintenance activities. Important information from typical weigh-in-motion (WIM) systems comprise of gross vehicle weights (GVWs), individual axle weights and vehicle speeds. It is also possible to classify the types of trucks crossing over the bridges from the axle spacing data. In general, roadside weigh stations are able to provide the weight and truck classification information accurately.

Weigh stations require additional infrastructure on the roadway sides, and not readily available near many bridges, and therefore, weighing of trucks are randomly implemented. To overcome this problem, pavement weigh in motion systems (WIM) and bridge weigh in motion (BWIM) systems have been introduced. Measurement of vehicle axle weights by pavement WIM are conducted by installing bending caps and piezoelectric strip sensors embedded in pavements (Yu et al. 2016).

In pavement WIM systems provide the required data, however, WIM systems need to be frequently calibrated. Their performance is affected by the condition and degradation of the pavement, thermal fluctuations and interaction of the pavement with the sensor system. Installation and maintenance of WIM systems require frequent destruction and re-construction of pavement segments, and lane closures (He et al, 2017; Chatterjee et al, 2006; Zhao et al, 2014).

BWIM systems are installed under the bridge and measure the gross and individual axle weights of the passing vehicles. Safer implementation and in many instances installations without lane closures are amongst the main advantages of bridge weigh in motion systems over pavement WIM systems. BWIM systems can be installed on bridges (Žnidarič et al, 2015) and unlike the pavement WIM systems, repeated axle loads due to passage of trucks do not wear down the sensors.

Moses (1979) proposed the initial idea of BWIM system for estimation of truck weights and speeds. Tape switches were employed in pavements for vehicle axle spacing and speed measurements. Strain gauges were used at the lower flanges of the girders for monitoring the flexural strains due to the truck weights on the bridge span. By relating the measured flexural strains to the products of the axle loads and moment influence lines and solving the system of equations, GVW of the passing trucks were obtained. This method was extended further by Moses and Ghosn (1983) to separate the GVW of multiple trucks passing in different lanes. Calculation of the influence surface during the calibration process with the trucks of known GVWs was the key component of this method.

Eventually this method was commercially made available in Europe (Jacobs & Loo, 2002). Because the pavement tape switches degraded shortly after usage, a free-of-axle detector (FAD) system was proposed by Znidaric et al (2015). They installed separate groups of strain sensors on the bottom side of the bridge deck. The purpose of these sensors was to detect axles of the trucks in weigh in motion system.

Other BWIM systems have also been proposed and developed over the past few years. Culway system was one of the early BWIM technologies introduced by Peters (1986) which correlated the peak responses of a calibrated truck responses to known truck responses. To eliminate the dynamic effect of the trucks, this system was mostly installed on the short span culverts to take advantage of the damping properties of the soil between the structure and the pavement. Algohi, et al. (2018) developed a new method to detect axle configuration of moving vehicles using acoustic emissions generated from expansion joints. O'Brian, et al. (2006) proposed a method to improve the BWIM system by calculating the influence line from direct strain measurements. Reaction force method (Ojio and Yamada, 2002), the moving-force identification (MFI) method, and their variations were also amongst some of the successful implementation of the flexure based BWIM techniques (Yu and Chan, 2007; Law, et al, 1997; Pinkaew, 2006; Rowley, et al, 2008; Deesomsuk and Pinkaew, 2010; Zhu and Law, 2006).

Review of recent literature indicates development of BWIM systems based on methods other than flexural response of Bridges. Helmi, et al (2015) developed a method based on measurement of shear strains by way of optical fiber strain rosettes at the Bridge abutments. O'Brien et al, (2012) used the shear strains for detection of truck axles. Bao, et al (2016) used shear rosette sensors and developed a shear influence line based approach for detection of axle weights, spacings and speeds as well as the GVW of the trucks. Bao, et.al's approach was automated and employed in a number of Bridges in USA. D. Feng and Feng (2015) introduced a method for the computation of vehicle speeds by minimizing the error between the measured and theoretically calculated displacement time histories of the bridge due to moving vehicles. A number of other

approaches have been recently developed, including the Virtual simply supported beam (VSSB) by He et al, (2017), simplified portable bridge weigh-in-motion (spBWIM) system by Sekiya et al, (2018) by using accelerometers instead of strain gauges; and nonconstant vehicle speed measurement in BWIM systems (Lansdell et al, 2017). An overview on the recent development in BWIM technology is also provided by Lydon, et al, (2016).

1.4.2 Application of distributed sensing using FOS

One of the most common application of distributed optical fiber sensors are in the health monitoring of bridges. Some of the investigations in this field are provided here. Glisic and Inaudi (2003) instrumented the Gotaalv bridge in Sweden which is a 1000 m long concrete slab bridge constructed on steel girders. This bridge has more than 50 piers. The continuous monitoring of this structure was required after the transportation authorities detected multiple crack along the bridge. The importance of distributed health monitoring was enhanced here since the bridge was required to be monitored in every single location due to the possibility of crack occurrence at any points. Therefore, a distributed optical fiber sensor system based on the Brillouin scattering technology was installed and experimented on the bridge in and monitored successfully. The system is measuring various parameters of the structure continuously from 2007 and is still in place.

Matta et al (2008) monitored a composite steel girder bridge with a Brillouin based distributed optical fiber sensor. Total length of optical fiber used in the monitoring system was about 1.15 km and it was used to measure strains and temperature throughout the

bridge in addition to loose fibers for temperature compensation. The results of the BOTDR was verified by a high accuracy total station system.

Glisic et al (2011) conducted another interesting monitoring experiment application. This time the distributed optical fiber sensors were built into the bridge during its construction stage. The Streicker bridge which is located in the campus of the Princton university was instrumented for this project. The monitoring of this structure provided valuable information regarding the global health of the bridge such as early behavior of the concrete for detection of damage which was unique. Validation of the results were achieved by comparing the results of the distributed strains with the outputs of the FBGs installed on multiple points of the bridge.

Comparison of two different installation types of the Brillouin based sensors including smart FRP bonding and near to surface fiber (NSF) were achieved by an experiment by Bastianini et al (2005). These two systems were installed on a reinforced concrete bridge which were going under diagnostic dynamic tests. It was depicted that the smart FRP bonding technique was more efficient and accurate compared to the other method. The cost of installation, reduction of experiment time and increase in performance was associated with this technique. This system was also installed for monitoring of a historical building by the same authors and the effectiveness of the method was prove there too.

Villalba et al (2010) used the distributed sensing technology with millimetric spatial resolution to monitor a reinforced concrete bridge in Barcelona. They installed the

distributed sensing system under the slab of the concrete deck and used the real dynamic loading to measure the data.

Zhao et al (2012) installed a multiscale fiber optic sensing mesh with a combination of FBG and BOTDA based distributed sensors to take advantage of developed global sensing method to achieve a high resolution in measurements. The stresses generated throughout the structure were measured with the distributed optical fiber sensors and the comprehensive data about the bridge were reported.

A reinforced concrete bridge over the black river in Canada were monitored by Regier and Hoult (2014) using distributed optical sensing technology. The results showed reliable information by being validated with other instrumentations such as strain gauges. Moreover, displacements of the bridge were also calculated using the distributed strains over the entire length of the bridge and the results depicted close relationship with the measurements with displacement sensors. This was used to prove that it is possible to calculate the deflection of the structure based on the measured strains with the distributed optical sensors. The method was successful in detection cracks location and their corresponding strains due to the loading, however, strain measurements in the area close to the cracks were reported to be challenging because of optical fiber's robustness feature. In addition, temperature compensation were achieved through measurement of strains and temperatures in a short period of time, however further investigation were suggested for long term monitoring and temperature effects. It was also advised to conduct more detailed experiments on the relationship between the measurements and cracks width.

1.5. Research outline

There are two main categories that can be investigated on infrastructures such as bridges. The first category pertains to investigation of response of the bridge to the applied loads. Deflection, reactions, internal forces and stresses falls into this category. Observing the behavior of the structure is conducted mainly by measuring the distributed strains. The second category corresponds to the applied loads affecting the structure. In other words, it is essential to have an exact evaluation of the external loads affecting the structural components. These external loads can be traffic loads such as vehicle axle loads and thermal cycles. Detailed information such as frequency and magnitude of live loads over the bridge is essential for proper evaluation of bridge under oversized loads. The following thesis investigates these two categories and their effects on the bridges.

In chapter 2, detection of micro cracks through using the distributed optical fiber sensing technology is introduced. A theoretical model is proposed to identify surface micro cracks through the entire length of the bridge without reference measurements. This technique is achieved by applying multiple static loads on the bridge spans using calibrated trucks. Calculating differential distributed strain in theory and comparing it with the measured distributed strains by defining a damage index ratio provides the probability of micro-crack detection in the superstructure. Development of the proposed method into the dynamic applications are discussed in Chapter 3. The development includes utilizing moving trucks as applied loads and localizing micro cracks based on the defined crack index. The proposed method in this chapter aims to eliminate the traffic closure for crack detection purposes and use the regular traffic as the live load for monitoring intentions. Experimental programs are defined and conducted on two multi-span bridges. The

detailed description of the superstructures and experimental tests are provided in Chapter 2 and 3. The thesis follows with Chapter 4 which pertains to the development of a new Bridge Weigh-in-Motion system based on monitoring the rotations at the bridge abutments. The measured end rotations are directly related to the axle loads by means of influence lines. The changes in girder rotations at the abutments are measured by a fiber optic rotation sensor, specifically designed for the proposed BWIM system. The theoretical models relating the rotation of the abutment to the changes of strains in the middle section of the sensors is also provided in this chapter. The rotation sensors are then incorporated into the BWIM system for correlation of the axle weights to the end span rotations. Applicability and accuracy of the proposed system was examined by tests on a four-span steel girder bridge. The field implementation included calibration and validation of the system with trucks pre-weighed at a nearby weigh station.

The materials of current chapter are partially published with the following citations:
Abdoli Oskoui, E., Taylor, T., & Ansari, F. (2019). Method and monitoring approach for distributed detection of damage in multi-span continuous bridges. Engineering Structures, 189, 385-395. doi:10.1016/j.engstruct.2019.02.037
Please refer to the authors' contributions in page iv in the beginning of this document for details of contributions.

Chapter 2 . METHOD AND MONITORING APPROACH FOR DISTRIBUTED DETECTION OF DAMAGE IN MULTI-SPAN CONTINUOUS BRIDGES

2.1. Introduction

Structural monitoring with a typical Brillouin scattering system, i.e. PPP-BOTDA, involves two measurements: (1) reference measurement prior to the change or application of loads; (2) measurement following a change in state or change in load. Difference between the two distributed strain measurements pertains to change in state of the structure. The practical applicability of this method in static mode may be limited to its use in load testing of bridges.

To effectively detect damage, this approach would require reference measurements of the structure at pristine stage. This renders the method impractical for high resolution detection of damage. In addition, the signal-to-noise ratio for Brillouin systems is low, complicating processing of data at static as well as in dynamic modes of operations. The objective for the work described in this chapter was to develop an analytical approach for detection and quantification of damage during load tests. The proposed approach does not require measurements at the original pristine state of the

bridge for the detection of defects. Instead it uses multiple positions of the load for construction of the influence line and comparison with the theoretical strains.

Verification of the method was accomplished, by use of the proposed method in testing of a 332-meter, 5-span precast, post tensioned segmental concrete box girder bridge. It was possible to detect the locations of the cracks in using this approach. Formulation of the analytical approach is described next, followed by the instrumentation and testing of the bridge.

2.2. Analytical Approach

Measured distributed strain along the span of a bridge contains influence from a number of perturbations in addition to the flexural response as a result of live loads. System noise, thermal effects, and defect induced singularities, and pre-tensioning effects during installation of the optical fiber contribute to the measured distributed strain. The distributed strain response of the bridge with defects is generally described by the following relationship (Bao et al 1993):

$$\varepsilon_P = \varepsilon_T + \varepsilon_L + \varepsilon_i + \varepsilon_C \quad (2.1)$$

Where, ε_P, is the measured strain at a sampling point along the length of the optical fiber, ε_T, is the strain due to variation in temperature, ε_L, is the strain due to the live load, ε_i is the strain induced in the fiber during the installations and ε_C is the crack induced strain peak due to pre-existing damage in the bridge.

Generally, a loose fiber is utilized to compensate the effect of temperature induced strains, ε_T, in distributed fiber optic sensing. Similar method is used in the present

research. However, Strains generated by dynamic loads under normal ambient conditions are not effected by temperature strains since the measurement durations are minimal. The effects of optical fiber installations are manifested as residual strains. They are automatically removed by the formulations proposed herein. PPP-BOTDA technology includes the system noise which has a higher level in smaller spatial resolution measurements.

BOTDA measures the distributed strains at pre-defined sampling points and spatial resolutions along the fiber length. The measured strain at each sampling point is computed based on the weighted average of neighboring points defined by the spatial resolution by Kishida and Nishiguchi (2005):

$$\varepsilon_{P_i}^{M} = \frac{1}{d}\sum_{s=-d/2}^{d/2} \varepsilon_i(s).\Delta_s \qquad (2.2)$$

Where, $\varepsilon_{P_i}^{M}$ is the measured strain at sampling point P_i, d is the spatial resolution defined earlier, s, is the spatial distance along the fiber and $\varepsilon_i(s)$ is the actual strain at distance s from the sampling point. Accordingly, the BOTDA measured strain at a sampling point along the length of the fiber is the weighted average strain represented by equation (2.2).

Identification of damage beyond the signal to noise limits of the instrument is achieved by normalization of the measured distributed strains during multiple positions of a truck with respect to the theoretical influence line of the bridge. Figure 2.1 illustrates the moment influence line for an arbitrary point, P_i , along the length of a 5-span bridge. Per definition, the function representing the influence line is generated by moving a unit load

along the bridge and calculating the moment at point P_i for the unit load. Moment due to multiple point loads (representing truck axles) at point P_i is computed by the product of each axle load and the ordinates of the influence line at the locations of the truck axles. A truck with three axles at five different loading positions is shown in figure 2.1. Considering the relationship between the flexural strain and moment as shown below:

$$\varepsilon = My/EI \tag{2.3}$$

For an arbitrary point P_i, flexural strain due to the truck load, $\varepsilon_{P_i}^T$, is computed as:

$$\varepsilon_{P_i}^T = \frac{\sum_1^m A_m IL_{P_i}(x_m)\, y}{EI} = \frac{\left(A_1 IL_{P_i}(x_1) + A_2 IL_{P_i}(x_2) + \ldots + A_m IL_{P_i}(x_m)\right) y}{EI} \tag{2.4}$$

Where, superscript T is employed in order to indicate computed or theoretical strain, m, is the number of truck axles, A_m is the truck axle load, x_m is the distance from the location of the mth axle with respect to the bridge end/abutment, $IL_{P_i}(x_m)$ is the ordinate of the moment influence line at x_m, E is the modulus of elasticity, I is the moment of inertia of the section and y is the distance between the location of the fiber on the section and its neutral axis.

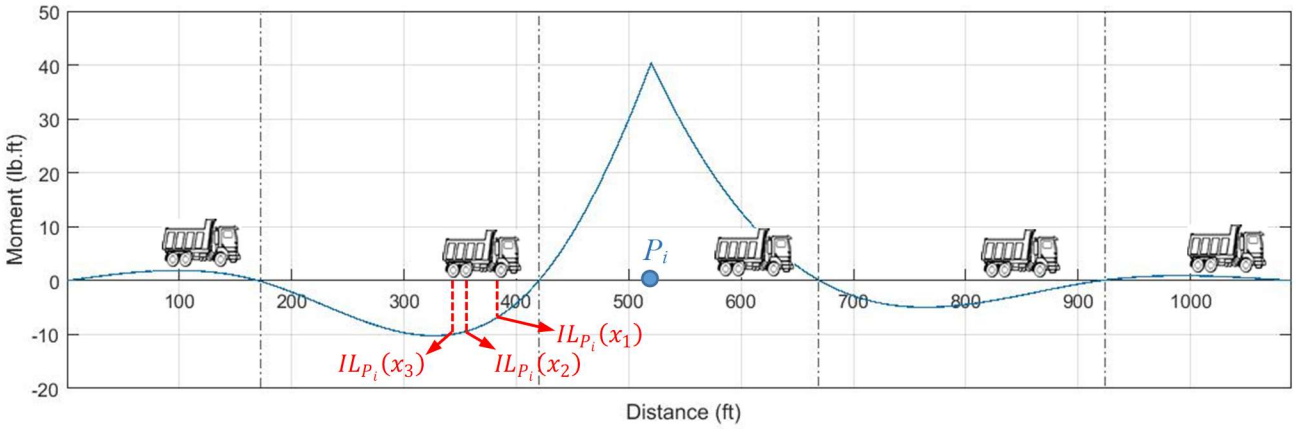

Figure 2.1 Moment influence line of point P_i

The theoretical strains for all the sampling points along the length of the optical fiber can be represented in vectoral form shown below:

$$[\varepsilon^T]_n = \begin{bmatrix} \varepsilon_{P_1}^T \\ \varepsilon_{P_2}^T \\ \vdots \\ \varepsilon_{P_i}^T \end{bmatrix}_n \quad (n = 1,2,\dots,k) \tag{2.5}$$

Where, k is the total number of loading positions and $[\varepsilon^T]_n$ is the vector including theoretical strains along the entire length of the bridge resulting from truck loads in load positions, n. By moving a truck with known axle weights and axle spacings over the bridge, a continuous strain profile for the sampling point P_i can be computed as shown in figure 2.2.

The difference between the theoretical strains due to two adjacent load positions for all sampling points, $[\Delta\varepsilon^T]_{n+1,n}$ is defined as:

$$[\Delta\varepsilon^T]_{n+1,n} = [\varepsilon^T]_{n+1} - [\varepsilon^T]_n = \begin{bmatrix} \left(\Delta\varepsilon^T_{P_1}\right)_{n+1,n} \\ \left(\Delta\varepsilon^T_{P_2}\right)_{n+1,n} \\ \vdots \\ \left(\Delta\varepsilon^T_{P_i}\right)_{n+1,n} \end{bmatrix} = \begin{bmatrix} \left(\varepsilon^T_{P_1}\right)_{n+1} - \left(\varepsilon^T_{P_1}\right)_n \\ \left(\varepsilon^T_{P_2}\right)_{n+1} - \left(\varepsilon^T_{P_2}\right)_n \\ \vdots \\ \left(\varepsilon^T_{P_i}\right)_{n+1} - \left(\varepsilon^T_{P_i}\right)_n \end{bmatrix}$$

$$= \frac{y}{EI} \begin{bmatrix} \sum_1^m \left[\left(A_m IL_{P_1}(x_m)\right)_{n+1} - \left(A_m IL_{P_1}(x_m)\right)_n\right] \\ \sum_1^m \left[\left(A_m IL_{P_2}(x_m)\right)_{n+1} - \left(A_m IL_{P_2}(x_m)\right)_n\right] \\ \vdots \\ \sum_1^m \left[\left(A_m IL_{P_i}(x_m)\right)_{n+1} - \left(A_m IL_{P_i}(x_m)\right)_n\right] \end{bmatrix} \tag{2.6}$$

Where, $\left(\varepsilon^T_{P_i}\right)_n$ is the theoretical strain at point P_i due to load position at n, $[\varepsilon^T]_{n+1}$, is the theoretical strain at position, $n+1$, and $\left(\Delta\varepsilon^T_{P_i}\right)_{n+1,n}$ is the theoretical strain differences at P_i for the two load positions, n, and $n+1$.

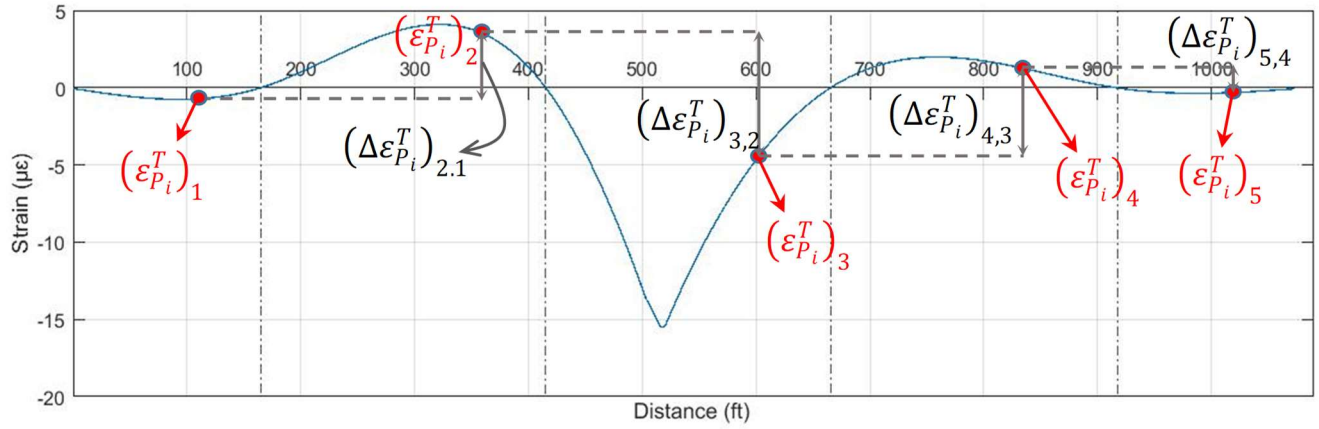

Figure 2.2 Theoretical strain profile for point P_i due to a specific truck load

Conversely, the strain profile at P_i can be established from the measured distributed strain during the load tests of the bridge. An example of this plot for a five span bridge is shown in figure 2.3. The theoretical strain profile at P_i is curvilinear since it represents the strain history of a specific point under a continuous moving load. The strain profile shown in figure 2.3 is linear since it was constructed by measurement of strain at P_i for five distinct truck positions.

The difference between the BOTDA measured strains from two adjacent truck positions during the load tests, $[\Delta\varepsilon^M]_{n+1,n}$, is defined as:

$$[\Delta\varepsilon^M]_{n+1,n} = [\varepsilon^M]_{n+1} - [\varepsilon^M]_n = \begin{bmatrix} \left(\Delta\varepsilon^M_{P_1}\right)_{n+1,n} \\ \left(\Delta\varepsilon^M_{P_2}\right)_{n+1,n} \\ \vdots \\ \left(\Delta\varepsilon^M_{P_i}\right)_{n+1,n} \end{bmatrix} = \begin{bmatrix} \left(\varepsilon^M_{P_1}\right)_{n+1} - \left(\varepsilon^M_{P_1}\right)_n \\ \left(\varepsilon^M_{P_2}\right)_{n+1} - \left(\varepsilon^M_{P_2}\right)_n \\ \vdots \\ \left(\varepsilon^M_{P_i}\right)_{n+1} - \left(\varepsilon^M_{P_i}\right)_n \end{bmatrix} \tag{2.7}$$

Where, $[\varepsilon^M]_n$ and $[\varepsilon^M]_{n+1}$ are the measured strains at P_i for load positions n and $n+1$, respectively. It should be noted that these strains are a combination of live loads and contributions of other perturbations introduced in equation 2.1. $\left(\Delta\varepsilon^M_{P_i}\right)_{n+1,n}$ is the measured strain difference, or strain differential, at P_i for load positions n and $n+1$. The effects of all the other perturbations were removed from the measured strain differentials through the differential process.

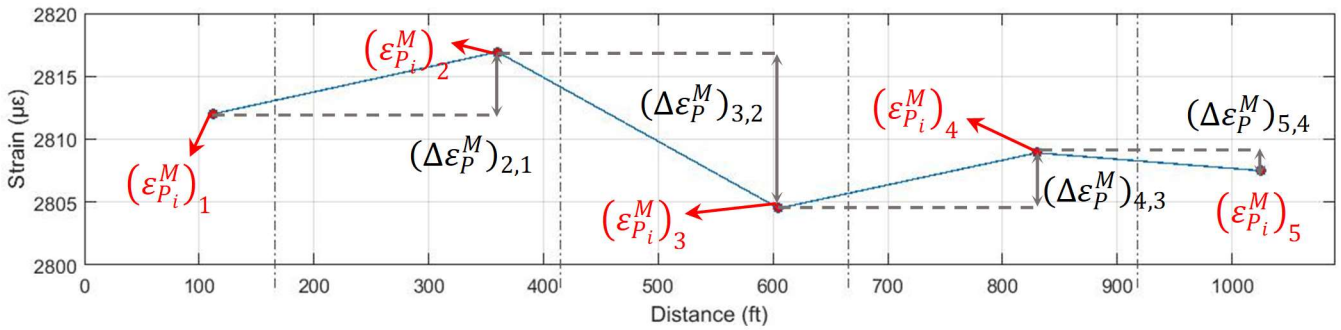

Figure 2.3 Measured strain profile for point P_i due to truck load

Comparison of the measured and theoretical strain differentials is achieved by computing the ratio between the two. This is accomplished by dividing equation (2.7) by equation (2.6):

$$\alpha_{P_i}^n = \frac{\left(\Delta\varepsilon_{P_i}^M\right)_{n+1,n}}{\left(\Delta\varepsilon_{P_i}^T\right)_{n+1,n}} \qquad (n = 1,2,\dots,k-1) \tag{2.8}$$

Where, $\alpha_{P_i}^n$ is the differential strain ratio. For a crack-free bridge, the measured and theoretical differential strain distributions are equal, i.e. $\left(\Delta\varepsilon_{P_i}^M\right)_{n+1,n} = \left(\Delta\varepsilon_{P_i}^T\right)_{n+1,n}$, and therefore, the differential strain ratio, $\alpha_{P_i}^n = 1$. For bridges with Cracks and defects, the strain peaks at the crack locations increase the strains measured by the optical fiber, whereas, the theoretical strain remains the same. Therefore, $\left(\Delta\varepsilon_{P_i}^M\right)_{n+1,n} > \left(\Delta\varepsilon_{P_i}^T\right)_{n+1,n}$, and the differential strain ratio becomes larger than, i.e. $\alpha_{P_i}^n > 1$. The larger the differential strain ratio, the more likelihood for presence and severity of damage. The

number of differential strain ratios, $\alpha_{P_i}^n$ at each sampling point is dependent on the number of loads tests (i.e. load positions at one or more spans).

Since the differential strains are computed by subtracting the strain at a sampling point for two different load positions, the number of $\alpha_{P_i}^n$ is equal to the number of load positions during the load tests minus 1, i.e. $n = k - 1$. Where, *n* is the number of differential strain ratios computed at each sampling point, and *k* is the number of load positions during load tests. Then the effects of all the differential strain ratios at each sampling point can be combined into a single value as the damage index at that point. The damage index, $\hat{\beta}_{P_i}$, at each sampling point is defined by the product of all the differential strain ratios, and then normalizing the computed vector as follows:

$$\beta_{P_i} = \prod_{n=1}^{k-1} \alpha_{P_i}^n = \alpha_{P_i}^1 \times \alpha_{P_i}^2 \times \ldots \times \alpha_{P_i}^n \tag{2.9}$$

$$[\hat{\beta}_p] = \frac{1}{(\beta_{P_i})_{max}} \begin{bmatrix} \beta_{P_1} \\ \beta_{P_2} \\ \vdots \\ \beta_{P_i} \end{bmatrix} = \begin{bmatrix} \hat{\beta}_{P_1} \\ \hat{\beta}_{P_2} \\ \vdots \\ \hat{\beta}_{P_i} \end{bmatrix} \tag{2.10}$$

Damage index vector $[\hat{\beta}_p]$, comprises of individual point damage indices, $\hat{\beta}_{P_i}$, that varies between zero and one with higher values indicative of higher likelihood of damage at the sampling point. By acquiring the distributed strain data following the load tests of a bridge and computing the damage index for all the sampling points, it will be possible to pinpoint the location of damage along the length of the bridge. The capability of the proposed approach for detection and identification of damage were evaluated during the

load tests of a 5-span concrete box girder bridge. Description of the load tests and measurement technique are described next.

2.3. Evaluation of the Method

Evaluation of the proposed approach was accomplished by monitoring the distributed strains during the load tests of the Kishwaukee river bridge, a 5-span continuous box girder bridge in Northern Illinois. Kishwaukee bridge consists of two structures carrying the North and Southbound traffic directions of interstate highway 39 (I-39) over the Kishwaukee river near Rockford, Illinois. The bridge under consideration is the structure carrying the Southbound traffic of I-39 (Figure 2.4).

The elevation and plan views of the bridge are shown in figure 2.5. The superstructure is a continuous five span precast post-tensioned concrete box girder with a total length of 332.2 m (1090 ft). The two end spans are each 51.8 m (170 ft) long, and the three middle spans are each 76.2 m (250 ft) long. The superstructure consists of segmental precast members with a cast in place segment in the middle of each span. The bearings at the first and fourth piers are fixed but the other two bearings in between along with the ones at the abutments are free to move in the longitudinal direction.

Figure 2.4 Kishwaukee River Bridge – Southbound

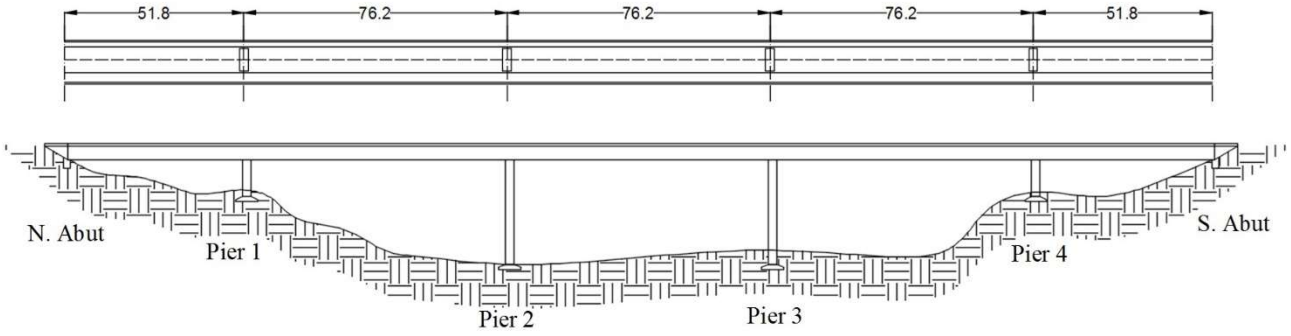

Figure 2.5 Plan and elevation views of the Kishwaukee bridge (units in meter)

The cross section of the bridge is shown in Figure. 2.6. The width of the cross section is 12.5 m (41 ft) which includes two 3.65 m (12 ft) lanes with a 3.04 m (10 ft) shoulder on the right and a 1.82 m (6 ft) shoulder on the left side of the traffic direction. The thickness of the slab varies from 22.9 cm (9 in) at the middle to 35.6 cm (14 in) at the

connection to the webs and 25.4 cm (10 in) at the hanging cantilever endings. The superstructure of the bridge was constructed with a concrete having a compressive strength of 37.9 MPa (5500 psi). Pre-stressed bars were used at the top and bottom flanges. The number of bars at the top flange varied from 100 at the piers to 2 at the middle section of spans. For the bottom flange, the numbers varied from 40 at the middle section of the spans to 2 at the piers location. The superstructure is located about 33.5 m (110 ft) above the Kishwaukee River. The concrete in the piers had a compressive strength of 24.1 MPa (3500 psi).

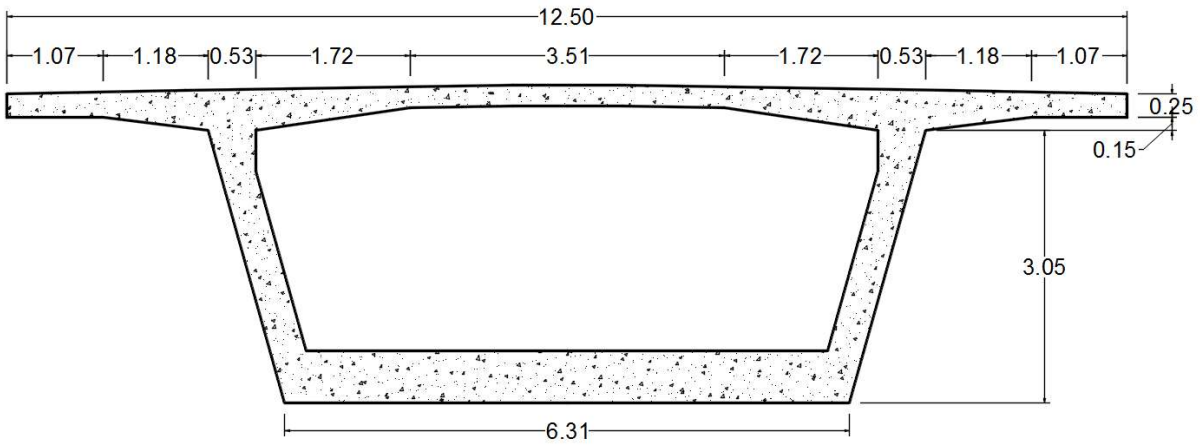

Figure 2.6 Sectional view of the Kishwaukee River bridge (units in meter)

2.3.1. Instrumentation

A single mode telecommunication grade optical fiber, Corning's SMF-28, was employed to serve as the distributed sensor. The core, cladding and coating diameters of

SMF-28 are 9, 125, and 250 μm, respectively. As shown in figure 2.7, the optical fiber was adhered to the inner side of the upper flange of the box girder. The distributed sensor covered all five spans of the bridge for a total length of 332.2 m (1090 ft).

A Silicon based adhesive was employed for adhering the optical fiber to the girder surface. The fiber was pretensioned over its entire length. A commercially available PPP-BOTDA was employed during the tests (Neubrescope NBX-6055). During the load tests, the lead line of the optical fiber distributed sensor was routed out of the box girder and connected to the BOTDA. It was more efficient to operate the BOTDA from outside of the box girder in order to coordinate the load test activities with the highway crew operating the trucks which were employed for load tests. Figure 2.8 pertains to the BOTDA device at the bridge site.

Figure 2.7 Location of the glued optical fiber on the section

Figure 2.8 PPP-BOTDA device at the Bridge site (Neubrescope NBX-6055)

2.3.2. Static Load Tests

Load tests were accomplished by using pre-weighed calibrated trucks. The axle configuration for a typical truck employed for the load tests is shown in figure 2.9. The first, second and third axles in each of the trucks, weighed 35.6 kN (8 kips), 88.9 kN (20 kips), and 80 kN (18 kips), respectively for a total gross vehicle weight of 204.6 kN (46 kips).

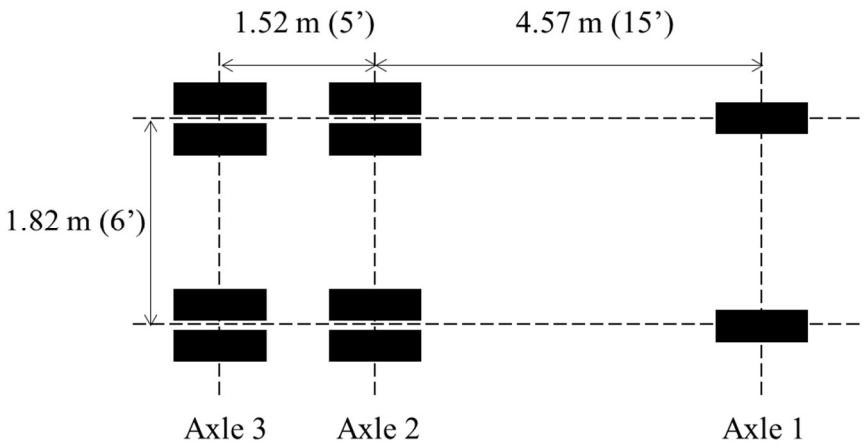

Figure 2.9 Axle configuration of the calibrated truck

As shown in Table 2.1, four different load cases were considered in the load tests. For load case 1, two trucks were used side by side in order to load each one of the five spans of the bridge in sequential manner. The same sequential loading of individual spans was repeated for load cases 2 and 3. For load case 2, three trucks were employed for loading of the individual spans, whereas, four trucks were employed for load case 3. For load cases 1 and 2, all the trucks were positioned side-by-side on each span. In load case 3, loading of spans was accomplished by placing the four trucks in two rows due to the bridge width limitation.

The effect of simultaneous loading of different spans was considered in load case 4. In each load position for load case 4, two spans were simultaneously loaded with two trucks on each with an empty span in between as shown in Table 2.1. Interstate 39 is a busy highway with heavy traffic, and therefore, the load tests were performed after the midnight, by closing the bridge to traffic in fifteen minute intervals for each of the load

cases. The PPP-BOTDA device was employed to acquire the distributed strain data at each individual load position. A spatial resolution of 20 cm, and sampling interval of 5 cm was employed for all the measurements. To clarify the truck alignment and positioning, a plan view from the second loading position of each loading case is illustrated in figure 2.10.

Table 2.1 DESIGNED LOAD CASES

		Applied load locations				
		span 1	span 2	span 3	span 4	span 5
Case 1	position 1	2 trucks				
	position 2		2 trucks			
	position 3			2 trucks		
	position 4				2 trucks	
	position 5					2 trucks
Case 2	position 1	3 trucks				
	position 2		3 trucks			
	position 3			3 trucks		
	position 4				3 trucks	
	position 5					3 trucks
Case 3	position 1	4 trucks				
	position 2		4 trucks			
	position 3			4 trucks		
	position 4				4 trucks	
	position 5					4 trucks
Case 4	position 1	2 trucks		2 trucks		
	position 2		2 trucks		2 trucks	
	position 3			2 trucks		2 trucks

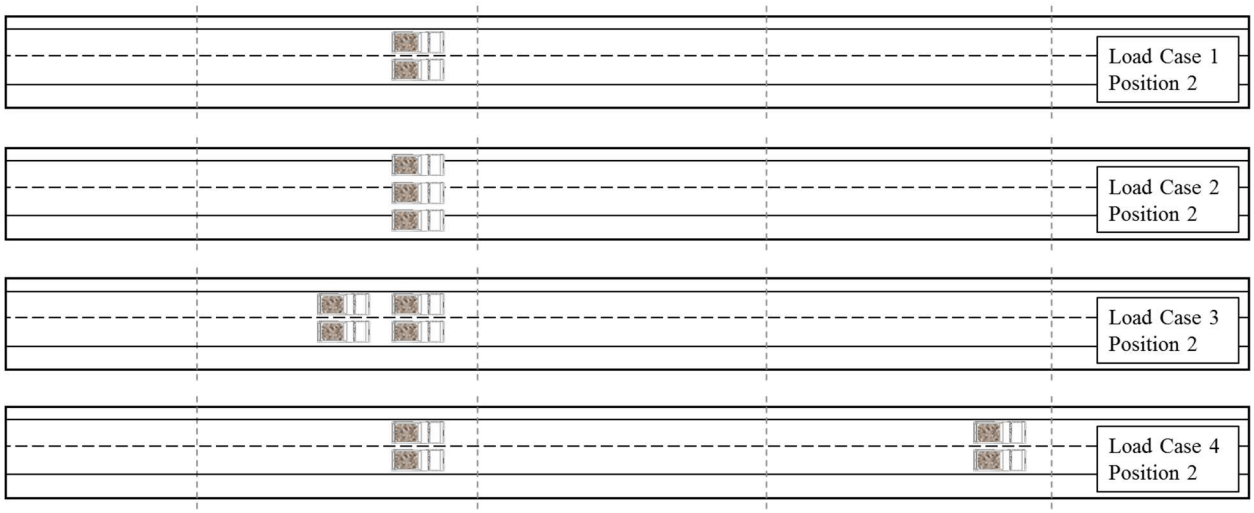

Figure 2.10 Typical loading locations of position 2 in all cases

2.3.3. Finite Element Model

Validating the measured strain was achieved by comparing the results with a finite element model created with the commercial software, CSI Bridge. Eight node solid elements were used for modeling the superstructure along with tendon elements for modeling pre-stressed and post tensioned tendons. Section dimensions and material properties for modeling were obtained from the original bridge construction documents and drawings. Figures 2.11 and 2.12 show the finite element model.

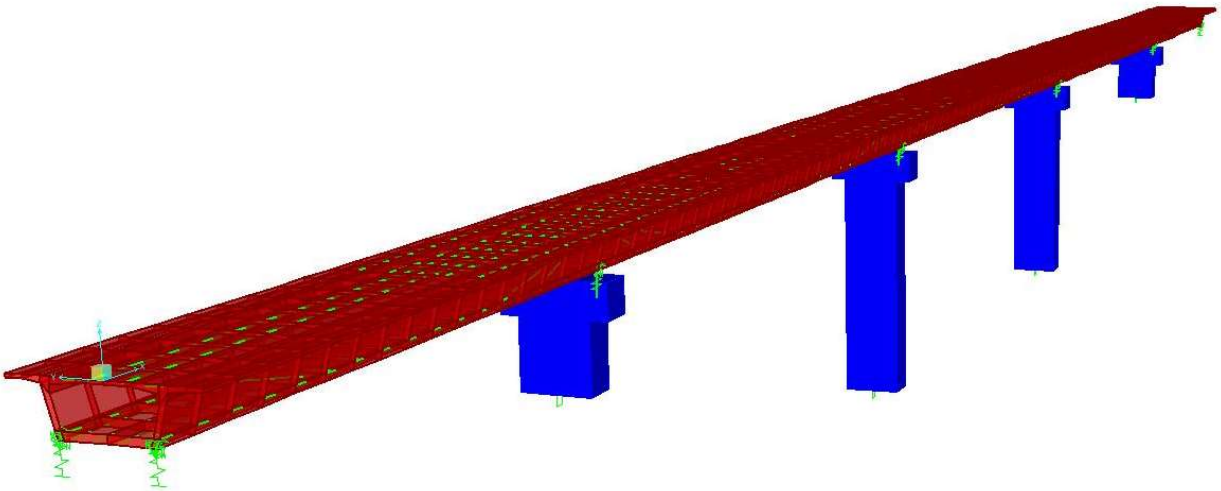

Figure 2.11 Three dimensional finite element view of the Kishwaukee River bridge

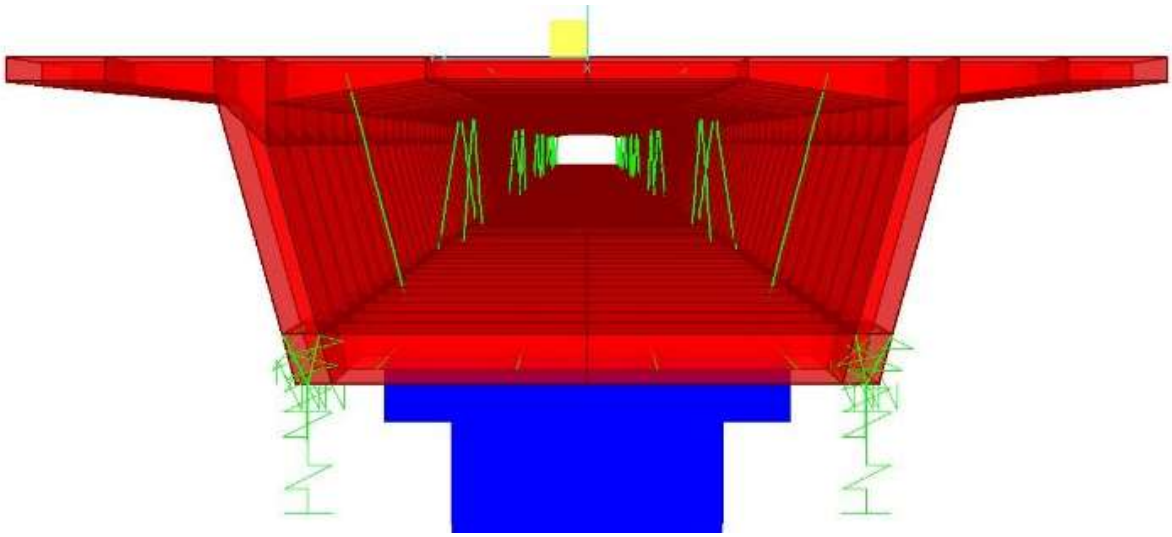

Figure 2.12 Sectional view of the finite element model of the Kishwaukee River bridge

2.4. Results

The BOTDA measured strains were filtered by using the moving averages in order to reduce the noise from the raw data. Figures. 2.13 through 2.30 pertain to typical data

for comparison of the measured and computed distributed strains. Both filtered and unfiltered strains are shown in these figures. They include data for the five loading positions of all load cases. Table 2.2 corresponds to the average errors or difference between the measured and computed strains in each of the load cases considered in this study.

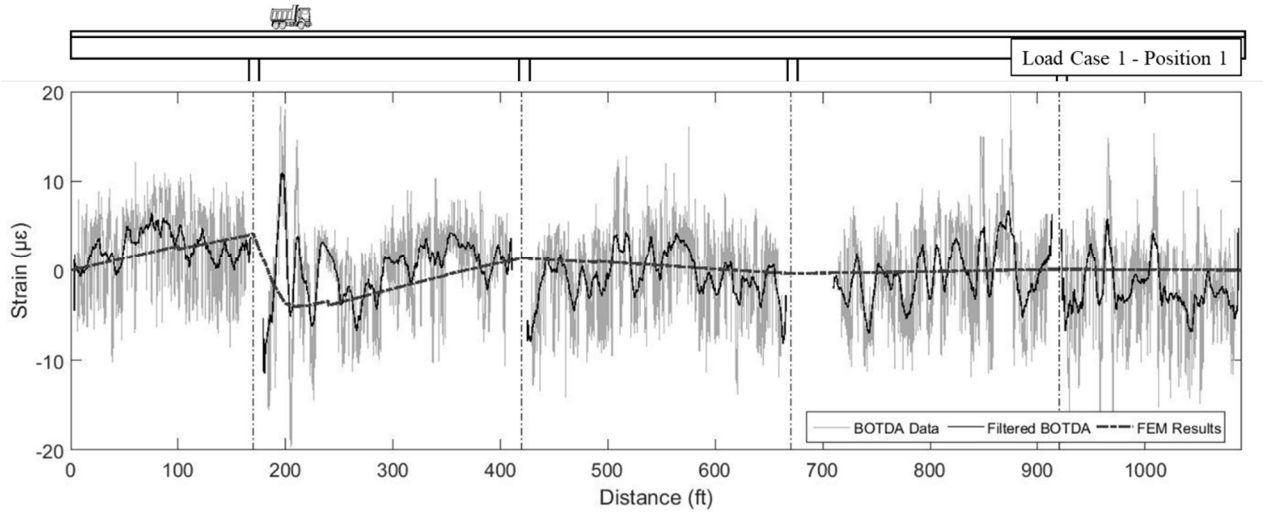

Figure 2.13 BOTDA strain measurement comparison with FEM for Case 1 – Position 1

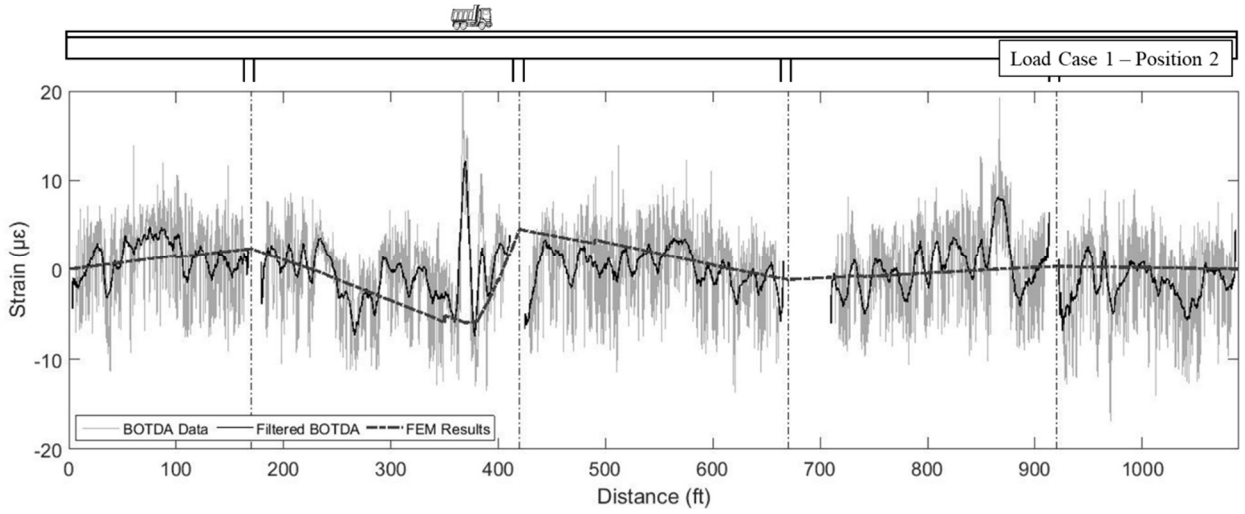

Figure 2.14 BOTDA strain measurement comparison with FEM for Case 1 – Position 2

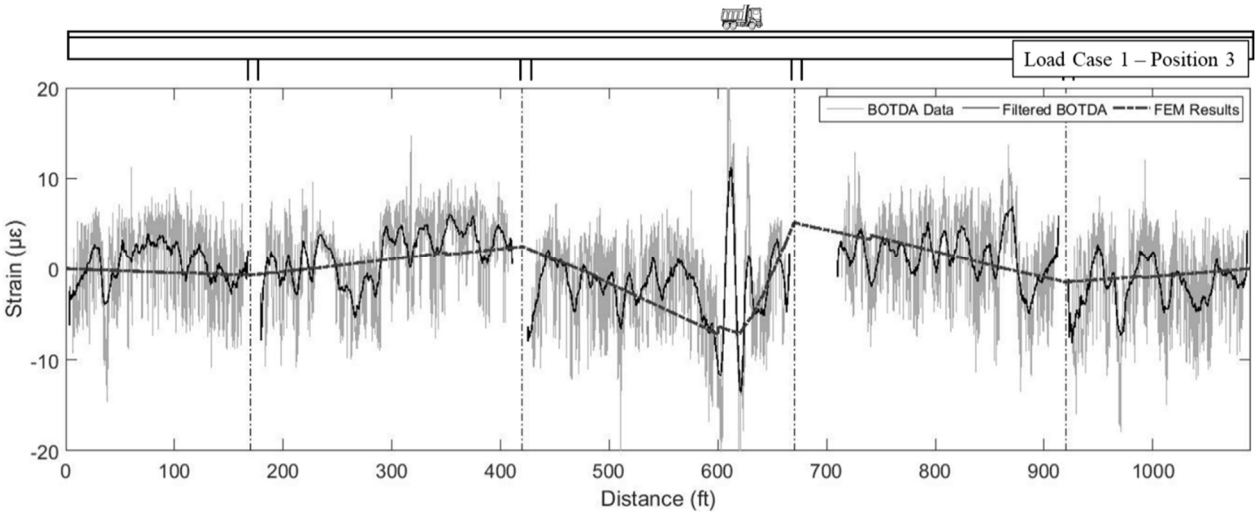

Figure 2.15 BOTDA strain measurement comparison with FEM for Case 1 – Position 3

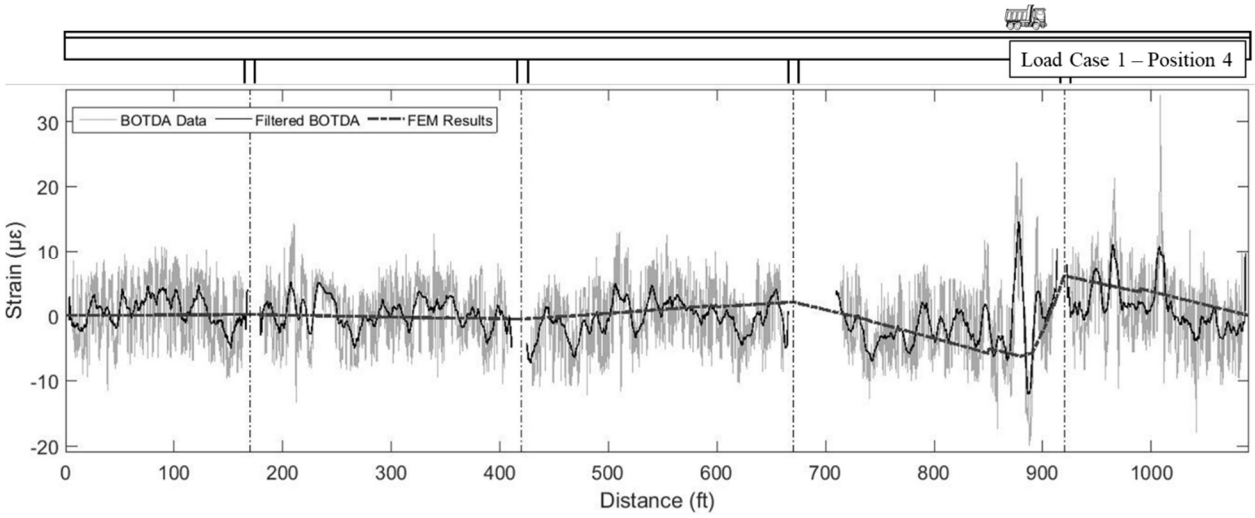

Figure 2.16 BOTDA strain measurement comparison with FEM for Case 1 – Position 4

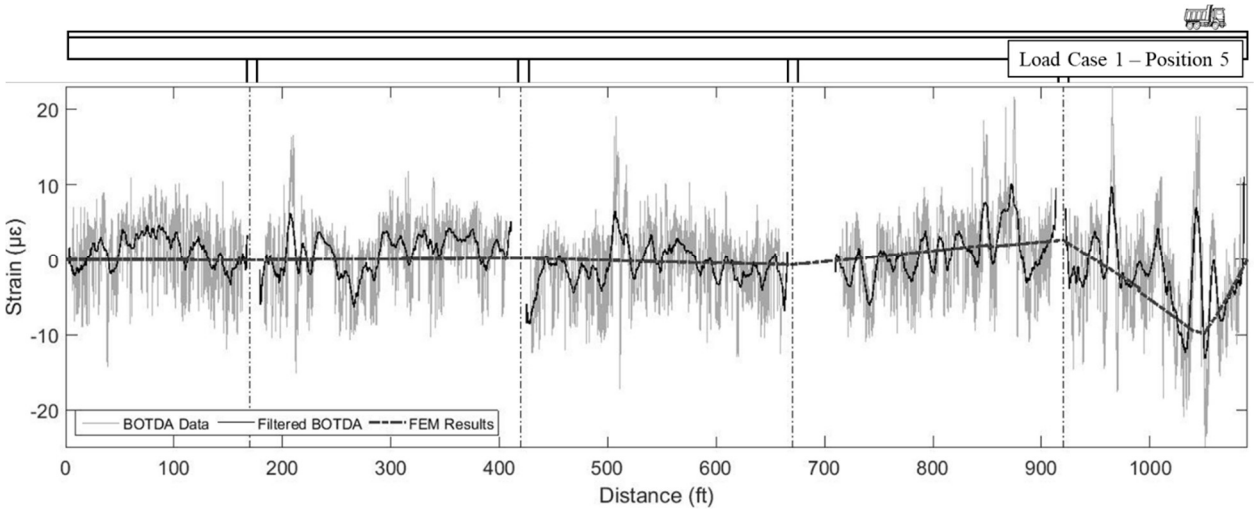

Figure 2.17 BOTDA strain measurement comparison with FEM for Case 1 – Position 5

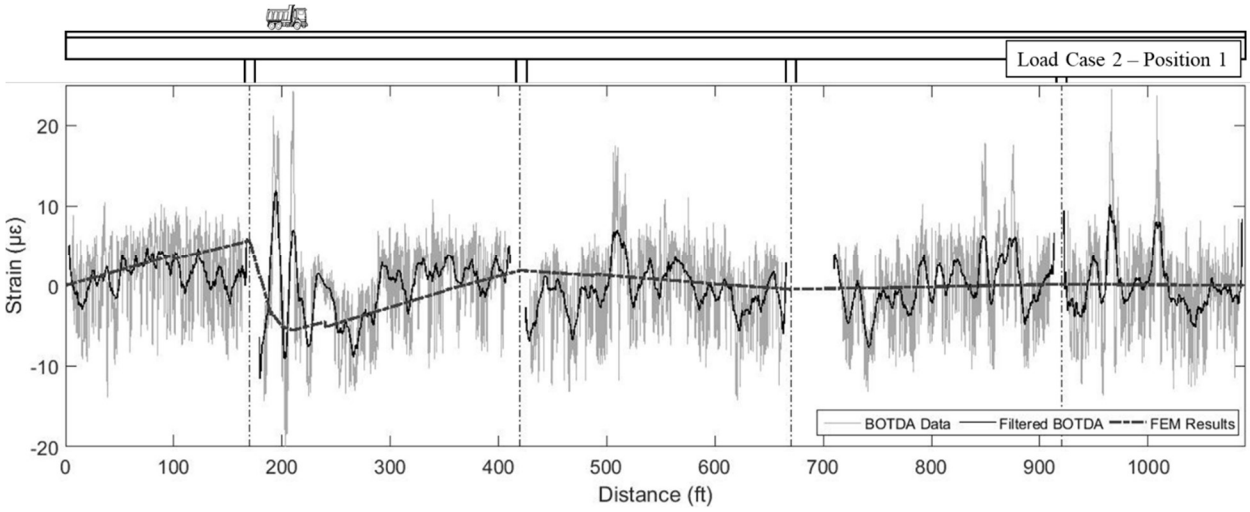

Figure 2.18 BOTDA strain measurement comparison with FEM for Case 2 – Position 1

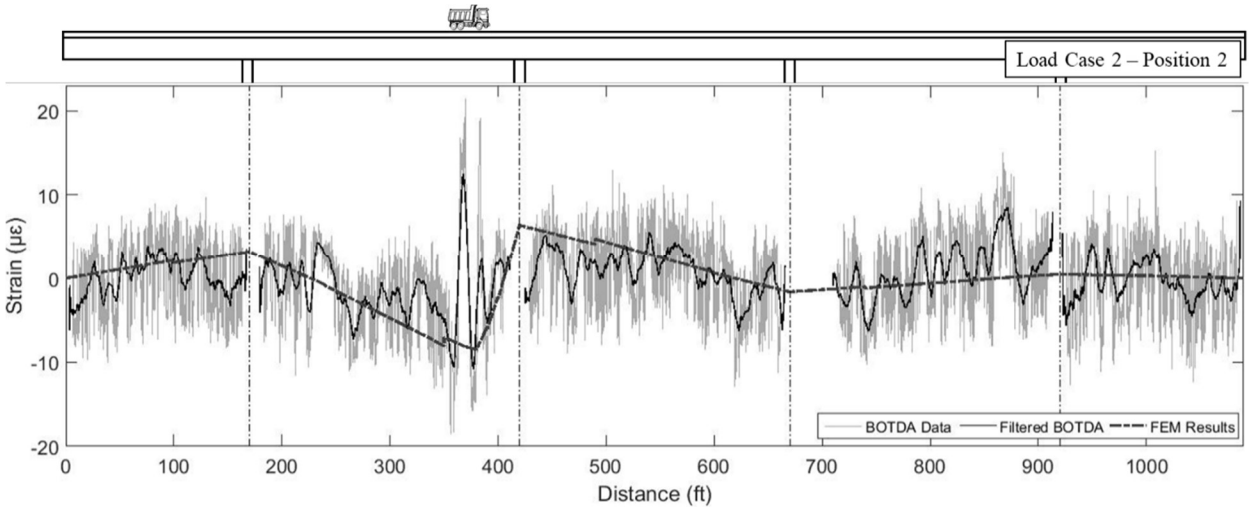

Figure 2.19 BOTDA strain measurement comparison with FEM for Case 2 – Position 2

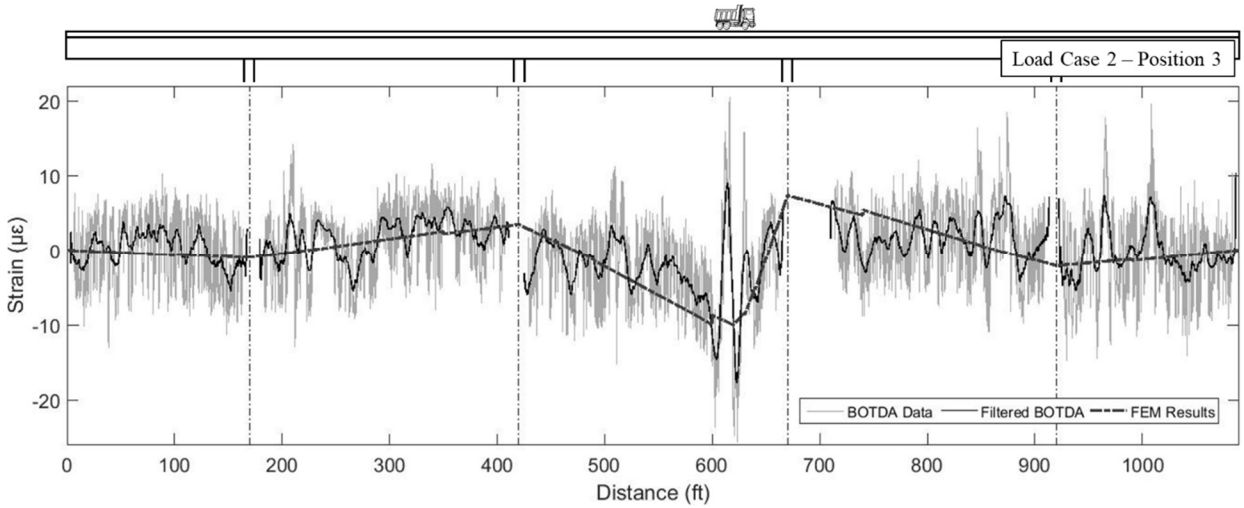

Figure 2.20 BOTDA strain measurement comparison with FEM for Case 2 – Position 3

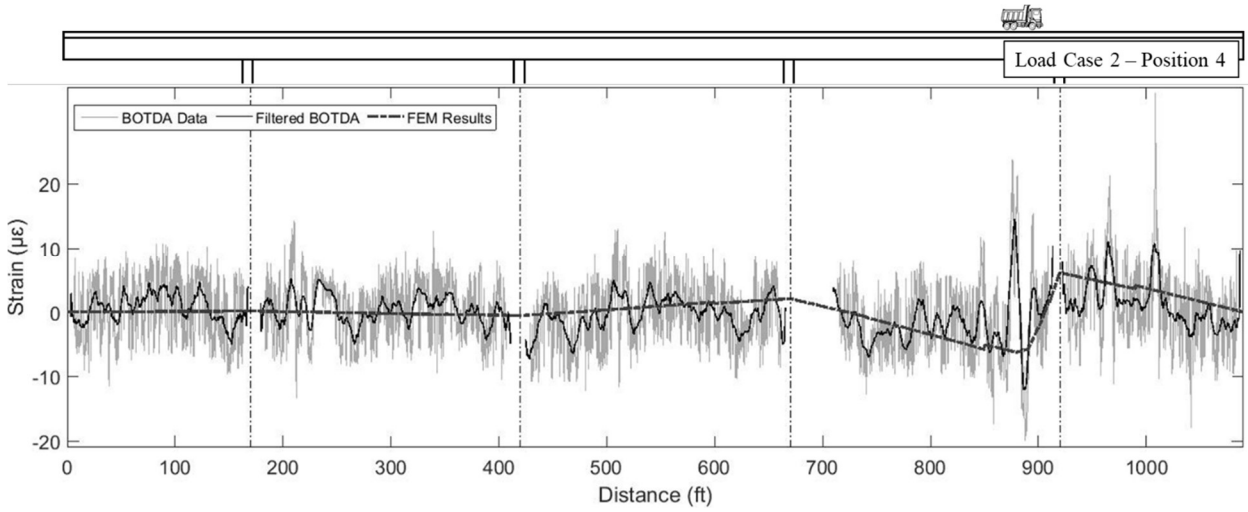

Figure 2.21 BOTDA strain measurement comparison with FEM for Case 2 – Position 4

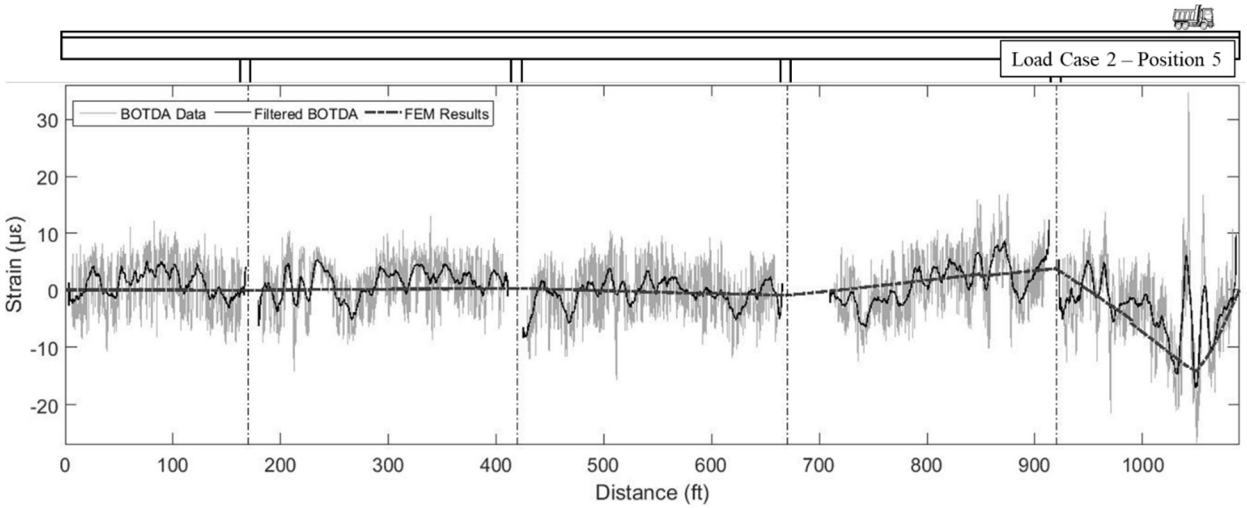

Figure 2.22 BOTDA strain measurement comparison with FEM for Case 2 – Position 5

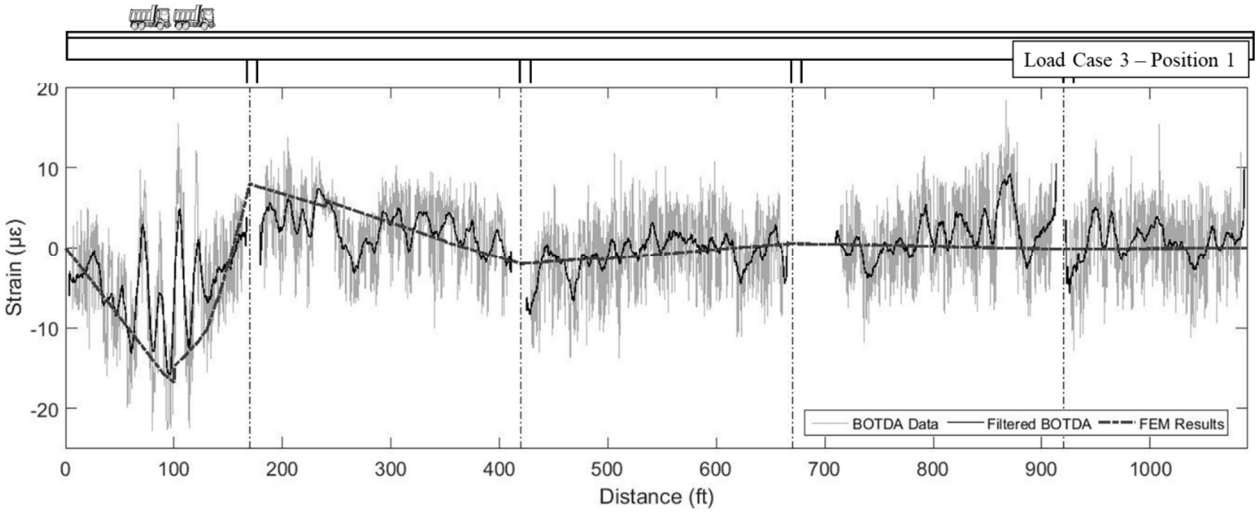

Figure 2.23 BOTDA strain measurement comparison with FEM for Case 3 – Position 1

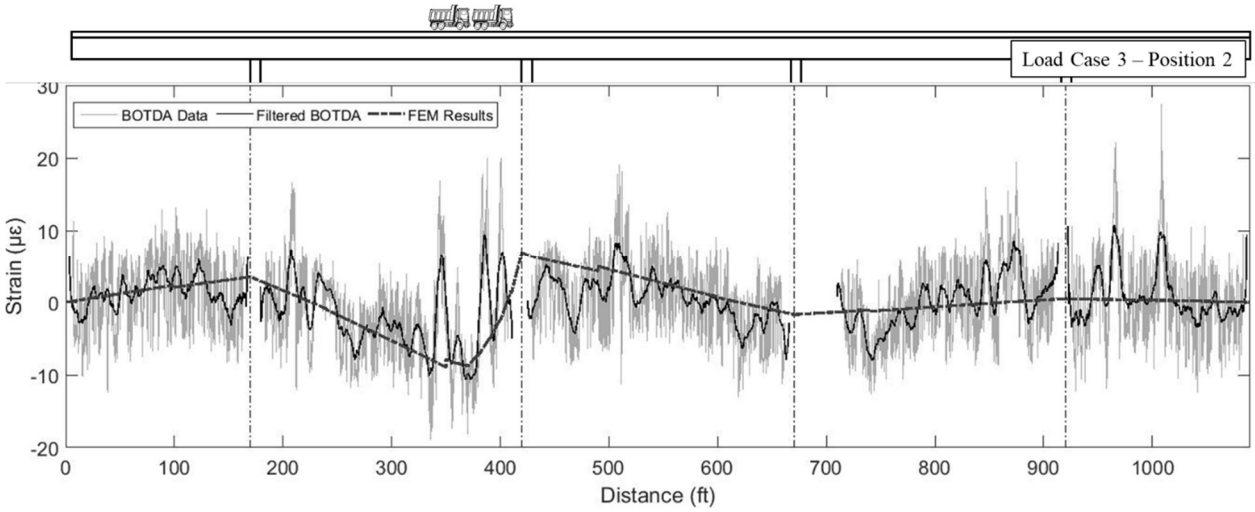

Figure 2.24 BOTDA strain measurement comparison with FEM for Case 3 – Position 2

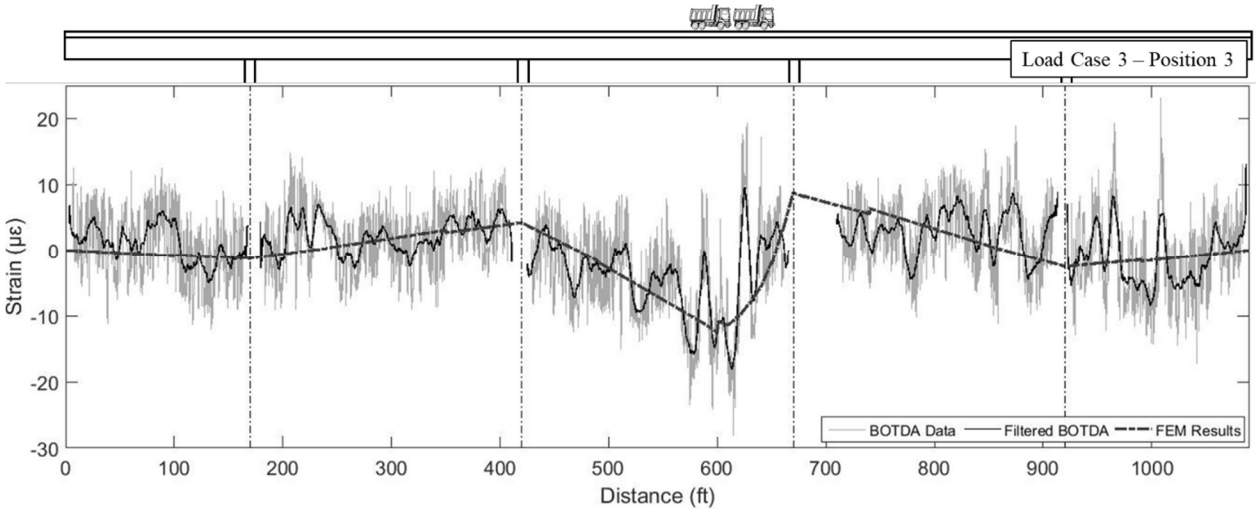

Figure 2.25 BOTDA strain measurement comparison with FEM for Case 3 – Position 3

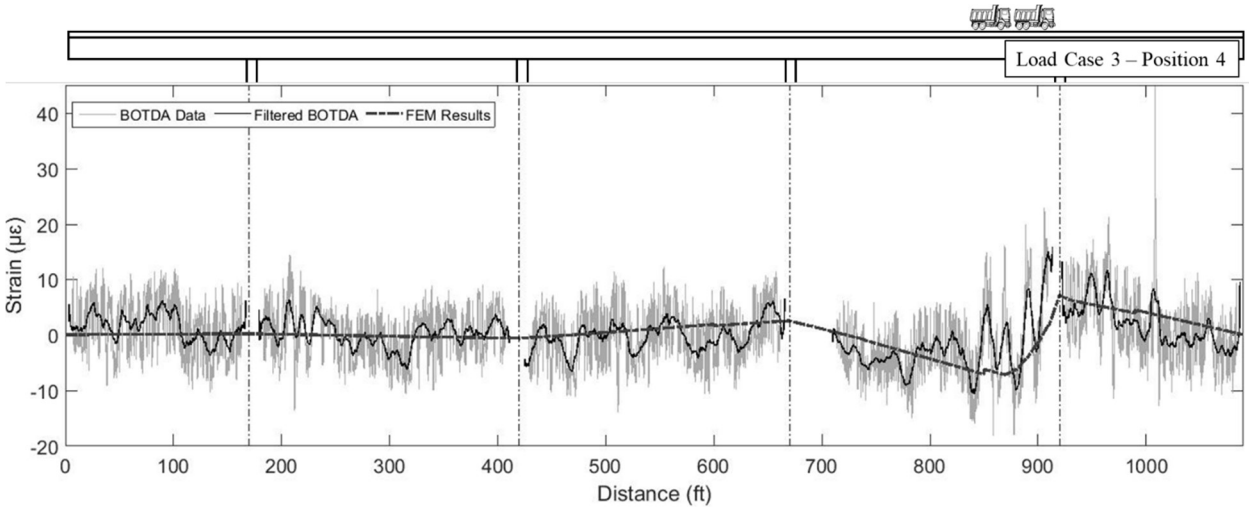

Figure 2.26 BOTDA strain measurement comparison with FEM for Case 3 – Position 4

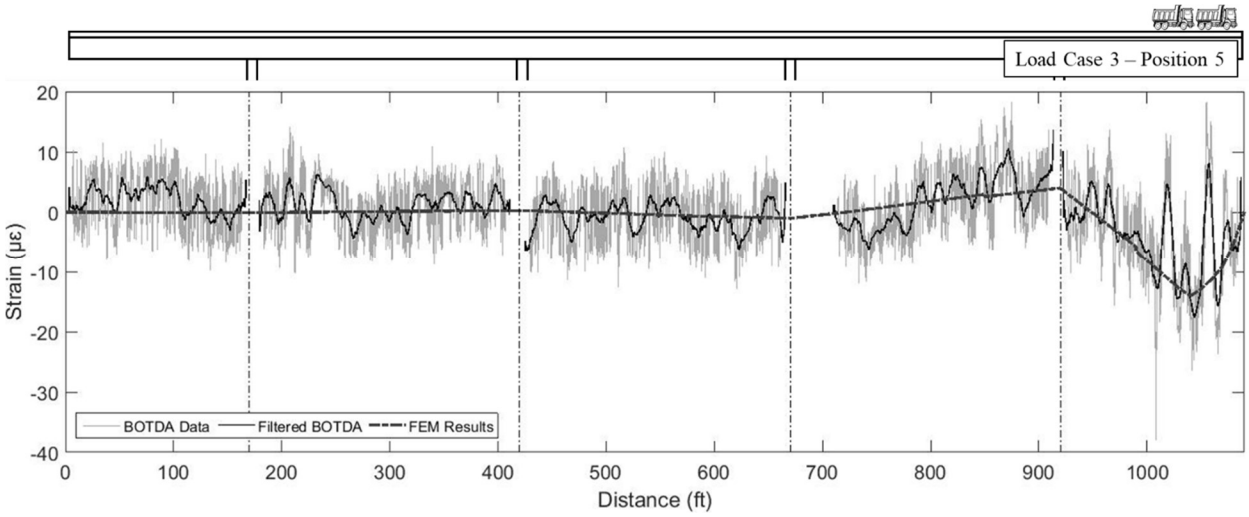

Figure 2.27 BOTDA strain measurement comparison with FEM for Case 3 – Position 5

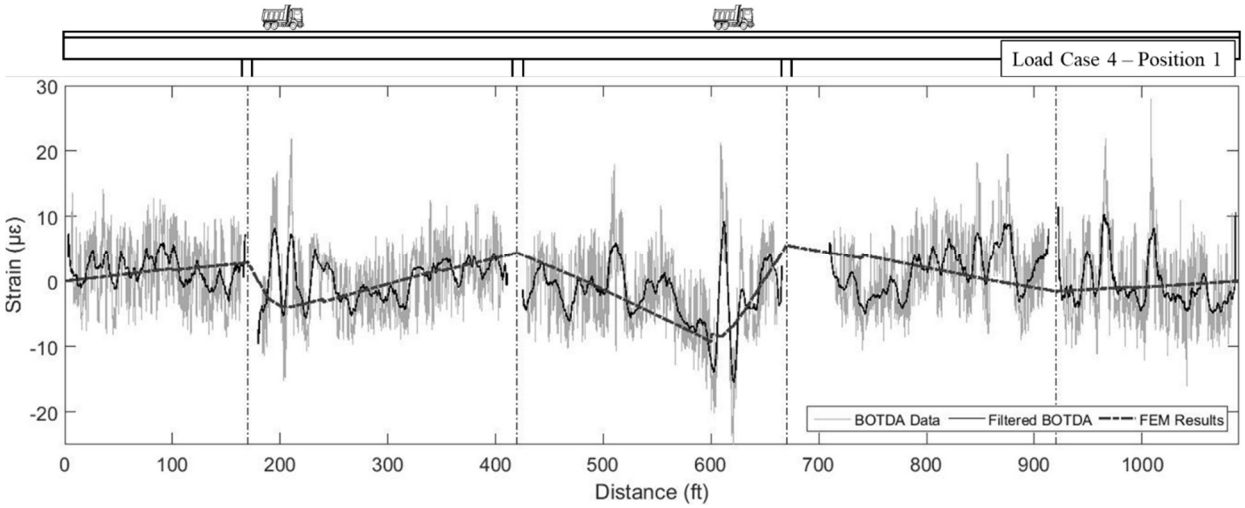

Figure 2.28 BOTDA strain measurement comparison with FEM for Case 4 – Position 1

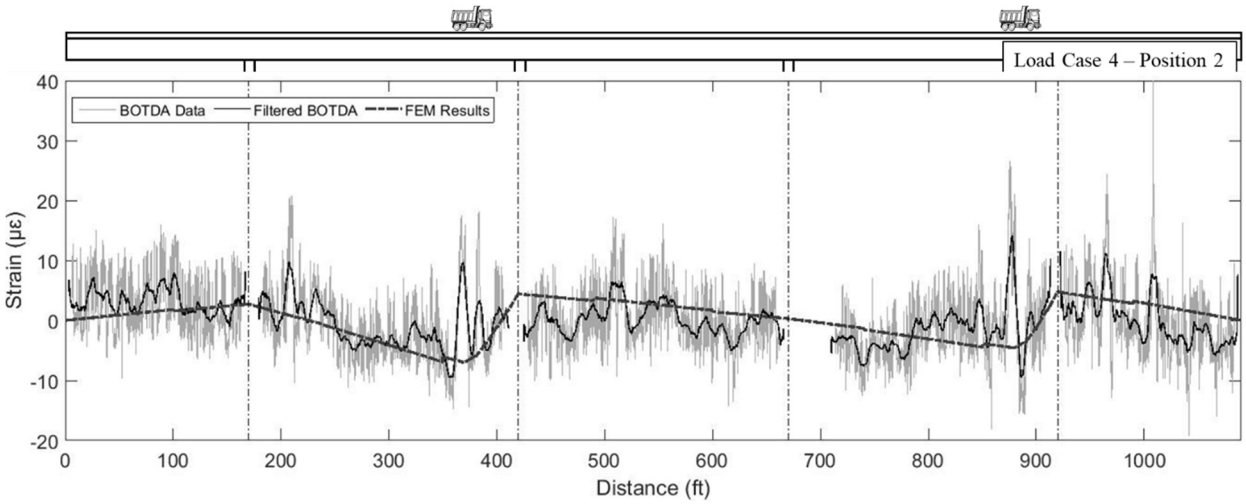

Figure 2.29 BOTDA strain measurement comparison with FEM for Case 4 – Position 2

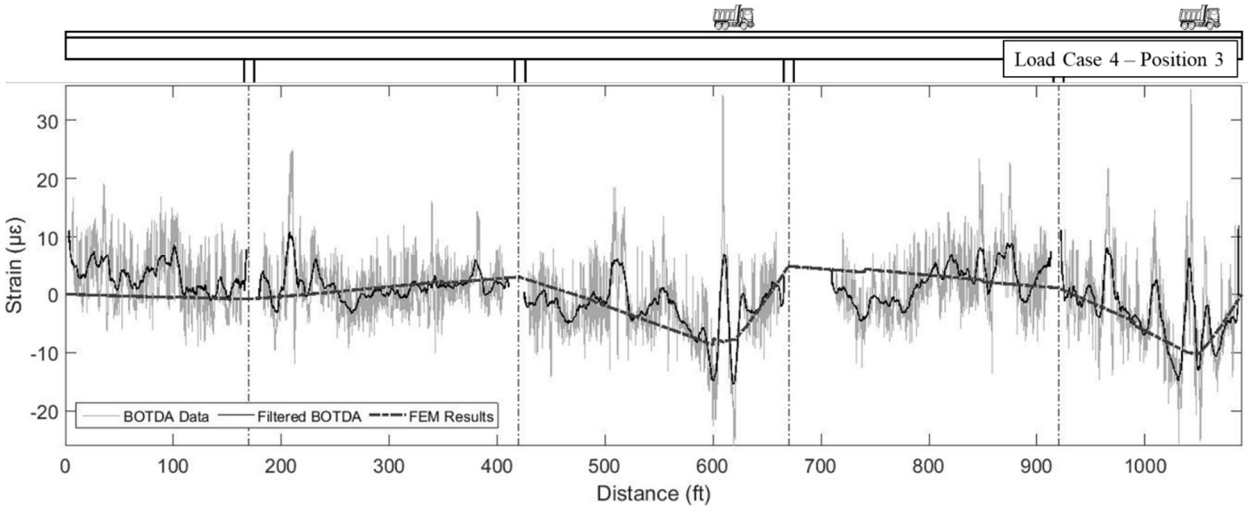

Figure 2.30 BOTDA strain measurement comparison with FEM for Case 4 – Position 3

Table 2.2 AVERAGE COMPUTED ERRORS (%)

	Load Position				
	1	2	3	4	5
Load Case 1	15.4	4.9	9.3	11.1	1.1
Load Case 2	10.9	16.4	8.1	7.1	12.2
Load Case 3	2.9	15.0	5.1	9.4	16.9
Load Case 4	2.4	3.9	8.3	N/A	N/A

Gaps in the measurements shown in figures are related to the misalignments at the intersection of some of the adjoining box girder segments. At those locations the optical fibers crossed over the misalignments and were not adhered to the box girder. As shown in these figures, truck axles produce localized peaks in the BOTDA strain response. Other peaks in strain are related to cracks, and anomalies in the

superstructure. As discussed earlier, the data contains noise making it difficult to differentiate the locations of cracks from other perturbations. Therefore, equations. (2.6) and (2.7) were employed for the computation of the ratio between measured and theoretical strains. The damage index, $\hat{\beta}_{P_i}$, and the damage index vector $[\hat{\beta}_p]$ were computed from equations. (2.9) and (2.10), respectively. Figure. 2.31 pertains to the distribution of damage index, for all the load cases, along the length of the bridge facilitating differentiation of cracks from the background noise.

As depicted in figure 2.31, case 1, 2 and 3 pertain to loading by two, three and four trucks for all load positions. Case 4 corresponds to two trucks in alternate spans (four total) for all load positions. Examination of all the damage index scenarios in figures 2.31 underlines existence of five locations where the damage index is categorically larger than the index at other locations. The locations of the identified damaged sections are marked by numerals, 1 through 5 in figure 2.31 (a). Some of the damage locations are detected in multiple scenarios, i.e. damage locations 1 and 2 in Figures. 2.31a and 2.31d, damage scenario 5 in Figures. 2.31 (a), 2.31 (b), 2.31 (c) and 2.31 (d).

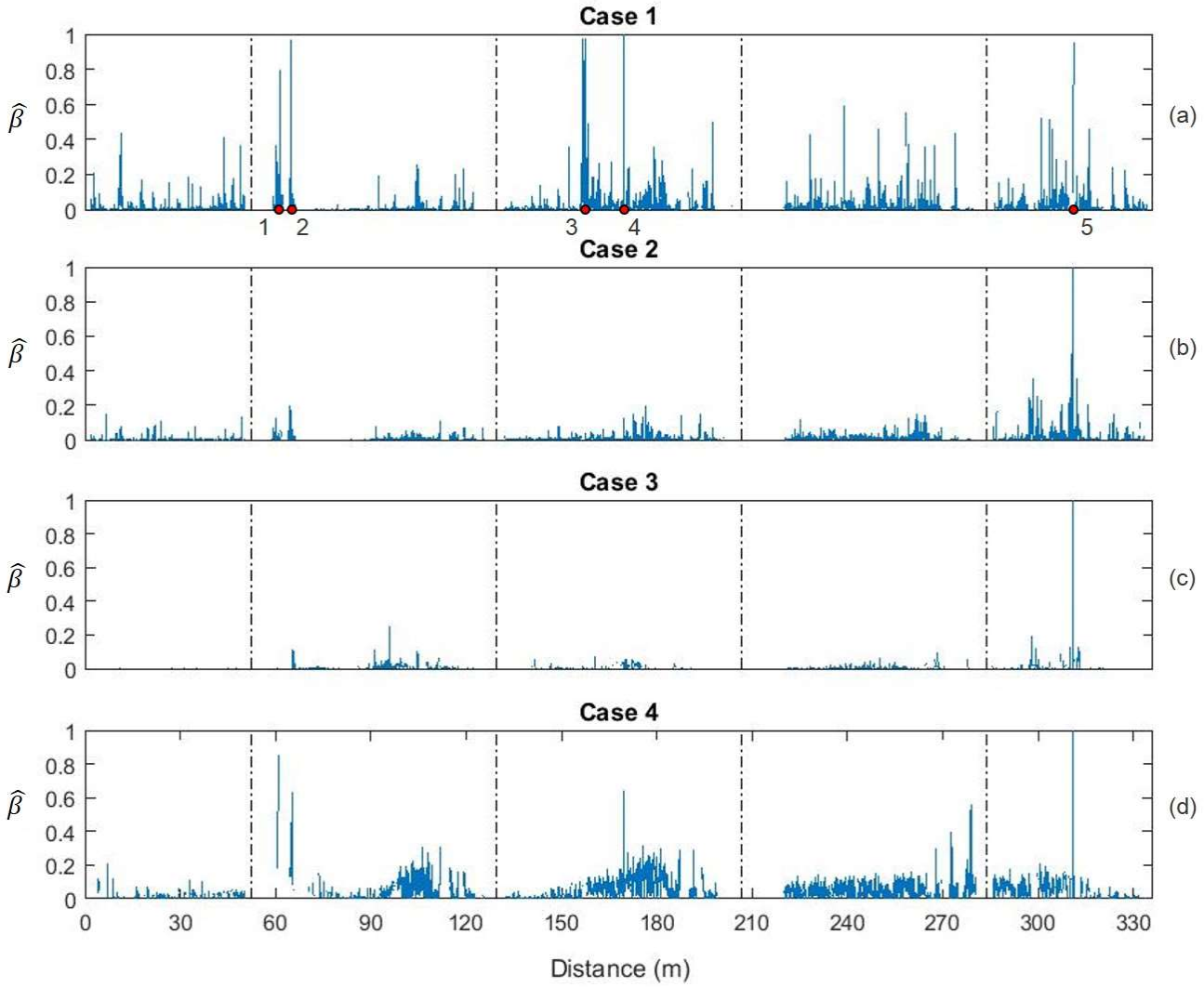

Figure 2.31 Damage Index for each load case

Table 2.3 corresponds to the location and the value of damage index in each of the four load cases. As shown in table 2.3, the damage index for location 5 on the 5th span is consistently larger than the same for other locations. A visual inspection of the

bridge indicated existence of a microcrack at that location (Location 5). The crack width was very small and it was not previously detected during the visual inspections. A marker was used to follow the crack pattern and direction as shown in Figure. 2.32.

Table 2.3 DAMAGE INDEX VALUES OF PROBABLE CRACK LOCATIONS

Point	Distance from north abutment of the bridge (m)	$\hat{\beta}$			
		Load Case 1	Load Case 2	Load Case 3	Load Case 4
1	56.60	0.793	0.127	0.016	0.850
2	59.98	0.968	0.198	0.114	0.631
3	152.33	0.974	0.038	0.010	0.056
4	164.93	1.000	0.123	0.032	0.645
5	306.32	0.950	1.000	1.000	1.000

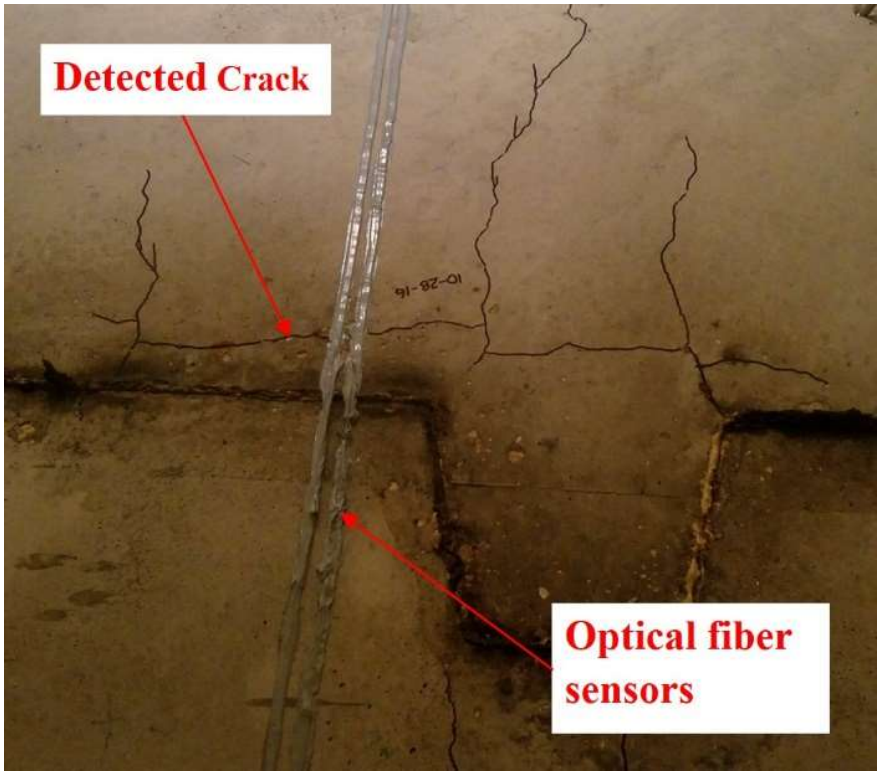

Figure 2.32 Detected crack in the fifth span (point 5)

The visual inspections verified the existence of a second crack at location 4, approximately 165 meters from the abutment of the bridge (indicated in Table 2.2). Photo of the microcrack in location 4 is shown in Figure. 2.33. Further inspection of the bridge indicated that the intensified damage indices at locations 1, 2 and 3 were due to the elevation difference between the adjacent box girder segments intensifying the strain amplitudes in those locations. Figure. 2.34 corresponds to locations 1, 2 and 3, and figure 2.35 pertains to the schematic lateral view of the elevation difference in the connected segments.

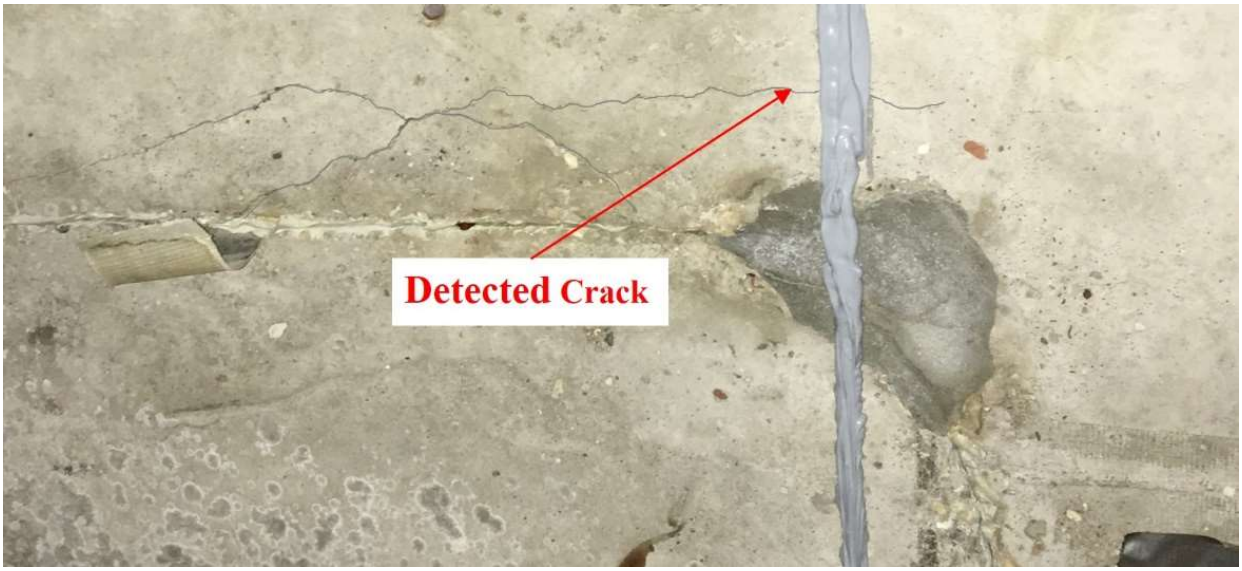

Figure 2.33 Detected crack in the third span corresponding to point 4

Figure 2.34 Connection joints corresponding to points 1, 2 and 3

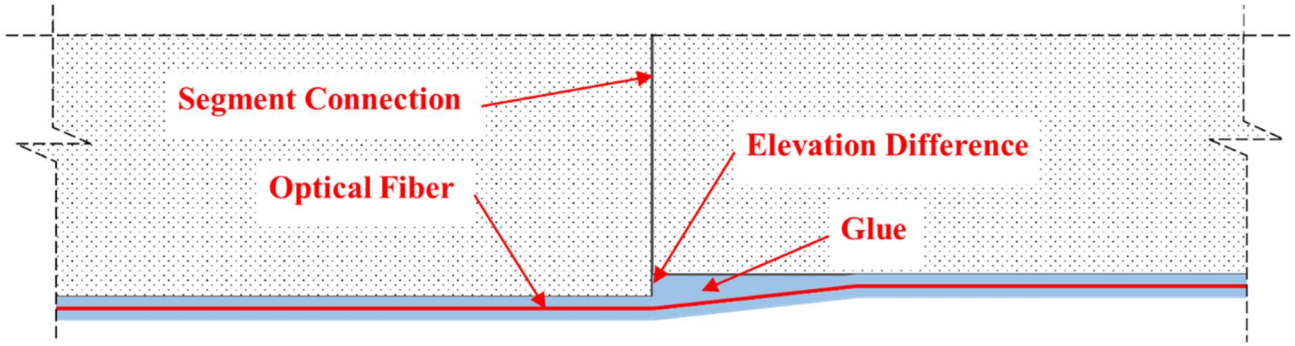

Figure 2.35 Elevation difference in connection joints

2.5. Summary of the chapter

The work described in this chapter corresponds to development and application of a method for detection of cracks in bridges by Brillouin scattering based distributed sensors. The proposed approach does not require measurements in pristine damage free state of the bridge. Identification of damage beyond the signal to noise limits of the instrument is achieved by normalization of the measured distributed strains during multiple positions of a truck with respect to the theoretical influence line of the bridge. Formulation of the method leads to the introduction of a damage index for identification of crack locations along the length of the Bridge.

The effectiveness of the proposed method was verified by load testing of a five span continuous precast post-tensioned concrete box girder bridge. An ordinary telecommunication grade optical fiber was employed for monitoring the damage along the entire 332-meter length of the Bridge. Analysis of the load test results based on the proposed method led to the identification of five locations with anomalies. Visual

inspection of the Bridge verified locations of two microcracks, and three misaligned sections at the shear keys of the box segments. Brillouin scattering based measurements are strain based and their response to cracks and other stress raisers such as misalignments between sections of the box girder are manifested by strain intensities. Therefore, they cannot differentiate between cracks and other issues unrelated to damage. Because of the inherent noise associated with Brillouin measurements, larger loads amplify the strain amplitudes and enhance the damage detection resolution of the system.

Chapter 3 . METHODS FOR MICRO-CRACKS DETECTION OF BRIDGES USING DISTRIBUTED SENSORS SUBJECTED TO DYNAMIC LOADS

3.1. Introduction

Application of BOTDA technology in structural health monitoring has been investigated in wide range of researches such as detection of tension loss in cable stayed bridges (Nazarian et al 2016; Scarella et al 2017); damage identification in reinforced concrete beams (Goldfiled and Klar 2013) and deflection calculation of bored piles adjacent to deep excavation (Mohamad et al 2011). Numerous experiments have also been conducted in the field of micro-crack detection of structures using BOTDA technology. For example, Bao et al (2016) investigated the feasibility of micro-crack detection in concrete pavements by linearly relating the magnitude of strain peaks to crack opening displacements (COD). Meng et al (2015) showed that the combination of the Brillouin frequency shift with the rise in Brillouin gain spectrum (BGS) width provides the reliable means for detection of micro cracks generating in structural surfaces. Experimental programs designed to evaluate the micro-crack detection performance of BOTDA system on concrete and steel girder bridges were also conducted subjected to static loads (Mufti et al 2011; Sun et al 2012)

This chapter investigates the applicability of distributed fiber optic sensors using BOTDA technology in detection of micro-cracks in bridges under dynamic loads. Typically, structural health monitoring using Brillouin based technology measures distributed stains of the structures in two stages. First stage is when the structures is not

loaded. The measurements recorded in this stage are called reference strains. Second stage involves recording the strains of the entire length of structure while it is subjected to dynamic or static loads. Comparison of the measured strains in first and second stage provides the location and intensity of probable micro-cracks. However, reference and static loading measurements involves traffic closure on the bridges. The proposed methodology provides the tools to eliminate the reference measurement in addition to elimination of static measurements of strains along the bridge. This method utilizes the ongoing traffic over the bridges without disturbing the traffic to detect probable micro-crack locations along the structures. The method which is introduced in this chapter, compares the strains differential in theory strain differentials in time domain while the dynamic loads cross over the bridge. The applicability of the method was put into test by experimenting it on two different bridges. Experimental program details and discussion on the results are provided in this chapter as well.

3.2. Method Introduction

Acquired strains at any sampling point on optical fiber used in the distributed sensing technology, ε_P, consists of a combination of temperature strains ε_T, dynamic loads strains ε_D, initial setup strains ε_i and possible crack induced strains ε_C.

$$\varepsilon_P = \varepsilon_T + \varepsilon_D + \varepsilon_i + \varepsilon_C \tag{3.1}$$

Temperature strains are generated from changes of temperature in the fiber. This effect should always be considered in data acquisition. There are two common ways to compensate the effect of temperature and eliminate the changes of strains due to this parameter. First approach involves measurements that are conducted in a short period

of time where the changes of temperature are negligible. Second approach is to utilize a loose fiber simultaneously with the main fiber for measurements of temperature strains only.

Strains generated from dynamic loads are considered to be resulting from moving loads which is the passing trucks over the bridge in this case. Initial setup strains are generated from the fiber pre-tensioning during installation. Optical fiber used as the distributed sensor is just capable of going through to eliminate this problem, pre-tensioning is applied to the fiber while installing it on any structure. Therefore, any compression in structure will be measured as a loss in tension.

Crack induced strains, which are usually detected as peaks in the strain profiles, are resulting from the crack opening displacements and are not permanently recorded in the measurements. Amount of these strains varies due to the applied load and the crack opening displacement.

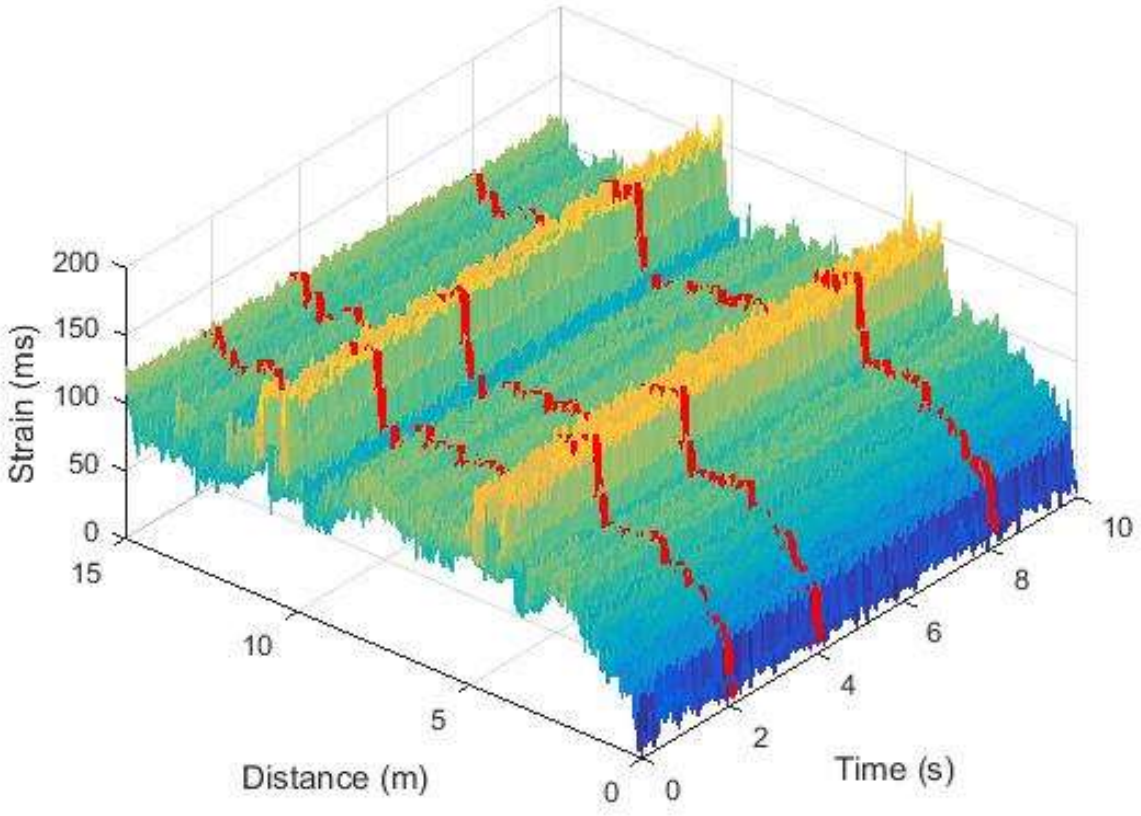

Figure 3.1 Example of distributed strains in distance and time domain

Figure 3.1 shows an example of the combination of all the mentioned strains in spatial and time domain. X axis corresponds to the distance of every single sampling point along the fiber, Y axis represents the changes of strains through time and Z axis represent the values of strain.

Measured strains in time and distance domain, $[\varepsilon^M]_{m\times n}$, can be represented in a matrix form as below:

$$[\varepsilon^M]_{x_i,t_j} = \begin{bmatrix} \varepsilon^M_{x_1,t_1} & \cdots & \varepsilon^M_{x_1,t_n} \\ \vdots & \ddots & \vdots \\ \varepsilon^M_{x_m,t_1} & \cdots & \varepsilon^M_{x_m,t_n} \end{bmatrix} \quad (3.2)$$

This strain matrix is a m by n matrix where m is the number of sampling points along the fiber and n is the number of generated files through time in the process of measurement. Superscript M stands for measured strains. Therefore, $\varepsilon^M_{x_m,t_n}$ is the measured strain of an arbitrary sampling point at the instance of t_n, which is located at the distance of x_m.

The frequency of measurement can be calculated by dividing the total number of recorded files (n) by the total time of measurement.

For any instance of time, like t_i, a section of this three dimension profile can be extracted which represents a strain profile of the whole structure. Strain profiles for time instances of 2, 4 and 8 seconds are also shown in Figure. 3.1 as an example. Measured strain profile of the structure at any single instance of time, $[\varepsilon^M]_{t_i}$, can be presented as a vector shown below:

$$[\varepsilon^M]_{t_i} = \begin{bmatrix} \varepsilon^M_{x_1,t_i} \\ \varepsilon^M_{x_2,t_i} \\ \vdots \\ \varepsilon^M_{x_m,t_i} \end{bmatrix} \quad (3.3)$$

If the structure of interest is a continuous bridge and the applied loads are the trucks passing over the bridge then the key strain profiles are for the time instances where the moving trucks are located at the middle of each spans. While the dynamic loads or trucks are at the middle of spans, deflection and therefore moments along the bridge are

at their maximum. Measured strain profiles at this instance of time may be stated as follows:

$$[\varepsilon^M]_{t_{sp(j)}} = \begin{bmatrix} \varepsilon^M_{x_1,t_{sp(j)}} \\ \varepsilon^M_{x_2,t_{sp(j)}} \\ \vdots \\ \varepsilon^M_{x_m,t_{sp(j)}} \end{bmatrix} \tag{3.4}$$

Where $sp(i)$ denoted j[th] span, $[\varepsilon^M]_{t_{sp(j)}}$ is the measured strain profile along the bridge and $\varepsilon^M_{x_m,t_{sp(j)}}$ is the measured strain of a point with distance of x_m at the time instance where the load is at the j[th] span.

For every single sampling point along the fiber the differences of measured strain due to two adjacent span loading positions, $[\Delta\varepsilon^M]_{j+1,j}$, are defined as below:

$$[\Delta\varepsilon^M]_{j+1,j} = [\varepsilon^M]_{t_{sp(j+1)}} - [\varepsilon^M]_{t_{sp(j)}} = \begin{bmatrix} \varepsilon^M_{x_1,t_{sp(j+1)}} - \varepsilon^M_{x_1,t_{sp(j)}} \\ \varepsilon^M_{x_2,t_{sp(j+1)}} - \varepsilon^M_{x_2,t_{sp(j)}} \\ \vdots \\ \varepsilon^M_{x_m,t_{sp(j+1)}} - \varepsilon^M_{x_m,t_{sp(j)}} \end{bmatrix} \qquad (j = 1,2,\dots k) \tag{3.5}$$

Where k is the number of bridge spans. Similar to the measured strains, theoretical strains are calculated and presented in the same way. The method for calculating the theoretical strains based on the moment influence line is described in the previous chapter. Theoretical strain profile of an arbitrary instance of time, $[\varepsilon^T]_{t_i}$, is presented as the following vector:

$$[\varepsilon^T]_{t_i} = \begin{bmatrix} \varepsilon^T_{x_1,t_i} \\ \varepsilon^T_{x_2,t_i} \\ \vdots \\ \varepsilon^T_{x_m,t_i} \end{bmatrix} \tag{3.6}$$

Where $\varepsilon^T_{x_m,t_i}$ is the strain of point in a distance of x_m, at the time instance of t_i. The superscript T stands for the theoretical calculations. Similar to measured strains, differences between theoretical differences for every sampling point along the fiber for two adjacent loading span positions, $[\Delta\varepsilon^T]_{j+1,j}$, are calculated as follows:

$$[\Delta\varepsilon^T]_{j+1,j} = [\varepsilon^T]_{t_{sp(j+1)}} - [\varepsilon^T]_{t_{sp(j)}} = \begin{bmatrix} \varepsilon^T_{x_1,t_{sp(j+1)}} - \varepsilon^T_{x_1,t_{sp(j)}} \\ \varepsilon^T_{x_2,t_{sp(j+1)}} - \varepsilon^T_{x_2,t_{sp(j)}} \\ \vdots \\ \varepsilon^T_{x_m,t_{sp(j+1)}} - \varepsilon^T_{x_m,t_{sp(j)}} \end{bmatrix} \quad (3.7)$$

Where $[\varepsilon^T]_{t_{sp(j)}}$ is the theoretical strain profile of the bridge in the time instance when the moving trucks are located at the middle of the j[th] span. $\varepsilon^T_{x_m,t_{sp(j)}}$ is the theoretical strain at a point in a distance of x_m when the loading trucks are located at the middle of the j[th] span.

Comparison of theoretical and measured strain differentials due to two adjacent span loading positions is achieved by calculating the ratios between them. This ratio, $\alpha^j_{x_i}$, is derived by the following equation:

$$\alpha^j_{x_i} = \frac{\varepsilon^M_{x_i,t_{sp(j+1)}} - \varepsilon^M_{x_i,t_{sp(j)}}}{\varepsilon^T_{x_i,t_{sp(j+1)}} - \varepsilon^T_{x_i,t_{sp(j)}}} = \frac{(\Delta\varepsilon^M_{x_i})_{t_{sp(j+1)},t_{sp(j)}}}{(\Delta\varepsilon^T_{x_i})_{t_{sp(j+1)},t_{sp(j)}}} \qquad (j = 1,2,\dots,k-1) \quad (3.8)$$

If this ratio is 1, it means that the changes of strains measured by BOTDA is the same as changes of theoretically calculated strains and therefore no crack or damage should have been developed at that sampling point. As the ratio increases the probability of presence of a crack or a change in sectional area increases. The number of $\alpha^j_{x_i}$ calculated for each sampling point is 1 less than the total number of spans, k. The effect

of all the $\alpha_{x_i}^j$ coefficients are then combined into a single value. Crack index $\hat{\beta}_{x_i}$, for each sampling point is defined by multiplying these ratios, and normalizing the calculated vector as follows:

$$\beta_{x_i} = \prod_{n=1}^{k-1} \alpha_{x_i}^n = \alpha_{x_i}^1 \times \alpha_{x_i}^2 \times \ldots \times \alpha_{x_i}^n \tag{3.9}$$

$$[\hat{\beta}] = \frac{1}{(\beta_{x_i})_{max}} \begin{bmatrix} \beta_{x_1} \\ \beta_{x_2} \\ \vdots \\ \beta_{x_m} \end{bmatrix} = \begin{bmatrix} \hat{\beta}_{x_1} \\ \hat{\beta}_{x_2} \\ \vdots \\ \hat{\beta}_{x_m} \end{bmatrix} \tag{3.10}$$

Crack index vector $[\hat{\beta}]$ is constructed from the individual crack indices for every single sampling point throughout the sensor, $\hat{\beta}_{x_i}$. Since crack index is normalized, it varies between zero and one. Higher values of crack index may indicate presence of crack at that specific sampling point.

Application of this method is put into test by acquiring a distributed strain data following a dynamic load test. The details on the description of the bridges, sensor installation and data acquisition and measurement techniques are explained next.

3.3. Test Programs

3.3.1 Description of the bridges

3.3.1.1 Kishwaukee bridge

The first experimental test is conducted on the southbound bridge as one of the twin Kishwaukee River bridges shown in figure 3.2. Sectional properties and information of the bridge is provided at chapter 2.

Figure 3.2 Kishwaukee River Bridge - Southbound

3.3.1.2 Thornton quarry bridge

Thornton quarry bridge is located at Thornton, Illinois just south of Chicago, IL (Figure 3.3). This Tri-State tollway bridge carries over the traffic of interstate I-294. Superstructure is three spans of non-composite continuous riveted and welded steel plate girder with a 50 m (164 ft) center span and 24.3 m (80 ft) end spans with a reinforced concrete bridge deck. Total length of the bridge is 98.7 m (324 ft). Width of the superstructure is 23.6 m (77.58 ft). Cross section of the bridge is shown in figure. 3.3. Superstructure of the bridge consists of 10 girders with 2.4 m (7.9 ft) space in between each other. Height and thickness of the girders' web are 1.98 m (6.5 ft) and 1.4 cm (0.56 in) respectively. Width and thickness of the girder flanges are 40 cm (16 in) and 2.54 cm (1 in) respectively. Thickness of the reinforced concrete deck is 19 cm (7.5 in).

Figure 3.3 Thornton Quarry bridge

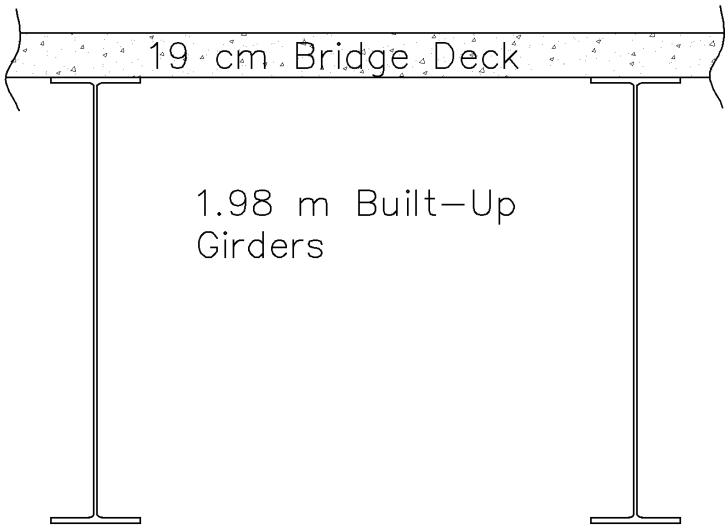

Figure 3.4 Cross section of the Thornton Quarry bridge

Concrete used for the superstructure had 27579 kN/m^2 (4000 psi) strength at 14 days. Concrete with a strength of 24131 kN/m^2 (3500 psi) was used for substructure,

Yield strength of reinforcement and the structural steel were 413685 kN/m^2 (60000 psi) and 344737 kN/m^2 (50000 psi) respectively.

3.3.2 Instrumentation

Corning's SMF-28 telecommunication grade optical fiber was employed as a distributed sensor for data acquisition purposes in both bridges. This single mode fiber has a core diameter of 9 μm, cladding diameter of 125 μm and coating diameter of 250 μm. The optical fiber was adhered to the inner section of the top deck by a silicon adhesive as shown in Figure. 3.5. The fiber was pre-tensioned during the installation. Neubrescope NBX-6055 was employed as the data acquisition and processing device.

Installation was continuous throughout the entire length of the bridge and all the five spans of the Kishwaukee bridge were covered with the distributed sensor. As for the Thornton quarry bridge, the distributed optical fiber sensor was attached under the concrete deck between the 7th and 8th girder in the first span. In addition to the deck, the optical fiber sensor was also installed on the bottom flange of the 7th girder. The installation is shown in Figures 3.6 through 3.9.

Three accelerometers were installed 27.4 m (90 ft), 42.6 m (140 ft) and 38.1 m (125 ft) away from the left abutment, first pier and second pier of the Kishwaukee bridge respectively. The installation location of the accelerometers was selected based on the modal shapes of the structure.

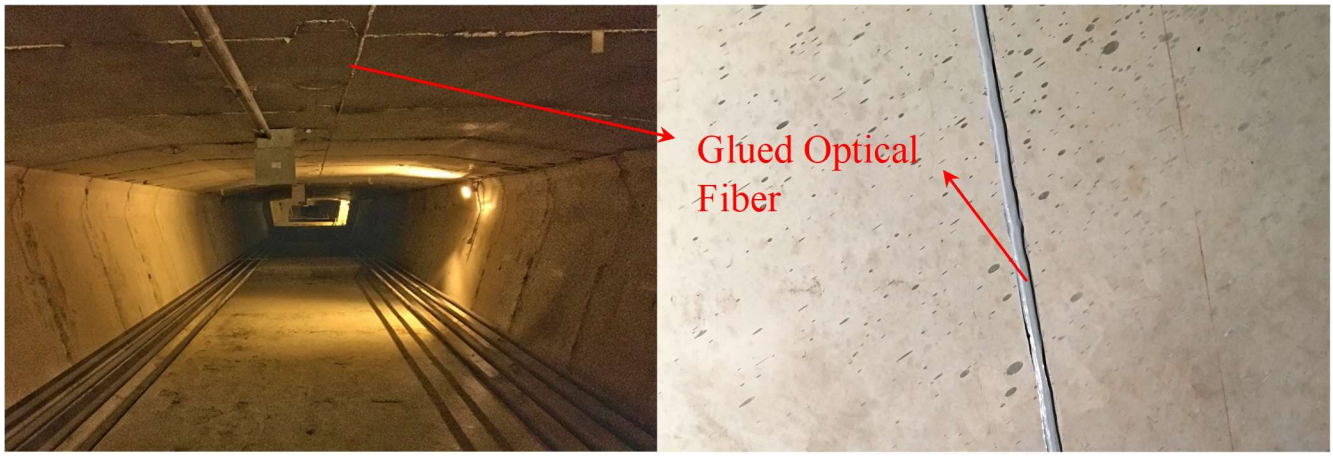

Figure 3.5 Location of the glued optical fiber on the Kishwaukee bridge

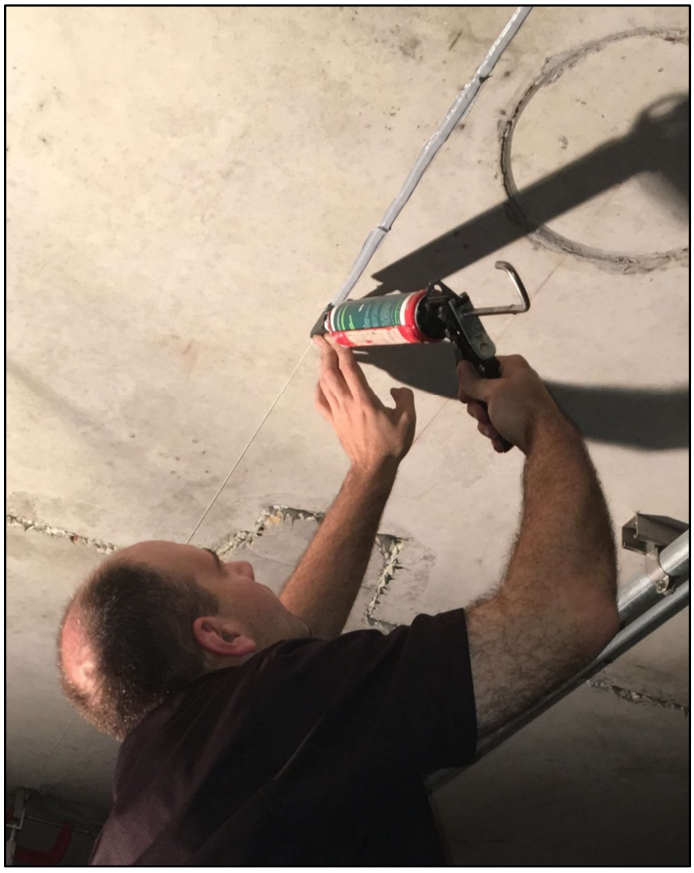

Figure 3.6 Installation of optical fiber on the Kishwaukee bridge

Figure 3.7 Initial setup for installation of optical fiber on the Thornton Quarry bridge

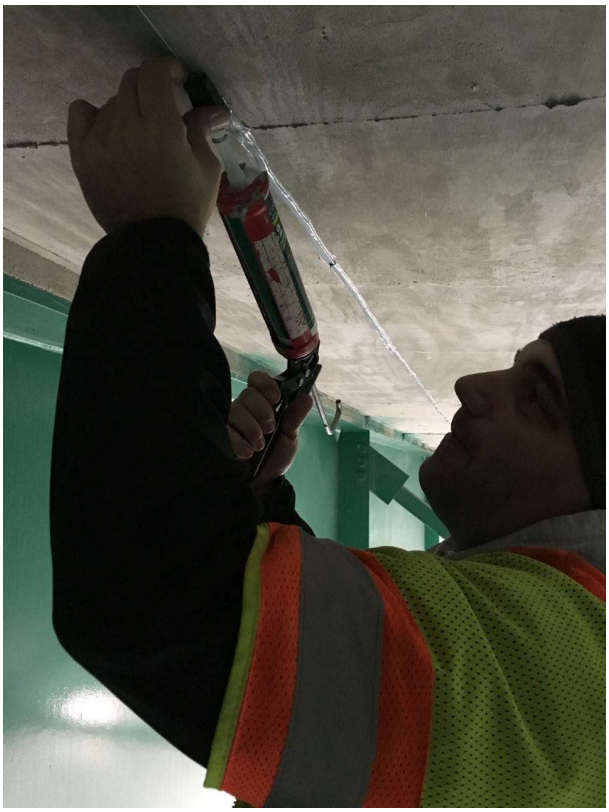

Figure 3.8 Installation of optical fiber on the Thornton Quarry bridge

Figure 3.9 Location of the glued optical fiber on the Thornton Quarry bridge

3.3.3 Dynamic load test

3.3.3.1 Kishwaukee bridge

Dynamic load test on the Kishwaukee bridge consisted of two calibrated moving trucks passing over the bridge in the south direction parallel to each other with the speed of 8.94 m/s (20 mph). The calibrated truck which is shown in Figure 3.10. had a gross vehicle weight of 204.6 kN (46 kips). The front axle weighed 35.6 kN (8 kips). Axles 2 and 3 weighed 88.9 kN (20 kips) and 80 kN (18 kips) respectively.

Figure 3.10 Calibrated truck

Sampling interval for the dynamic data acquisition is 10 cm with 20 cm spatial resolution and 2^{10} for measurement averaging. 3000 sets of distributed strain data are recorded in 50 seconds leading to the measurement frequency of 59.48 Hz. The combination of this sampling interval with spatial resolution is used to obtain the highest accuracy with minimum noise introduced to the measurement.

3.3.3.2 Thornton quarry bridge

The strain data from the distributed optical fiber sensors on the Thornton quarry bridge was recorded under the dynamic loads of regular traffic. Therefore, no controlled traffic or calibrated trucks were used during the tests. 8 separate measurements were taken under random traffic loads. Sampling interval and spatial resolution for the tests were set to is 5 cm with 20 cm respectively with 2^{10} for measurement averaging. 3000

sets of distributed strain data were recorded in 22 seconds for each measurement leading to the measurement frequency of 136.36 Hz. Higher recording frequency was used in this test since the speed on the regular traffic was higher in comparison to the Kishwaukee bridge test.

3.3.4 Finite Element Model

Calculating the modal shapes and frequencies of the Kishwaukee bridge was achieved by comparing the results with a finite element model created with the commercial software, CSI Bridge. Eight node solid elements are used for modeling the superstructure along with tendon elements for modeling pre-stressed and post tensioned tendons. Section dimensions and material properties for modeling are obtained from the original bridge drawings.

3.4. Test Results

3.4.1 Kishwaukee Bridge

3.4.1.1 Modal Shapes and Frequencies

The accelerometers' measurements were recorded while the calibrated trucks passed over the bridge. Calculating the modal frequencies of the bridges was achieved by applying the Fast Fourier Transform on the recorded data. Modal shapes and frequencies were also generated by the finite element model, analyzed by the CSI Bridge software. Figure 3.11 shows the first three modal shapes and frequencies derived from the FEM analysis. First, second and third modes have the frequencies of 1.54, 1.93 and

2.43 Hz respectively. It should be noted that all the modal shapes and frequencies are in the vertical direction.

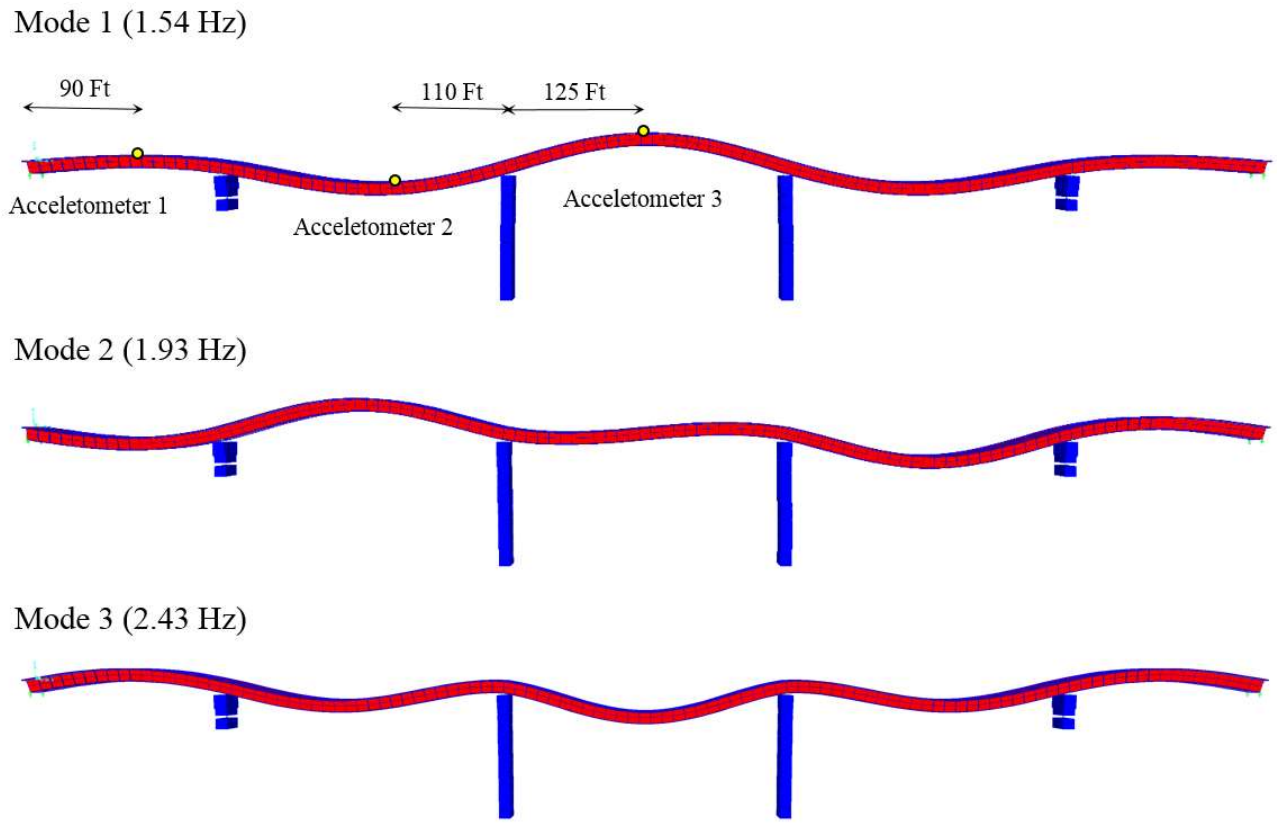

Figure 3.11 Modal shapes and frequencies of Kishwaukee bridge

Figures 3.12 to 3.14 show the FFT results of the three accelerometers' measurements. The frequencies derived for the first three modes are 1.64, 2.10 and 2.72 Hz respectively. The differences of calculated frequencies for the first three modal shapes through field measurements and finite element analysis were 6.0, 8.8 and 11.9 percent. Comparison between the two outcomes shows the fact that the structure has stayed and

performs in the linear elastic phase and all the theoretical calculations which is based on the linear elastic theory applies to the structure.

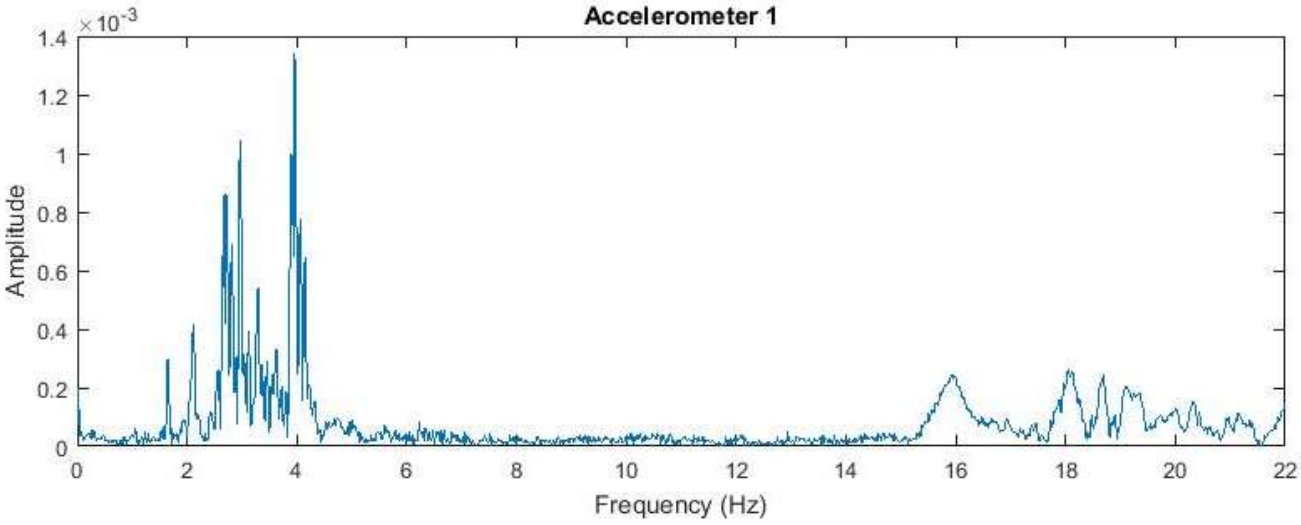

Figure 3.12 Fast Fourier Transform of the first accelerometer

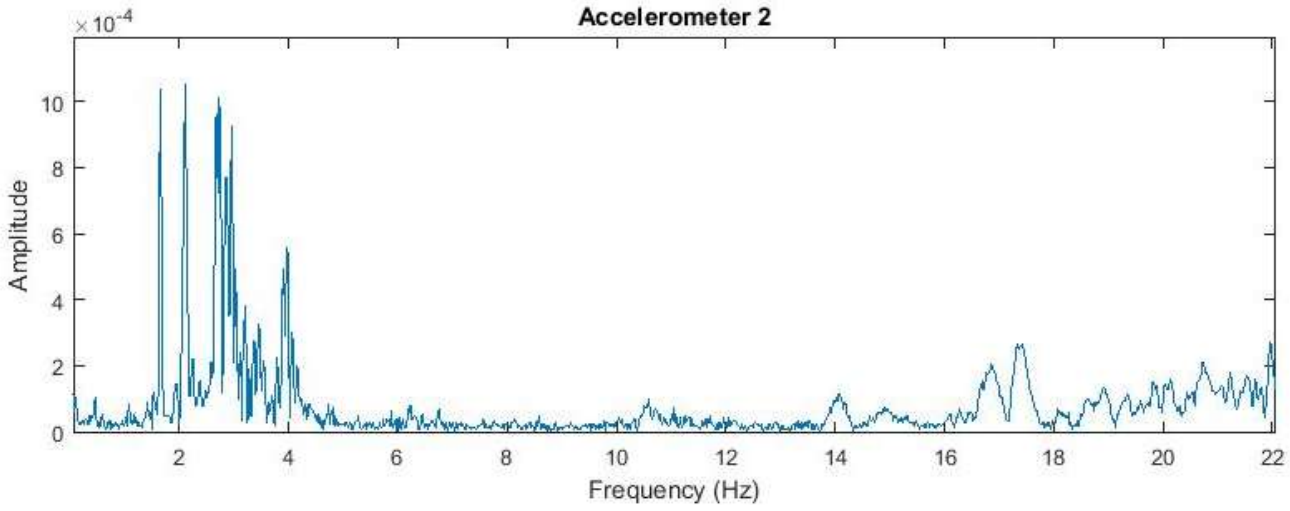

Figure 3.13 Fast Fourier Transform of the second accelerometer

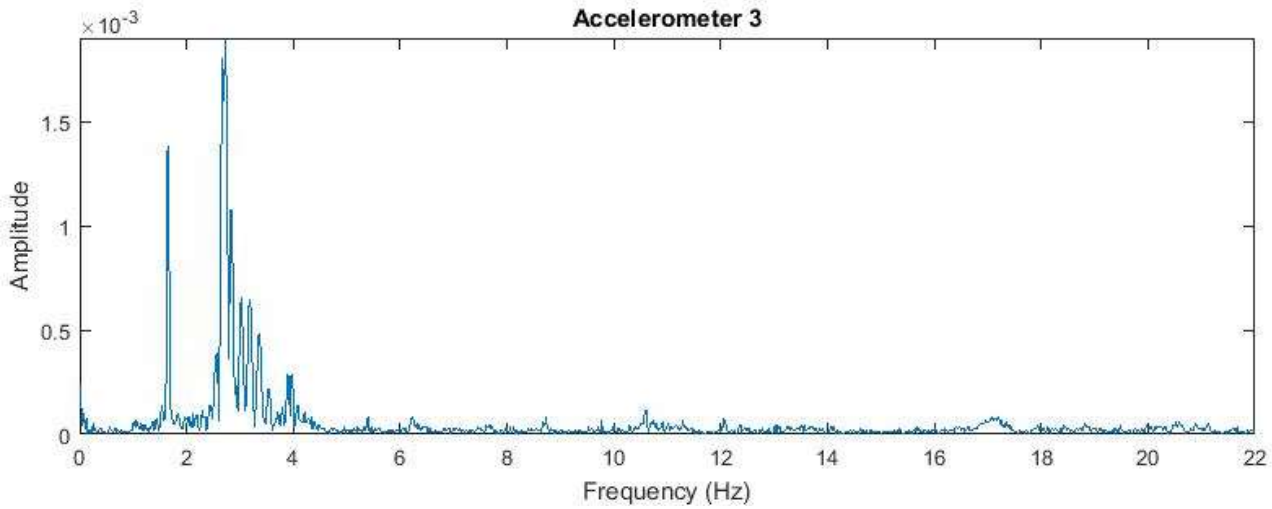

Figure 3.14 Fast Fourier Transform of the third accelerometer

3.4.1.2 Strain measurements

The unfiltered distributed strains throughout the entire length of the Kishwaukee bridge are shown in figure 3.15. X, Y and Z axes are time and sampling numbers and strain respectively.

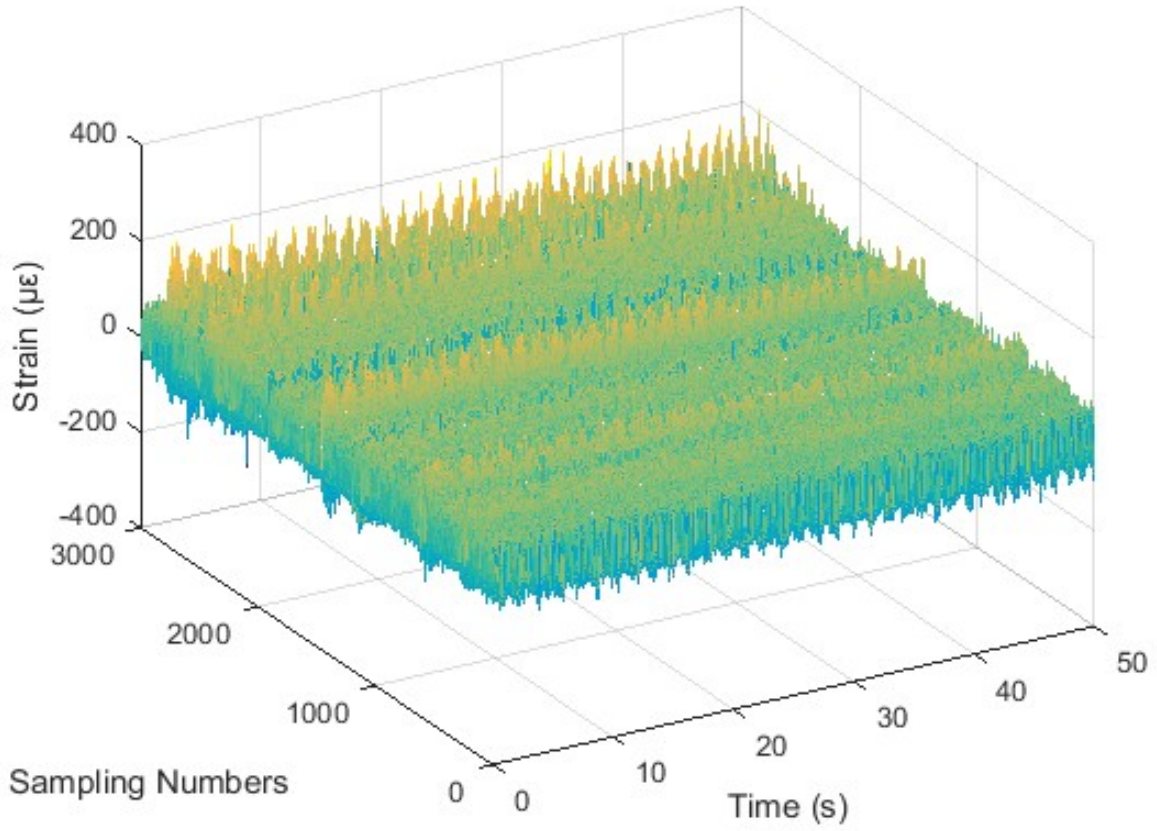

Figure 3.15 Distributed strain data of the Kishwaukee bridge over time

Knowing the location of calibrated trucks in time is essential for extracting the strain profiles for instances of time where trucks are in the middle of each span. Therefore, the load path of the passing trucks should be calculated for the measured strains. Deriving out the live load path was achieved by taking advantage of local tensions created by the truck wheels under the deck. Sectional stresses of the superstructure while the trucks are located at the middle of the second span are shown in Figure 3.16.

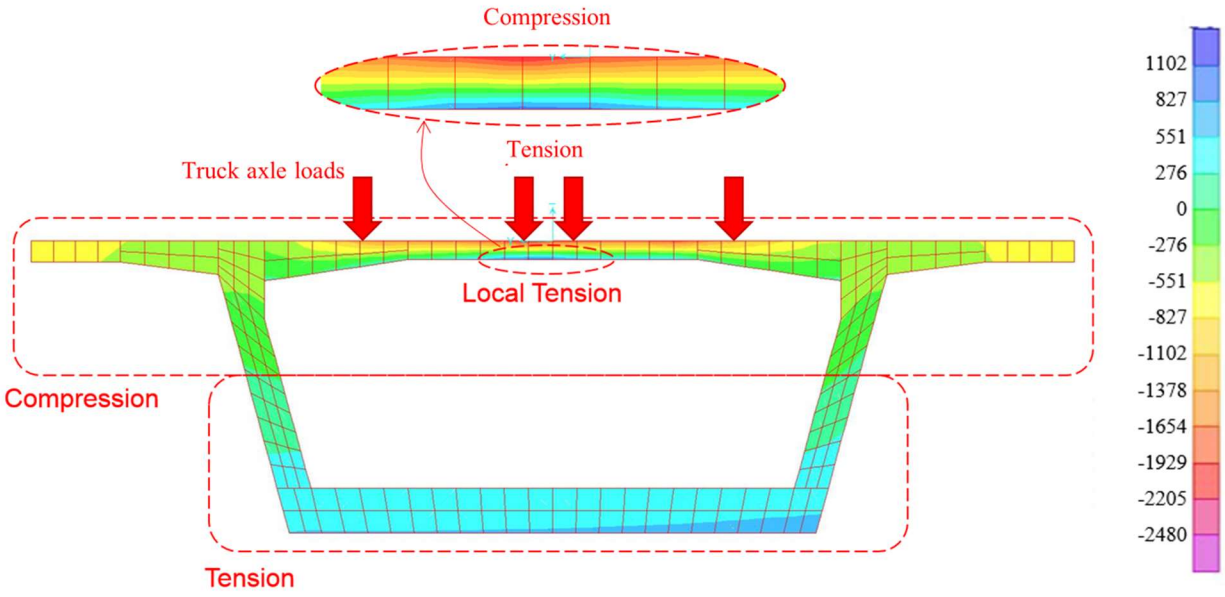

Figure 3.16 Sectional stresses under truck axle (kPa)

As it is depicted, due to the concentrated wheel loads, bottom surface of the upper deck goes under local tension. This tension is generated where the distributed optical fiber sensor is installed. Applying moving average to the measured strains reveals these local strains. The diagonal line depicted in figure. 3.17 is showing that the trucks entered the bridge 3 seconds into the recording and left the bridge at around 40th second.

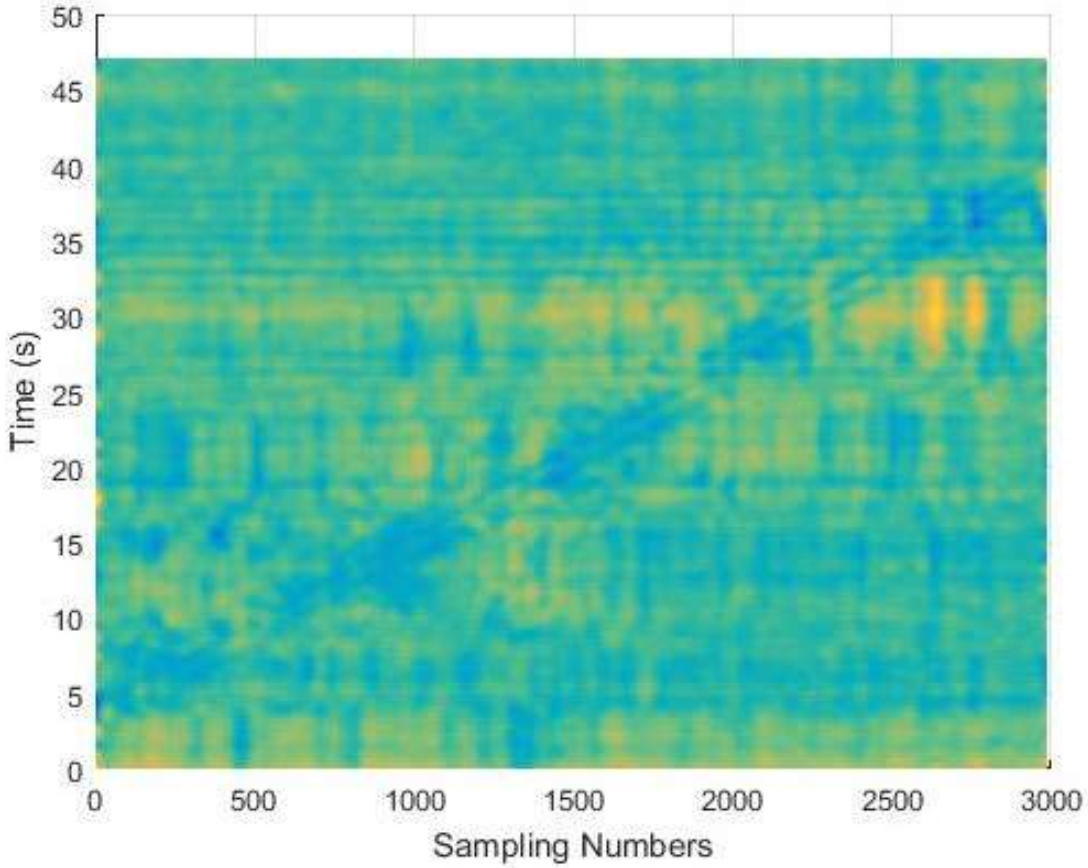

Figure 3.17 Filtered distributed strains of the entire bridge in time

To extract the load path and its equation, a threshold is applied to filtered distributed strains and the outcome is shown in figure. 3.18. The live load path's moving equation is derived using a linear regression analysis. Inverse slope of the line is the speed of the calibrated trucks passing over the bridge. In this specific case, the calculated speed is 1/0.11=9.09 m/s (20.33 mph) which is only 1.6% different from the reported test speed of 8.94 m/s (20 mph).

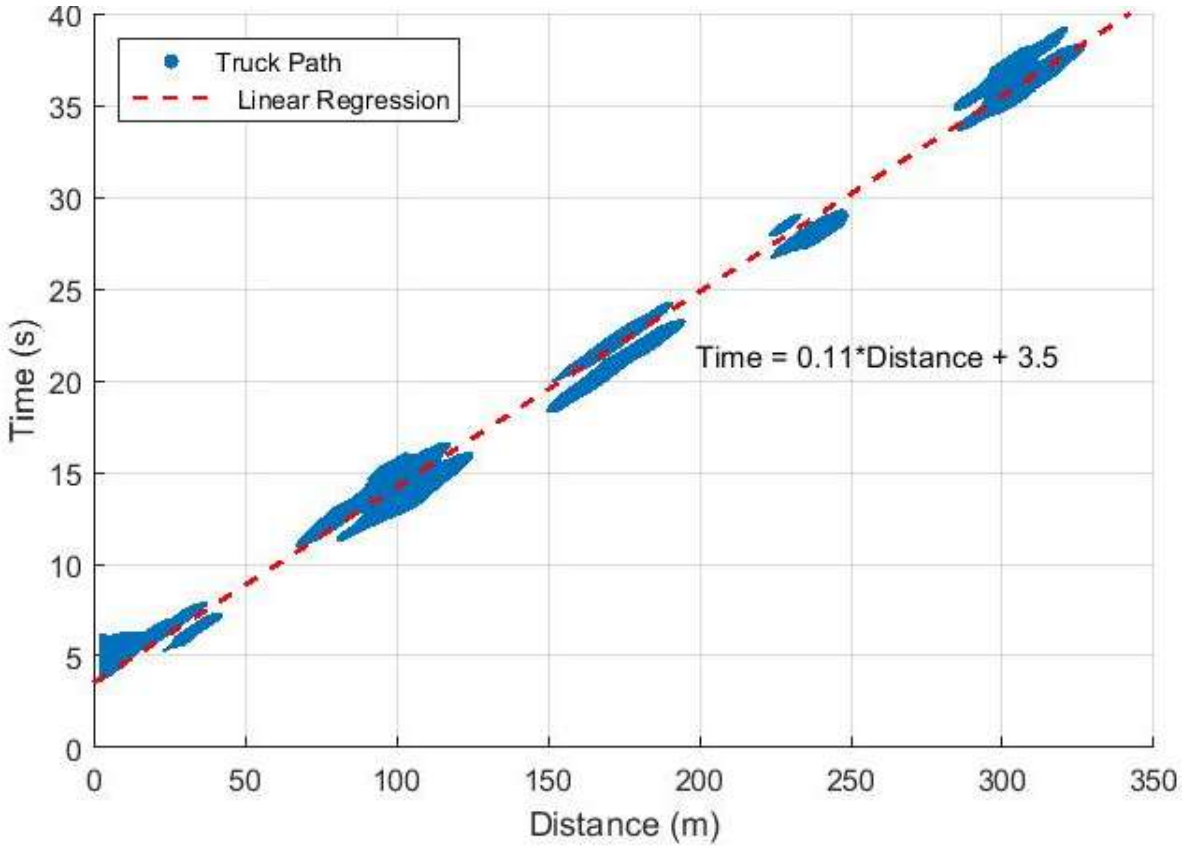

Figure 3.18 Linear regression formula for load path derivation

Since the location of the trucks in time is known based on the derived load path equation, strain profiles of the entire length of the bridge can be extracted from the initial time-distance strains, when the trucks are located in the middle of each span. Based on this equation, $[\varepsilon^M]_{t_{sp(1)}}$, $[\varepsilon^M]_{t_{sp(2)}}$, …, $[\varepsilon^M]_{t_{sp(5)}}$ from equation. 3.4 are extracted. Selected strain profiles when trucks are located at the first and fourth span are depicted in figure. 3.19. Theoretical strains corresponding to loading positions in the middle of each spans are also calculated as $[\varepsilon^T]_{t_{sp(1)}}$, $[\varepsilon^T]_{t_{sp(2)}}$, …, $[\varepsilon^T]_{t_{sp(5)}}$.

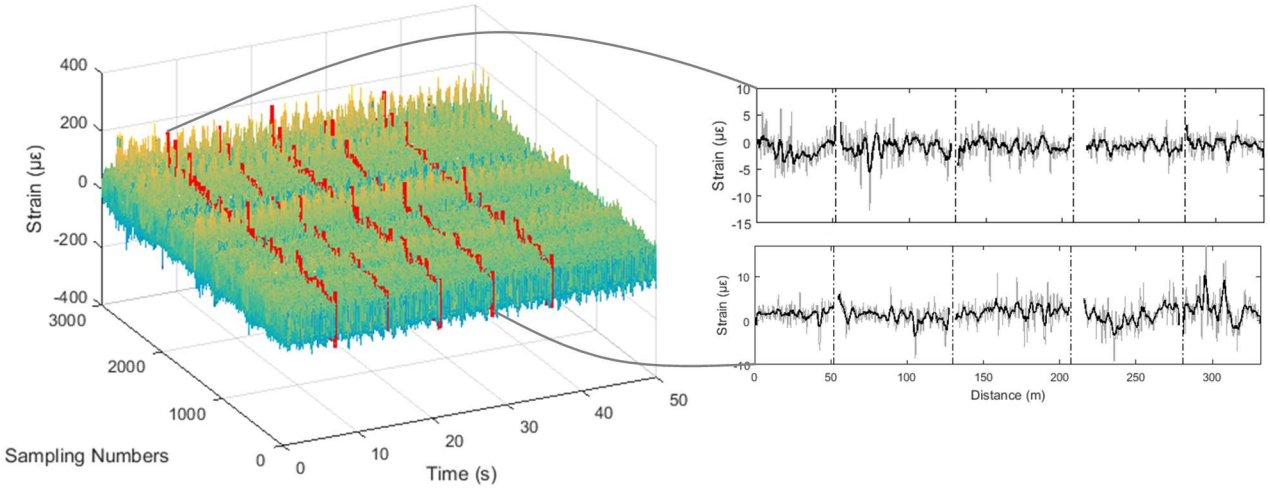

Figure 3.19 Strain sets while the trucks are located at the middle of each span

By following the proposed procedure using equation. 3.5 through 3.10, the crack index profile for this specific dynamic test is calculated. Figure. 3.20 shows the crack index values, $\hat{\beta}$.

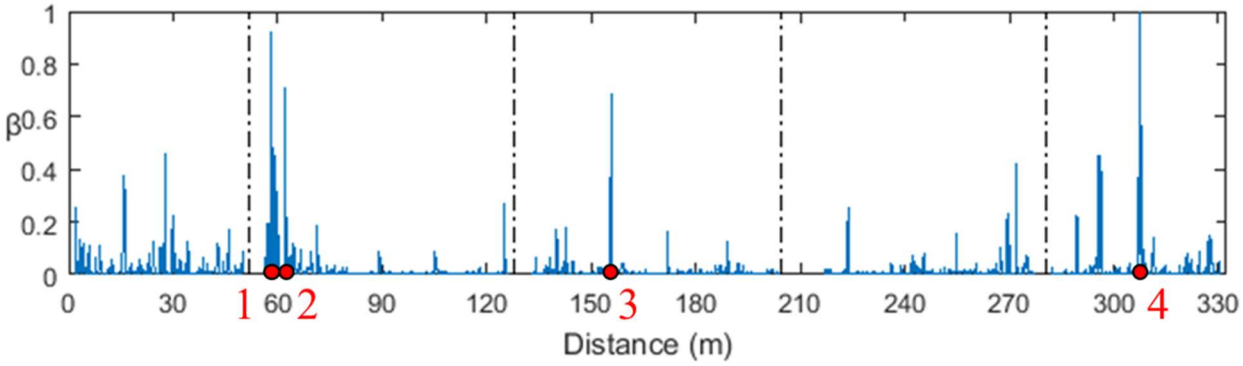

Figure 3.20 Crack index for all the sampling points along the bridge

As it is shown in Figure. 3.20, point 4 has the highest crack index and is located at 27.4 m from the beginning of the fifth span. The other three point having the highest damage index are located at 6.4 and 10.4 m from the beginning of the second span and 27.9 m from the beginning of the third span. Damage index values of the 1^{st}, 2^{nd}, 3^{rd} and 4^{th} point are 0.92, 0.70, 0.68 and 1 respectively.

After inspection of these 4 points at the bridge site, it was found that point 4 at the fifth span relates to a crack as it was anticipated. The other 3 points were detected to be related to the connection joints of the precast superstructure segments with elevation differences. Figure. 3.21 illustrates the crack found at the fifth span. The direction of the crack with its propagation pattern was enhanced with a marker.

Results show that the proposed method is able to detect probable crack locations under dynamic loads.

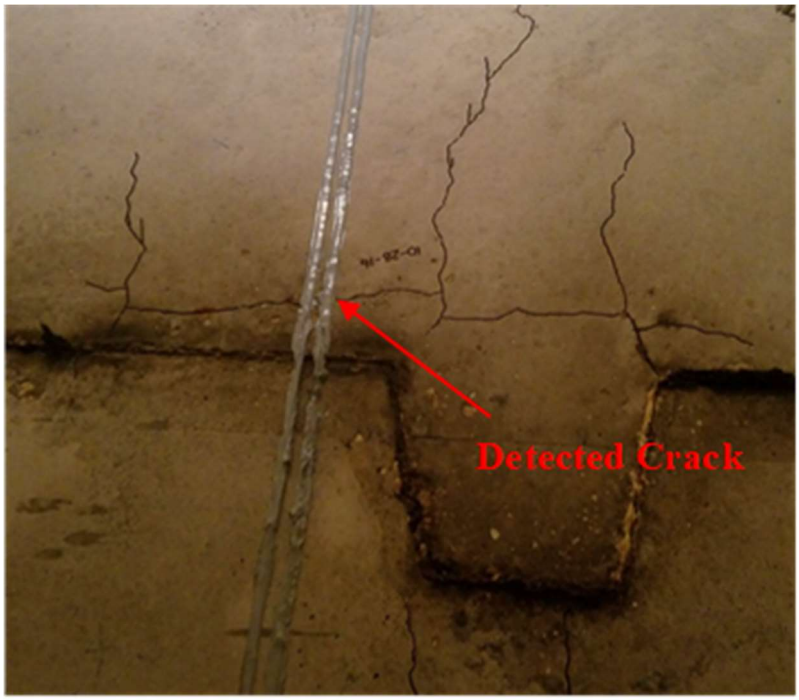

Figure 3.21 Detected crack in the fifth span (point 4)

3.4.2 Thornton Quarry bridge

3.4.2.1 Strain measurements

Distributed strain acquisition in time for the Thornton Quarry bridge was performed under unrestricted traffic. Smaller sampling interval and higher measurement frequency were used to keep up with the speed of traffic. The trade-off for having a high measurement frequency is the high level of noise on the data. Wavelet noise reduction technique was used on the initial time-distance strain profiles for all the 8 recording cases.

Figures 3.22 and 3.23 show the filtered strain profile of the deck and bottom flange of run number 5.

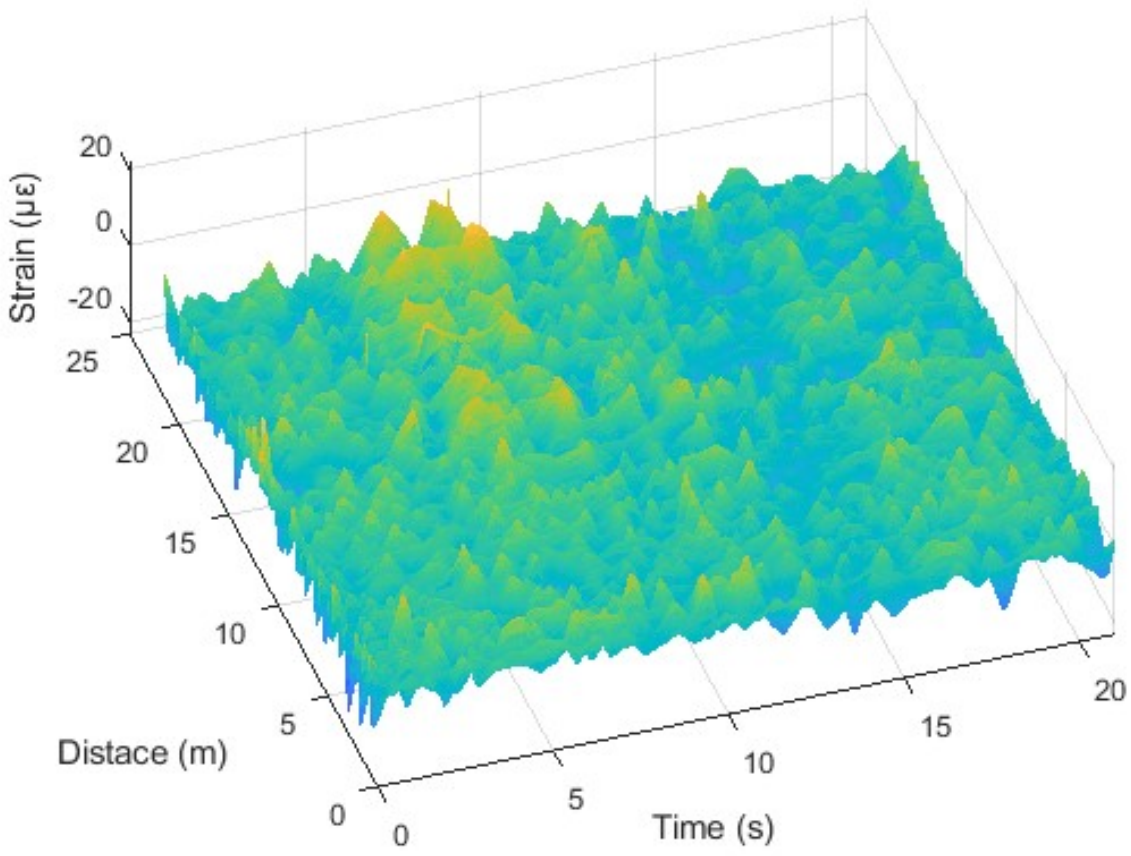

Figure 3.22 Filtered distributed strain profile of the deck for run number 5

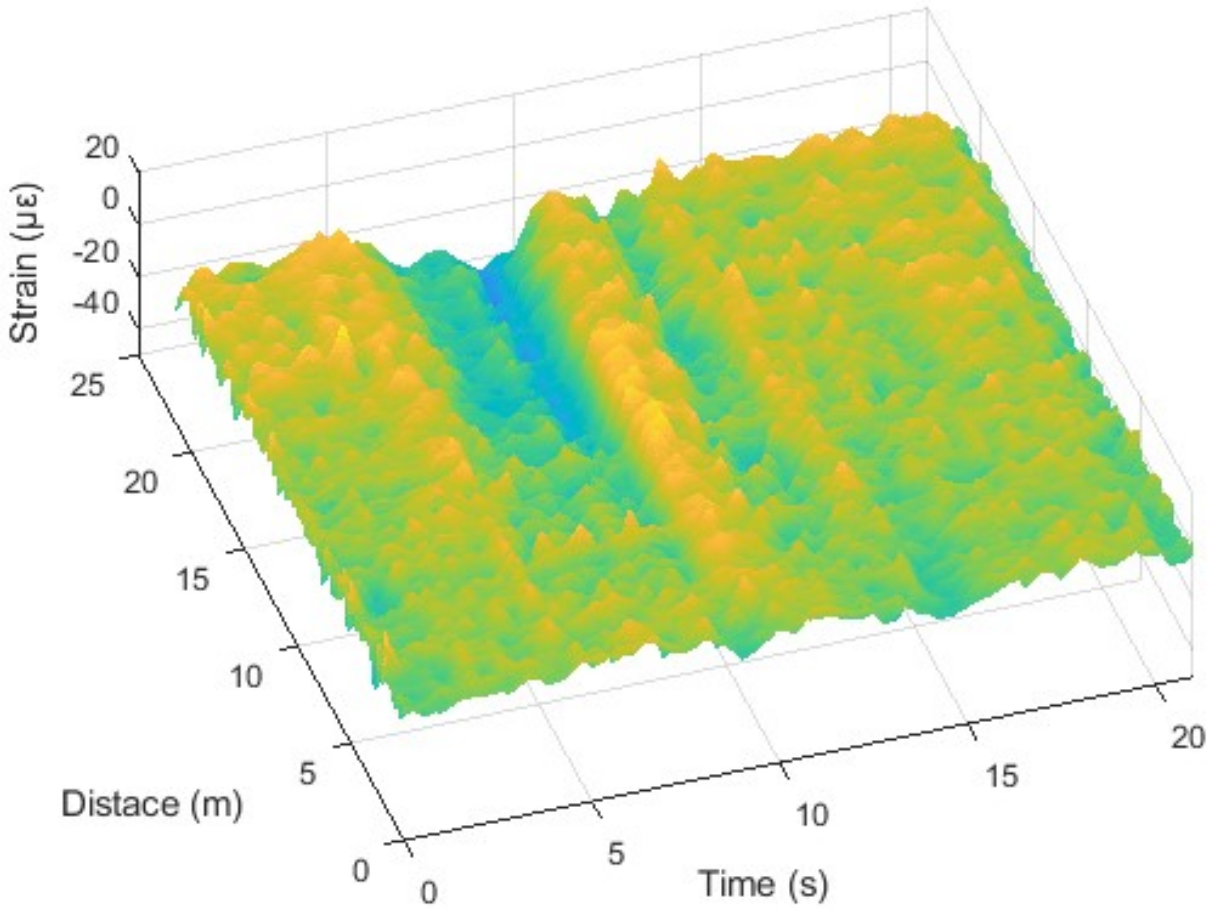

Figure 3.23 Filtered distributed strain profile of the bottom flange for run number 5

Since no information regarding the moving loads over the bridge was available, theoretical strains could not be generated in conventional manner. Therefore, flange strains were used as a reference, representing the uncracked strain profile.

For every sampling point along the deck there is an equivalent sampling point on the flange. In an ideal condition where no cracks are generated in the deck and the

structure is performing in its elastic range, strain at the deck of a section, ε_{deck}, is related to its corresponding strain at the flange, ε_{flange}, with the following equation:

$$\varepsilon_{deck} = -\gamma \varepsilon_{flange} \tag{3.11}$$

$$\gamma = \frac{y_{deck}}{y_{flange}} \tag{3.12}$$

The coefficient γ is solely related to shape of the section and where the neutral axis is located along the section. y_{deck} is the distance between neutral axis of the section to the bottom of the girder. y_{flange} is the distance between the neutral axis of the section to the upper side of the bottom flange. Figure. 3.24 shows strain diagram of a composite girder's cross-section.

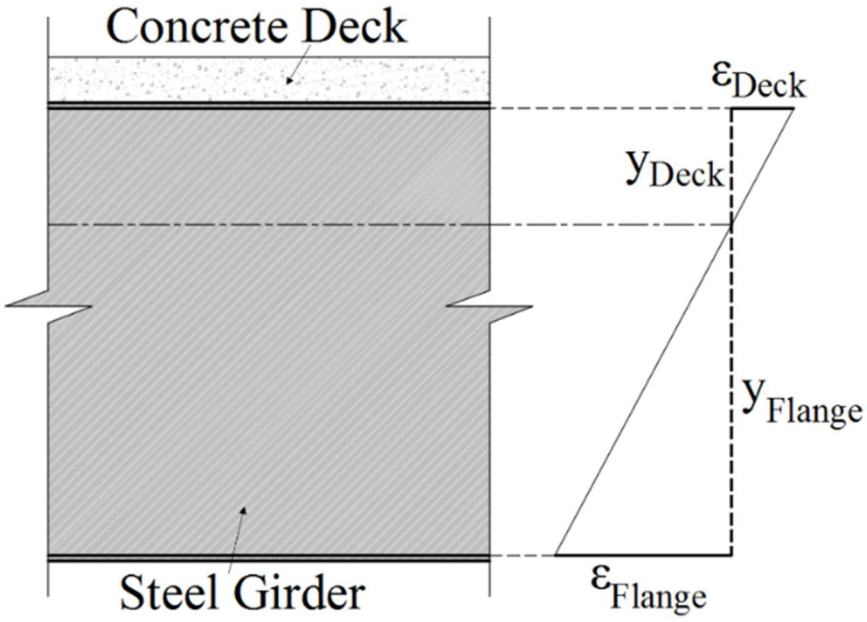

Figure 3.24 Strain diagram of the cross section

By multiplying γ coefficient, distributed strains of the flange are transformed to their corresponding deck strains for comparison:

$$[\varepsilon^M]^{ED} = -\gamma[\varepsilon^M]^F \tag{3.13}$$

Where $[\varepsilon^M]^{ED}$ is the equivalent deck strains generated from flange strains, $[\varepsilon^M]^F$. Recognition of abrupt changes of strains due to cracks or damages are performed by measuring the differences between the actual deck strains, $[\varepsilon^M]^D$ and the equivalent deck strains, $[\varepsilon^M]^{ED}$. Calculating the variances of strains differentials in time for every single sampling point along the fiber, is set to be an indication of crack or damage in that sampling point. The higher the variation of strain differential, the higher the probability of micro cracks at that section.

$$Var\left([\varepsilon^M]_{x_i}^D - [\varepsilon^M]_{x_i}^{ED}\right) = \left(\frac{1}{N}\sum_{j=1}^{N}\left((\varepsilon^M)_{x_i,t_j}^D - (\varepsilon^M)_{x_i,t_j}^{ED}\right)^2\right) - \mu_{x_i}^2 \quad (3.14)$$

$$\mu_{x_i} = \frac{1}{N}\sum_{j=1}^{N}\left((\varepsilon^M)_{x_i,t_j}^D - (\varepsilon^M)_{x_i,t_j}^{ED}\right) \quad (3.15)$$

Where $[\varepsilon^M]_{x_i}^D$ is a vector that contains measured deck strains for sampling point x_i in time, $[\varepsilon^M]_{x_i}^{ED}$ is a vector with equivalent measured deck strains for sampling point x_i in time, N is the number of instances of time or number of strain values through time, $(\varepsilon^M)_{x_i,t_j}^D$ is the measured deck strain at point x_i and instance of time t_i, $(\varepsilon^M)_{x_i,t_j}^{ED}$ is the equivalent measured deck strain at point x_i and instance of time t_i, μ_{x_i} is the average of measured stain differentials and Var stands for variance. Figures 3.25 to 3.32 depict the calculated variances in equation (3.14) for all the 8 runs over the bridge.

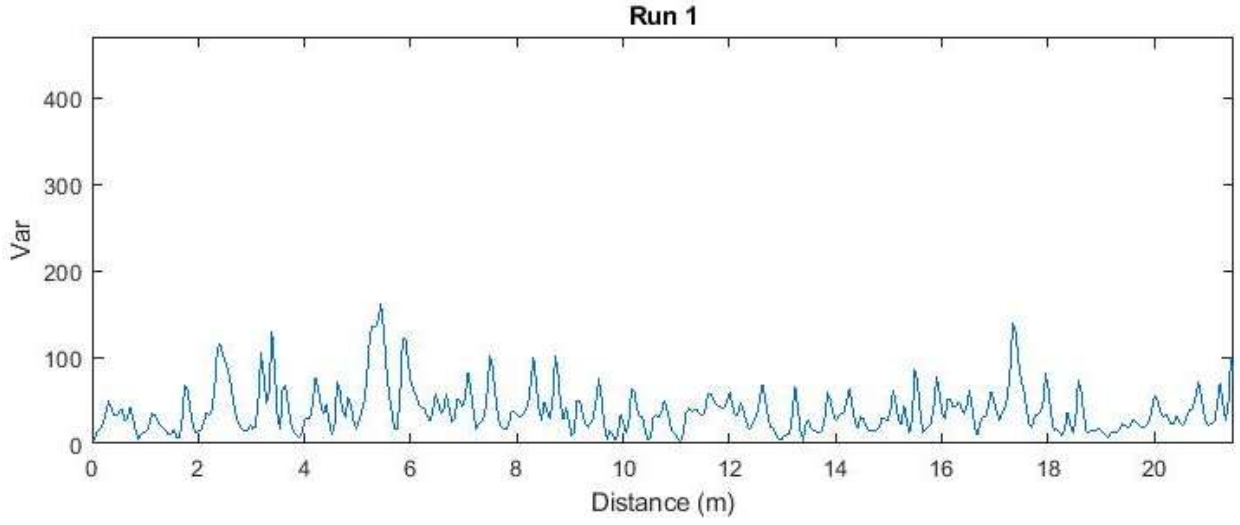

Figure 3.25 Variances of strains differentials through time along the deck for run 1

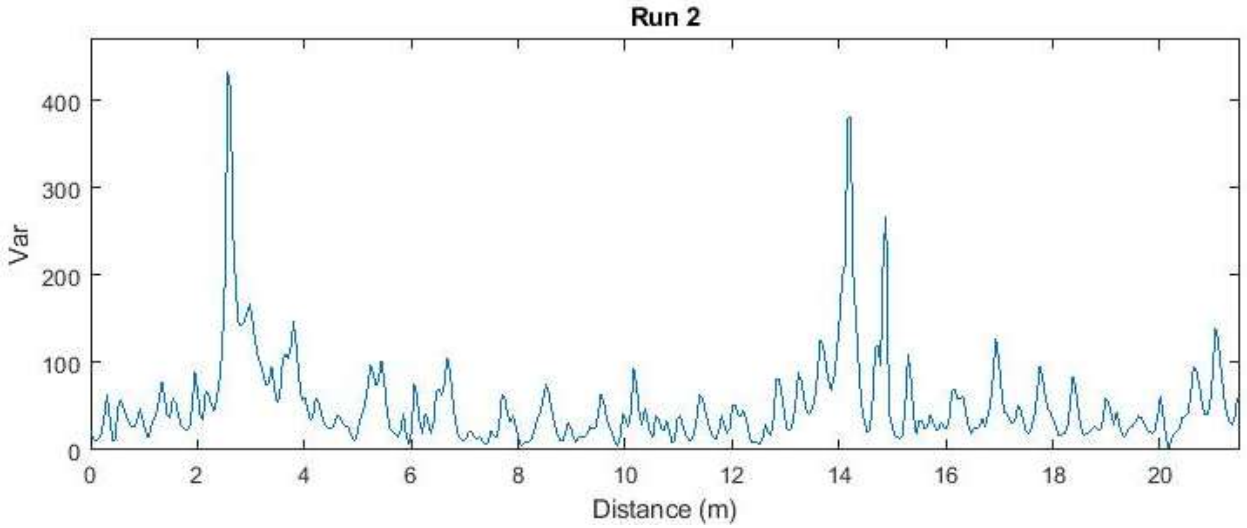

Figure 3.26 Variances of strains differentials through time along the deck for run 2

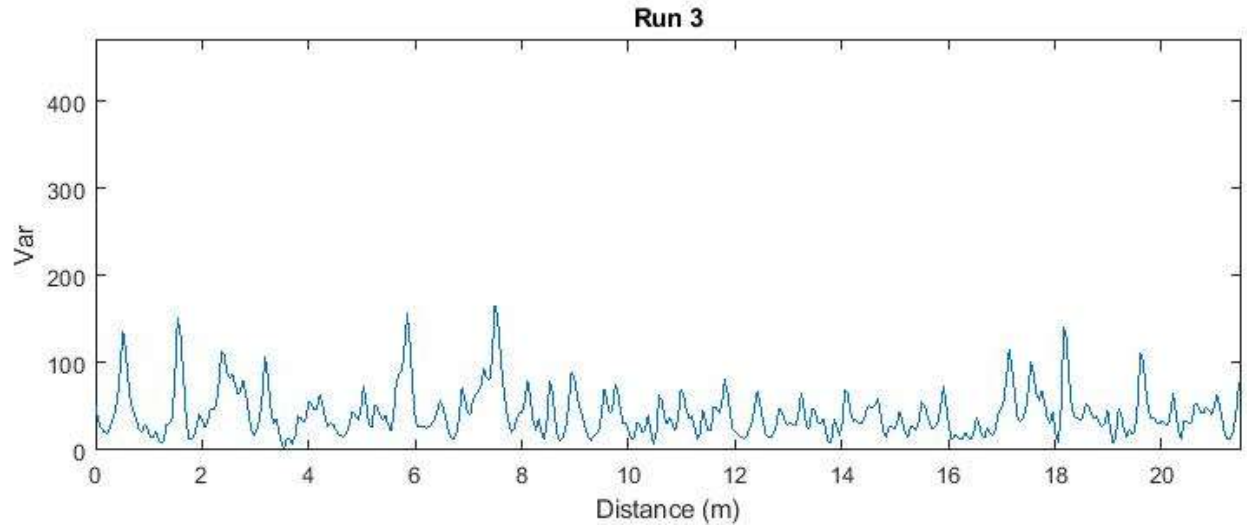

Figure 3.27 Variances of strains differentials through time along the deck for run 3

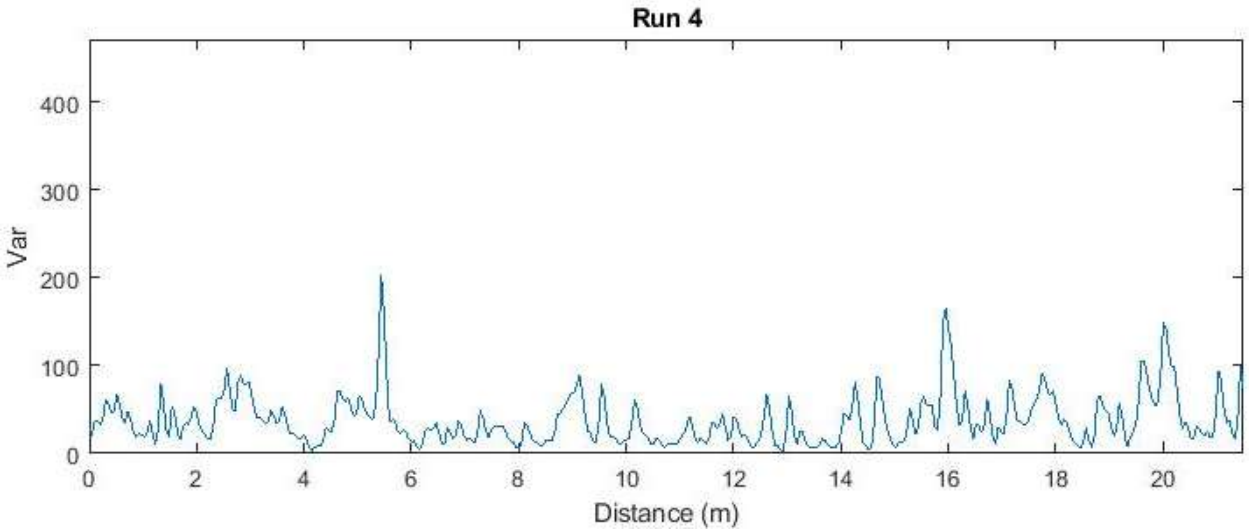

Figure 3.28 Variances of strains differentials through time along the deck for run 4

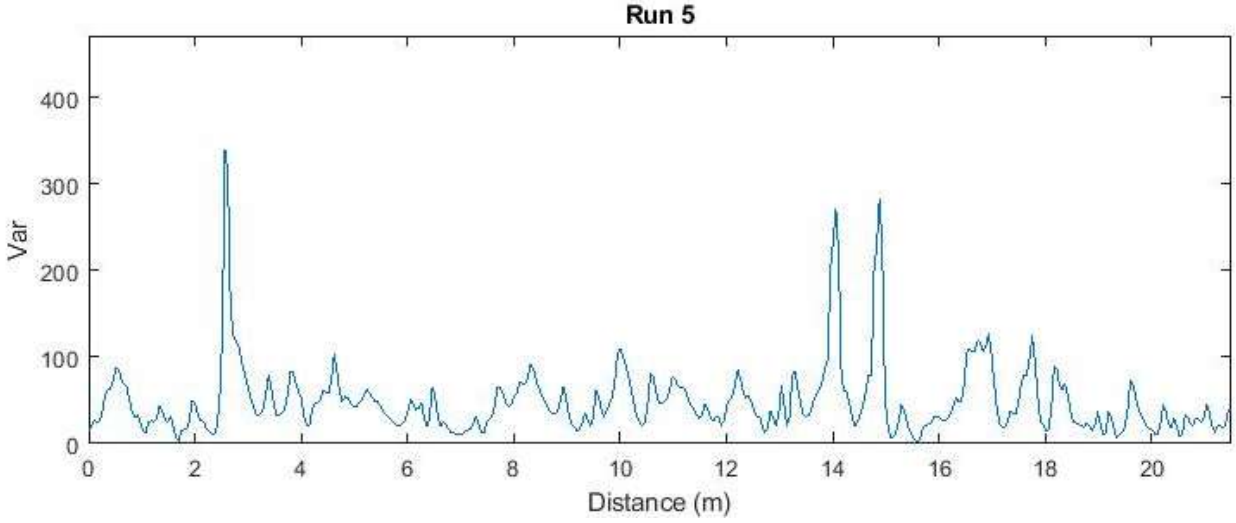

Figure 3.29 Variances of strains differentials through time along the deck for run 5

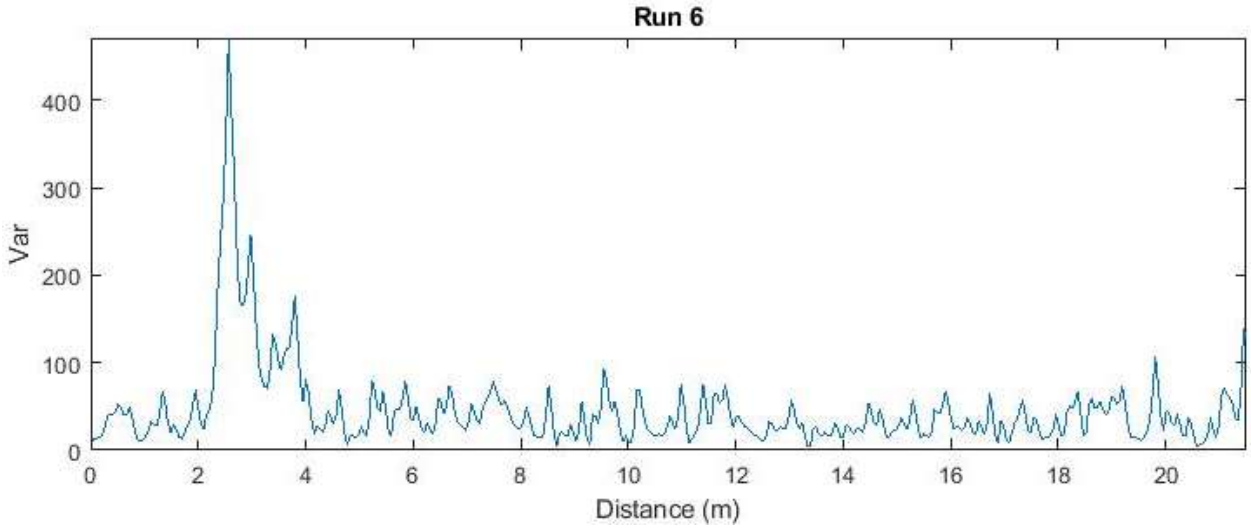

Figure 3.30 Variances of strains differentials through time along the deck for run 6

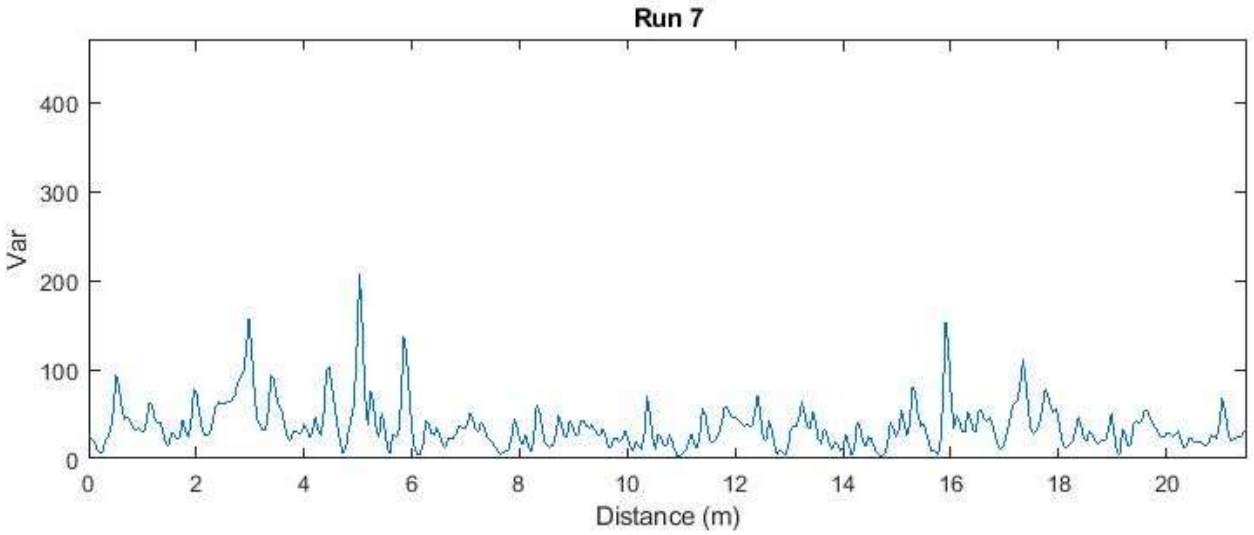

Figure 3.31 Variances of strains differentials through time along the deck for run 7

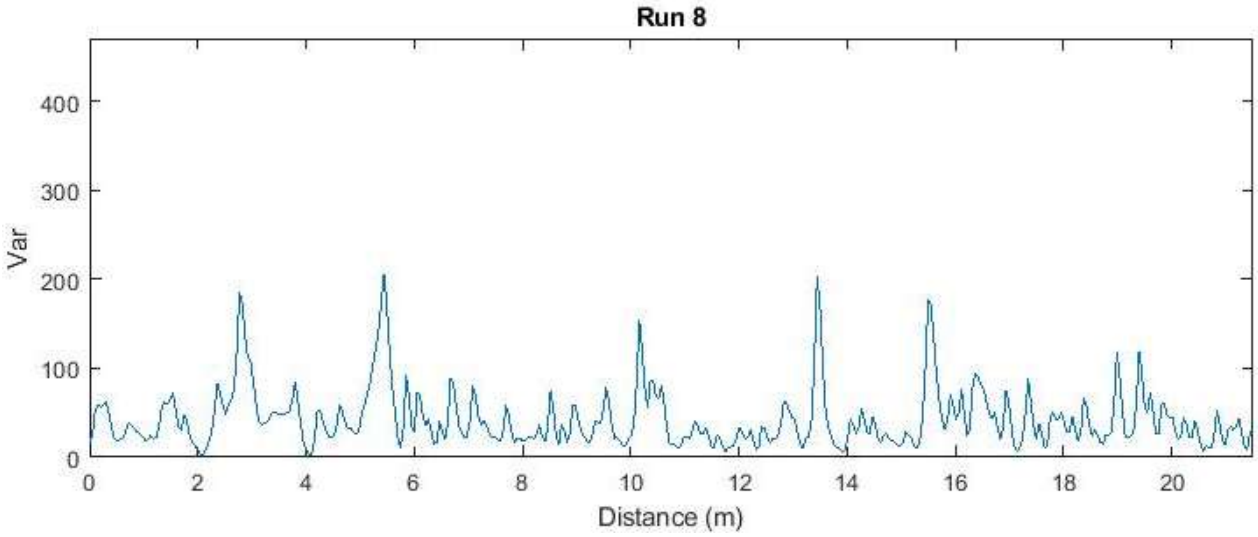

Figure 3.32 Variances of strains differentials through time along the deck for run 8

A quick review on the results of the variances of strain differentials for all the 8 runs showed that sampling points at distances 2.5, 14 and 14.9 m from the abutment of the bridge have the highest values compared to their adjacent sampling points which might have been an indication of micro crack at those points. Run 2, 5 and 6 contain the higher values for differential strain variances. Rest of the runs show relatively lower variances. The reason for this fact may be due to randomness of passing trucks over the desired lane. It is assumed that for measurements of runs 1,3,4,7 and 8 no truck has passed the bridge, or the passed trucked used other lanes to commute. Therefore, variances of strains differentials are lower at the mentioned points compared to runs 2, 5 and 6.

The bridge was inspected throughout the lane and it was found that 4 micro-cracks are located along the span. Cracks 1, 2 and 3 were already detected by the strain measurements at 2.5, 14 and 14.9 m respectfully from the abutment. However, crack 4

which was located 19.7 m away from the abutment was not detected during the 8 measurements. Figures 3.33 to 3.35 illustrates the detected and missed cracks along the span.

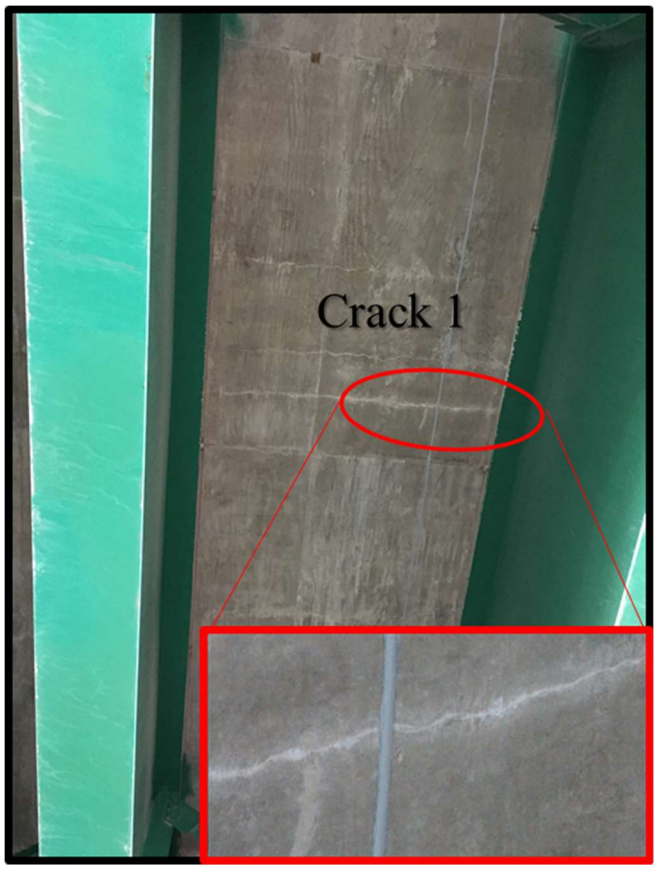

Figure 3.33 Detected micro-cracks on the surface of the deck

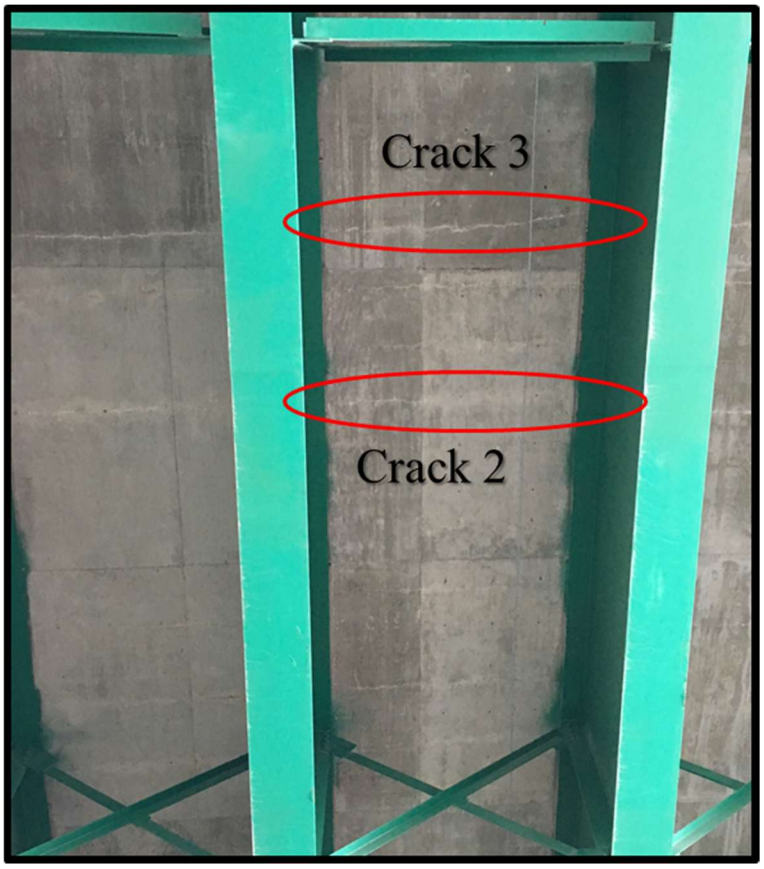

Figure 3.34 Detected micro-cracks on the surface of the deck

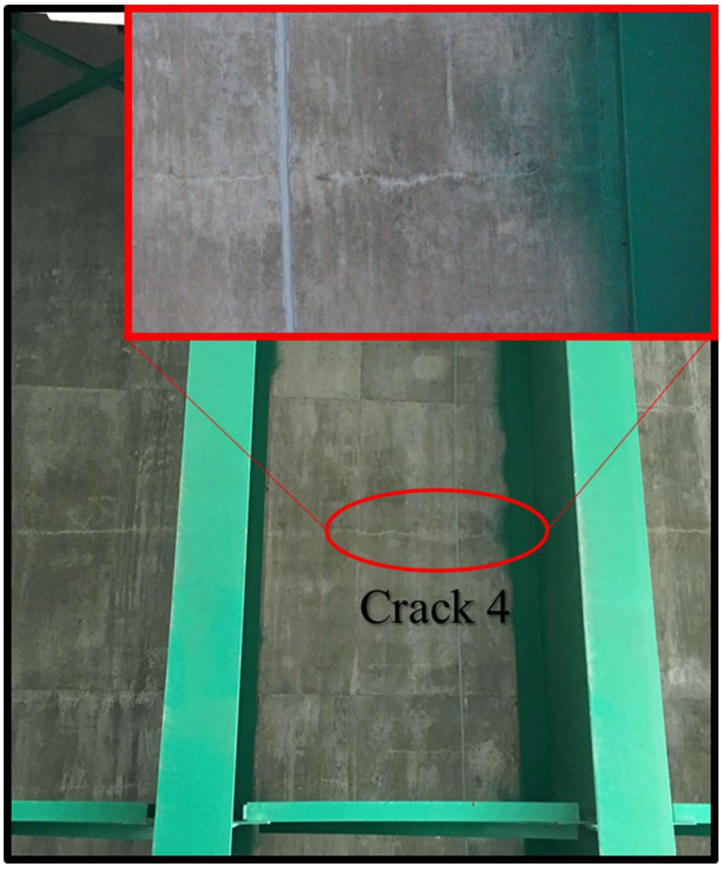

Figure 3.35 Detected micro-cracks on the surface of the deck

In situ inspection depicted that the proposed method works for micro crack detection through regular traffic. No pre measurement of strain along the length of the bridge is required for this method to work. Traffic stoppage and controlled traffic flow is not also required by this method. Although in should be noted that measurement pool should contain enough runs for reliable analysis of the data.

3.5. Summary of the chapter

A method for micro crack detection under dynamic loads using distributed fiber optic sensors was proposed in this chapter. The method utilizes Brillouin Optical Time

Domain Analysis technique to measure distributed strains along the structure. The developed procedure is not dependent on measurement of reference strains of the structure where no loads are applied on it. Traffic stoppage is also not required for proper performance of the method. Detection of micro-cracks with induced strains over the noise ratio is achieved by calculating the strain differentials in theory and measurement field. Formulation of the method leads to a normalized crack index along the sampling point on the entire length of the structure. For random traffic loads with no information on the loading, variances of the strain differentials over time is set to be the indicator of presence of cracks. The applicability of the method was verified by dynamic load testing on a five-span continuous precast post-tensioned concrete box girder bridge and a three-span continuous steel girder bridge. Analysis of the results led to probable location of damages. Visual inspections were performed on both bridges for verification purposes. Sampling points with highest crack index values in Kishwaukee bridge corresponded to a micro-crack and three sectional misalignments. Highest values of the strains differentials in Thornton Quarry bridge were verified to be three micro cracks. However, the method failed to detect one micro crack located on Thornton Quarry bridge. The proposed method depicted acceptable performance in detecting micro crack under dynamic loads. However, measurement pool should contain enough random traffic runs for a robust crack detection performance.

Chapter 4 . METHOD AND SENSOR FOR MONITORING WEIGHT OF TRUCKS IN MOTION BASED ON BRIDGE GIRDER END ROTATIONS

In the study described in this chapter, a new concept and sensor for monitoring of moving truck weights on Bridges is introduced. The method is based on the correlation between the bridge abutment rotations and the axle weights of moving trucks on the bridge. The proposed BWIM system uses the end rotation influence lines due to the truck axle loads. The rotational response of the bridge due to passing trucks at the abutment are measured by a rotation sensor, specifically developed for the proposed BWIM system.

The rotation sensor developed in this study is an inherent component of the proposed approach due to its attributes in terms of geometric conformity for applications in various bridge types, and space limitations at the bridge abutment and girder interfaces, temperature compensation, dynamic response, and cost effectiveness. The concept, and formulations leading to the method for the rotation based BWIM system is described first. The rotation sensor including the theoretical and calibration of the sensor are described separately. Field implementation of the proposed BWIM system at a bridge site, calibrations, and proof of concept monitoring of the truck weights are described last.

4.2 Methodology

The proposed approach is based on the relationship between the load and the load induced rotations in structures. In particular application to bridges, the change in the end rotations of bridge girders due to axle loads of trucks are employed for the formulation of BWIM relationships. In the simplest form, considering a simple span, the relationship

between the rotation of the abutment and the applied point load is demonstrated by Figure 4.1:

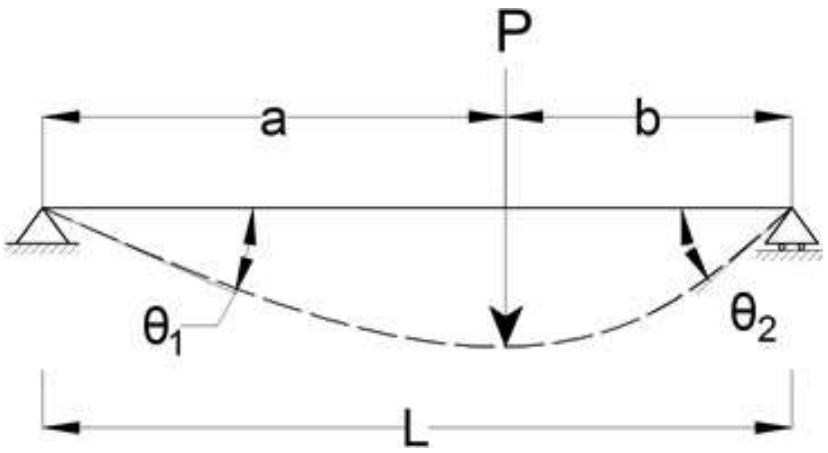

Figure 4.1 Deflection of a simple span beam due to a point load

$$\theta_1 = \frac{Pb(L^2-b^2)}{6LE} \tag{4.1}$$

Where, P is the point load at an arbitrary distance, b, from the abutment; L, is the span length, E is modulus of elasticity and I is the moment of inertia of the girder section. Substituting the point load, P, with a unit load and recording the rotation at the abutments due to a moving unit load generates the rotational influence line. The generalised influence line approach can be employed for any span type, including continuous spans. Considering linear behavior, the effect of vehicle axle loads on the rotational response of the abutment follows the superposition principle shown in figure 4.2.

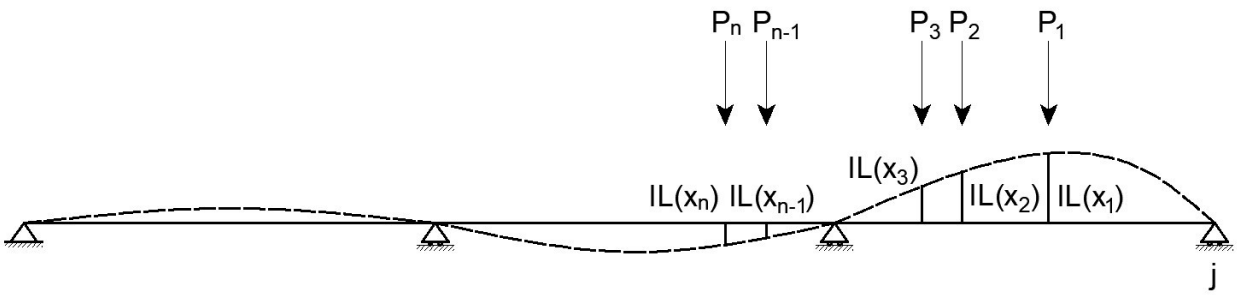

Figure 4.2 Rotational influence line of support at j

The superposition principle relates the effect of multiple axle loads on the rotational response of the abutment by using the rotational influence line at the support:

$$\theta_j = \sum_{i=1}^{n} P_i \,.\, IL(x_i) \tag{4.2}$$

Where, θ_j is the rotation at the abutment, P_i is the truck axle loads, n is the number of axles, $IL(x)$ is the rotational influence line of the abutment, and x_i is distance of the axle i from the abutment. The gross vehicle weight is the summation of all the axle weights as follows:

$$GVW = \sum_{i=1}^{n} P_i \tag{4.3}$$

4.2.1. Axle Spacing, Individual Axle Weights and GVW Calculation

The proposed BWIM system requires two strain-based sensors (wheel sensors) for detection of axles, their spacings, and speeds; and a rotation sensor for the computation of the axle weights. Figure 4.3 shows the general locations of the wheel

sensors (A and B), rotation sensor (C) and truck location on the bridge. P_1, P_2, …, P_n are the individual truck axle weights and L_1, L_2, …, L_{n-1} are axle spacing for a truck with n axles. w_1 is the distance between wheel sensor A and the abutment and w_2 is the distance between wheel sensor B and wheel sensor A. The Rotation sensor is located at the abutment support. As seen in figure 4.3, the truck is moving from left to right toward point C where the rotation sensor is installed.

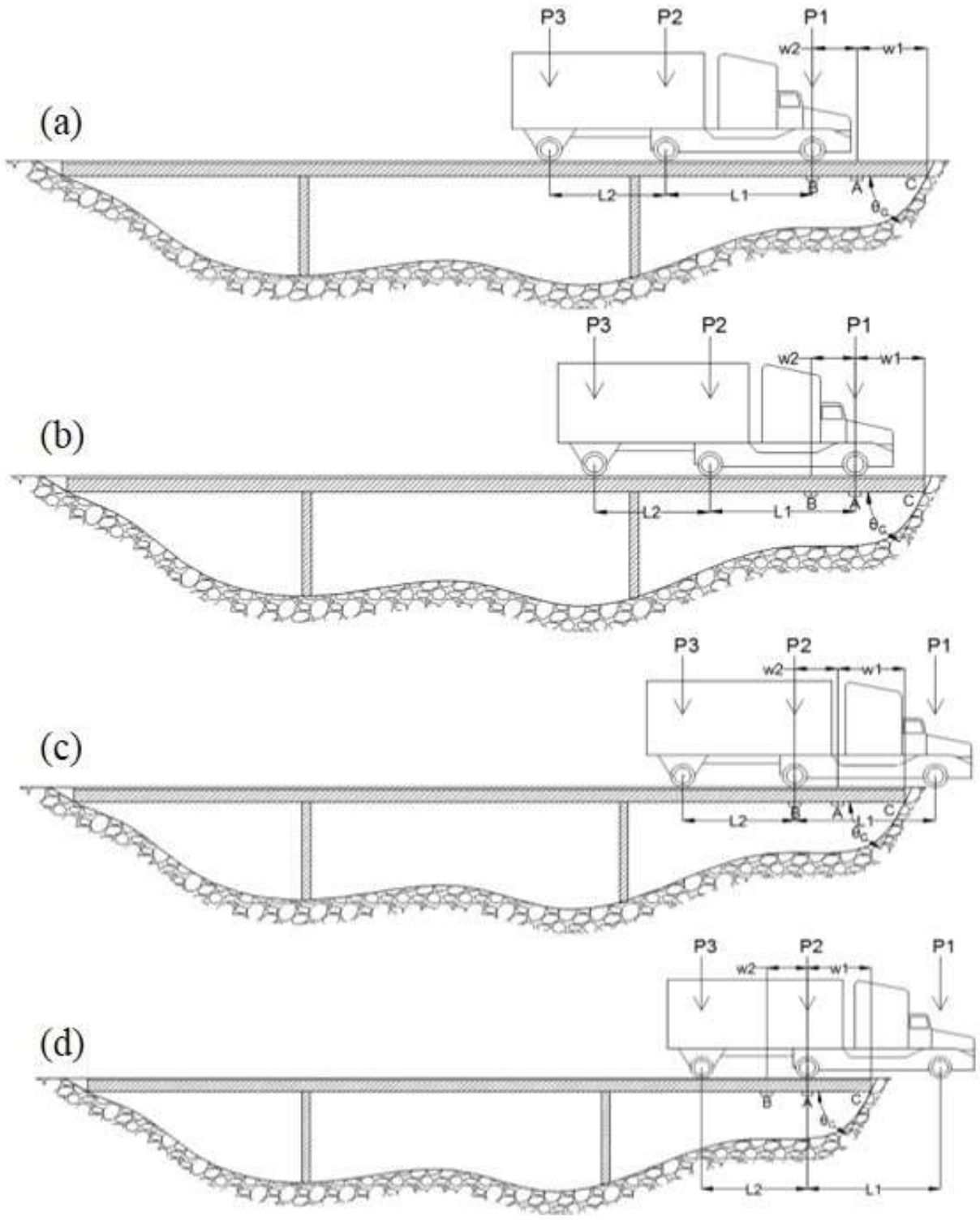

Figure 4.3 Bridge weigh in motion calculation steps

The general equation in the system of equations, relating the truck axle loads to the abutment rotation is shown in Equation 4.4. The rotation at point C (θ_C), when the first axle of the truck is at a general distance x from the abutment is calculated as follows:

$$\theta_C = P_1 * IL(x) + P_2 * IL(x + L_1) + \cdots + P_n * IL(x + L_1 + \cdots + L_{n-1}) \quad (4.4)$$

Where $IL(x)$ is the magnitude of the rotational influence line of point C when the truck axle load is located at point x. The first axle of the truck reaches wheel sensor B first as shown in figure 3a. These two wheel sensors are solely used to detect the axle spacing and truck speed. The process of calculating the truck speed and measuring individual axle spaces starts at this moment. The instance when the first axle reaches wheel sensor B is defined as T_{B1}.

Figure 4.3b shows the moment when the first axle reaches wheel sensor A. The time corresponding to this moment is defined as T_{A1}. The rotation at the abutment when the first axle reaches wheel sensor A, θ_C^{A1} , is calculated as:

$$\theta_C^{A1} = P_1 * IL(w_1) + P_2 * IL(w_1 + L_1) + \cdots + P_n * IL(w_1 + L_1 + \cdots + L_{n-1}) \quad (4.5)$$

The time difference when the first axle travels between wheel sensors A and B is calculated with the following equation:

$$\Delta T_1 = T_{A1} - T_{B1} \quad (4.6)$$

Since the distance between the two wheel sensors is known and the travel time between these two sensors are recorded, the speed of the truck, v, is then calculated as follows:

$$v = \frac{w_2}{\Delta T_1} \tag{4.7}$$

The time when the second axle reaches wheel sensors B and A are defined as T_{B2} and T_{A2} respectively.

The next step is when the second axle reaches the wheel sensor A. This is depicted in figure 4.3d. At this step the first axle should have left the bridge. Therefore, in writing the response equation, one unknown variable, P_1, is removed. To satisfy this condition, the distance between the wheel sensor A and the abutment should be less than the minimum axle spacing of the truck. The rotation at the abutment when the second axle reaches wheel sensor A is:

$$\theta_C^{A2} = P_2 * IL(w_1) + \cdots + P_n * IL(w_1 + L_2 + \cdots + L_{n-1}) \tag{4.8}$$

To calculate the individual axle spacing, two axles should pass over a single wheel sensor. Wheel sensors A and B can both be used to measure axle spacings independently. The spacing between the first and the second axle is estimated by the following equations:

$$L_1 = v(T_{B2} - T_{B1}) \quad \text{or} \quad L_1 = v(T_{A2} - T_{A1}) \tag{4.9}$$

The calculation repeats as the last axle reaches wheel sensor A.

$$\theta_C^{A(n-1)} = P_{n-1} * IL(w_1) + P_n * IL(w_1 + L_2 + \cdots + L_{n-1}) \tag{4.10}$$

$$L_{n-1} = v(T_{Bn} - T_{B(n-1)}) \quad \text{or} \quad L_{n-1} = v(T_{An} - T_{A(n-1)}) \tag{4.11}$$

$$\theta_C^{An} = P_n * IL(w_1) \tag{4.12}$$

In equation 4.12, the rotation at point C is measured by the rotation sensor and therefore, it is a known quantity. Considering that the abscissa of the influence line at w_1 is also a known quantity, the only unknown variable is the weight of the last axle, P_n. It is then computed by using equation 4.12. Substituting the calculated value of P_n into equation 10 leads to solving the weight of the preceding axle, $P_{(n-1)}$. This process is repeatedly performed in reverse order, starting from equation 4.12 through to equation 5 until all individual axle weights are calculated.

4.2.2. Monitoring of Rotations Using the Rotation Sensor

Determination of rotations employed in equation 4.12 is accomplished by the measurement of beam rotation at the bridge abutment. This parameter is measured using the fabricated rotation sensor. This optical fiber sensor consists of an arch with a radius of 50 mm, thickness of 0.65 mm and width of 14 mm. The arch material is spring steel and its modulus of elasticity is 200 GPa. Figure 4.4 shows a typical rotation sensor made in the laboratory. The sensing capability of this sensor comes from installing two fiber brag grating (FBG) sensors at the arch crown. Figure 4.5 shows the location of FBGs on the fabricated sensor.

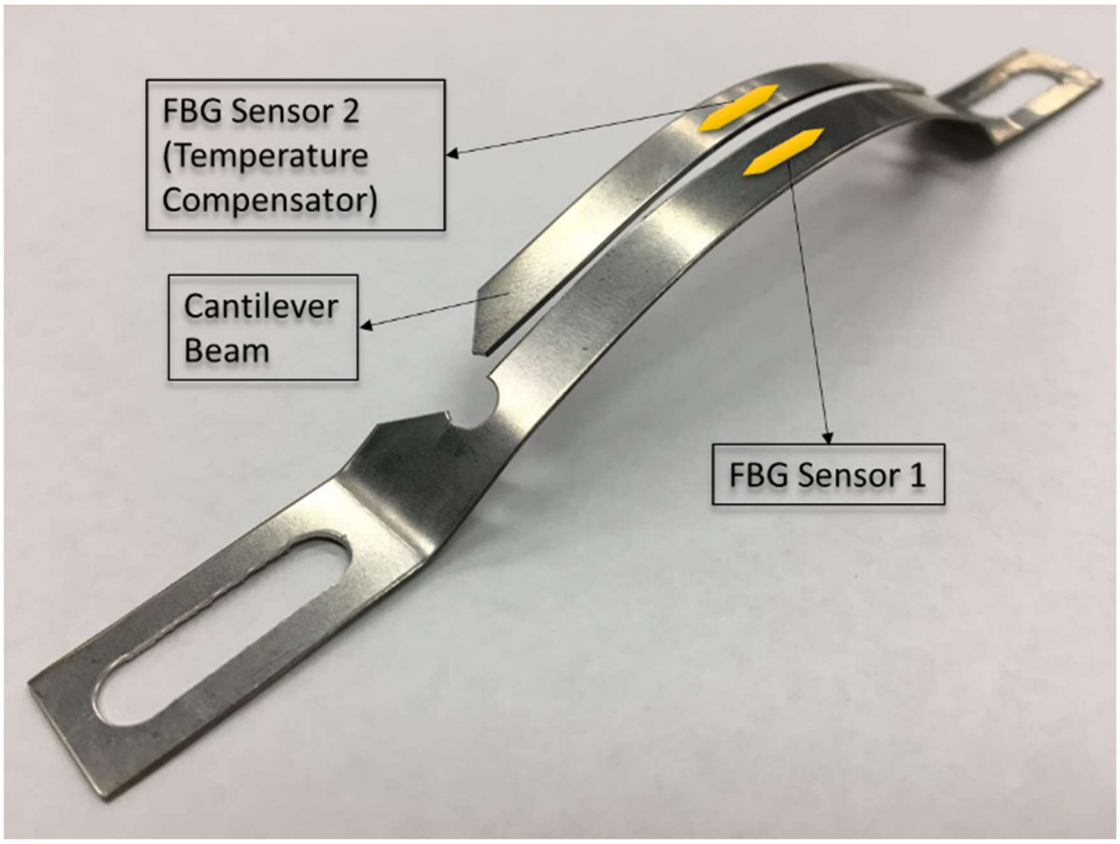

Figure 4.4 Rotation Sensor and FBG locations

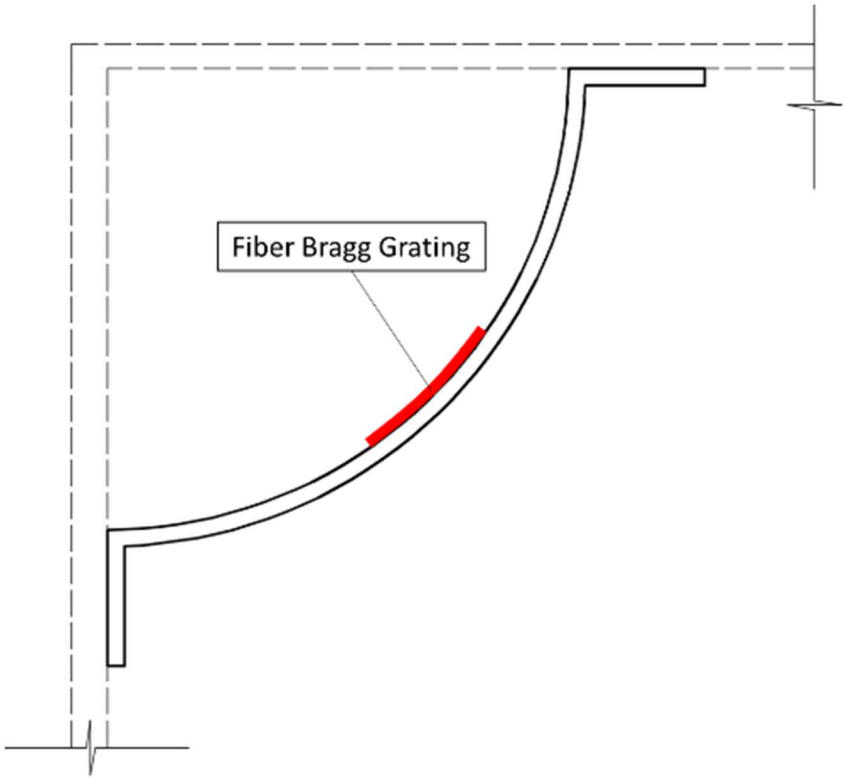

Figure 4.5 Rotation Sensor Layout

There are a couple of steps required to calculate the changes of rotation by the proposed rotation sensor. The attached FBG measures the changes of strain in the center of the rotation sensor. Therefore, the objective is to relate the end displacements and rotations to the strain in the center section. Thus, the first step is to find the relationship between the rotation sensor's end displacement and rotations to their corresponding shear forces and bending moments. For general curved members, Parcel and Moorman (1955) developed the stiffness matrix based on the slope-deflection method. Figure 4.6 depicts a curved member undergoing rotations and displacements x_i , x_j , y_i , y_j , θ_i and θ_j at both end points.

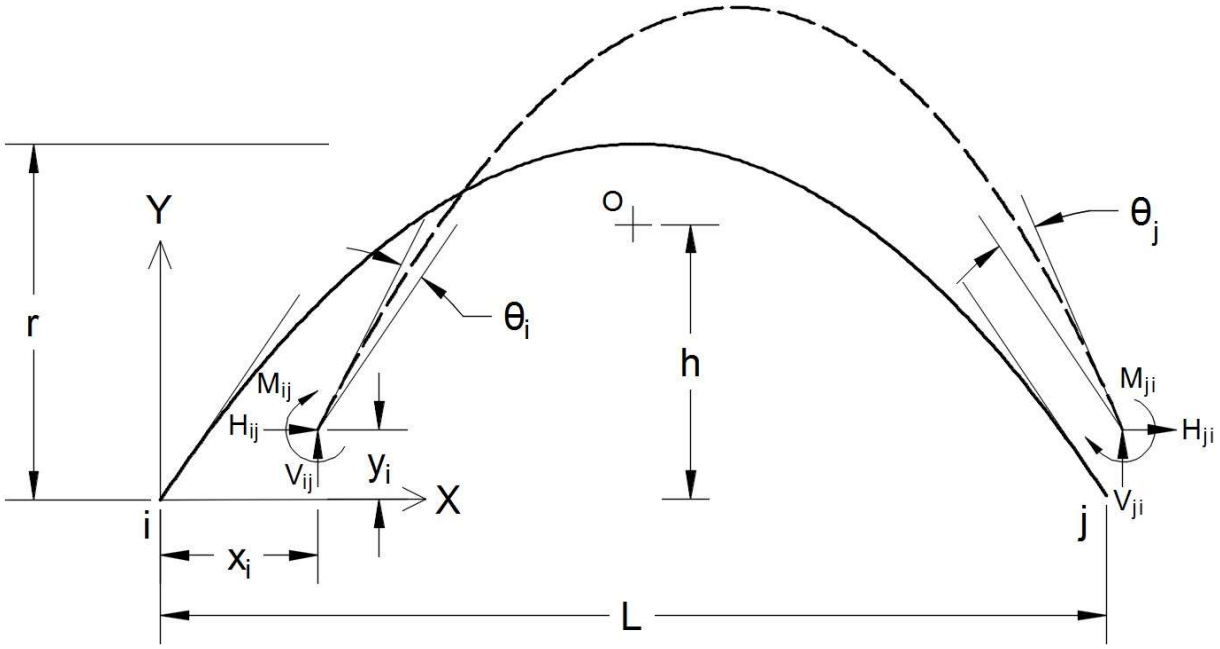

Figure 4.6 Curved member with positive moments and forces

The following matrix form is the force-displacement relationship of the end points:

$$\begin{Bmatrix} M_{ij} \\ M_{ji} \\ V_{ij} \\ V_{ji} \\ H_{ij} \\ H_{ji} \end{Bmatrix} = \frac{EI}{L} \begin{bmatrix} C_1 & -C_2 & \frac{-C_3}{L} & \frac{C_3}{L} & \frac{C_4}{r} & \frac{-C_4}{r} \\ & C_1 & \frac{-C_3}{L} & \frac{C_3}{L} & \frac{-C_4}{r} & \frac{C_4}{r} \\ & & \frac{2C_3}{L^2} & \frac{-2C_3}{L^2} & 0 & 0 \\ & & & \frac{2C_3}{L^2} & 0 & 0 \\ & symmetric & & & \frac{C_4}{rh} & \frac{-C_4}{rh} \\ & & & & & \frac{C_4}{rh} \end{bmatrix} \begin{Bmatrix} \theta_i \\ \theta_j \\ y_i \\ y_j \\ x_i \\ x_j \end{Bmatrix} = [S] \begin{Bmatrix} \theta_i \\ \theta_j \\ y_i \\ y_j \\ x_i \\ x_j \end{Bmatrix} \quad (4.13)$$

Where $[S]$ = stiffness matrix of the member, E = modulus of elasticity, I = cross sectional moment of inertia, L = span length of the curved member, h = perpendicular distance from the centroid to the line connecting the two joints, r = member's height, V = vertical shear force, H = horizontal shear force and M = bending moment. The stiffness parameters C_1, C_2, C_3, C_4 and C_5 are defined as:

$$C_1 = \frac{L}{\int ds_0} + \frac{L^3}{4\int x_0^2 ds_0} + \frac{h^2 L}{\int y_0^2 ds_0} \tag{4.14}$$

$$C_2 = \frac{L}{\int ds_0} - \frac{L^3}{4\int x_0^2 ds_0} + \frac{h^2 L}{\int y_0^2 ds_0} \tag{4.15}$$

$$C_3 = \frac{L^3}{2\int x_0^2 ds_0} \tag{4.16}$$

$$C_4 = \frac{rhL}{\int y_0^2 ds_0} \tag{4.17}$$

$$C_5 = \frac{h}{L} \tag{4.18}$$

The fabricated rotation sensor's shape is part of a cycloid. Wang and Merrill (1988) calculated the stiffness parameters for various curved shaped members including cycloidal curved members. The following equations are the stiffness parameters for a cycloidal curve member. Knowing the stiffness parameters of the designed rotation sensor, the displacements and rotations at both ends of the sensor can be related to the two ends moment and shear forces.

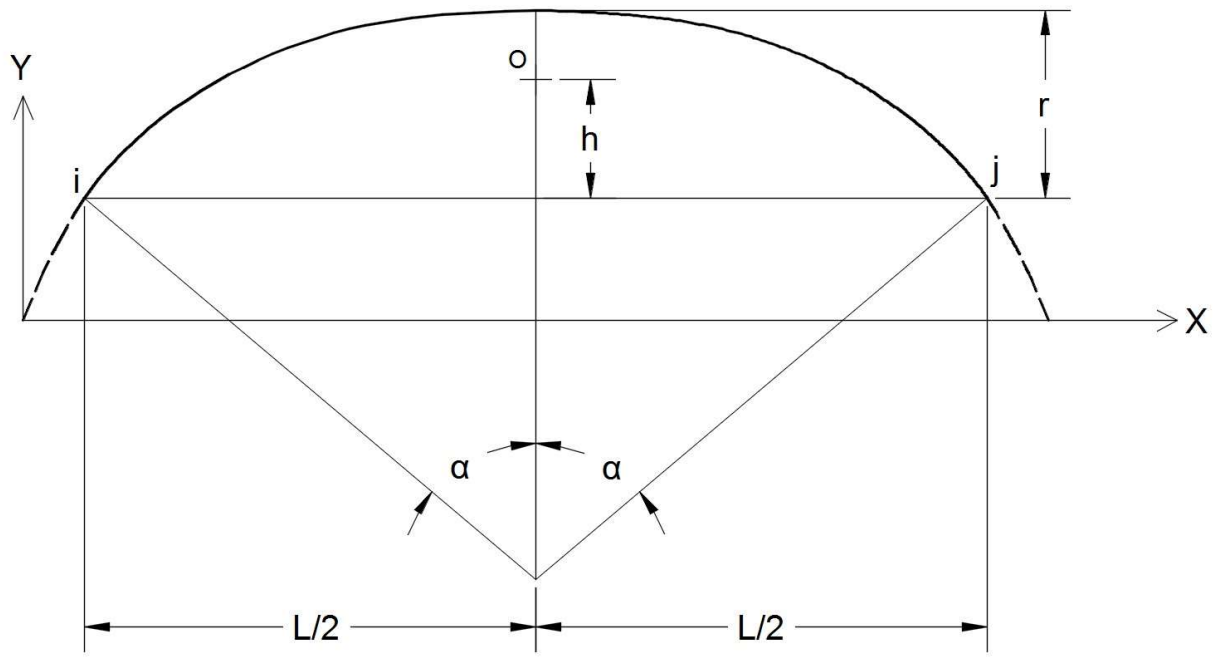

Figure 4.7 Cycloidal arch form

$$C_1 = \frac{\sin\alpha}{4\lambda} + \frac{2\,sin^6\alpha}{A\lambda^3} + \frac{32\,sin^6\alpha}{9B} \tag{4.19}$$

$$C_2 = \frac{\sin\alpha}{4\lambda} - \frac{2\,sin^6\alpha}{A\lambda^3} + \frac{32\,sin^6\alpha}{9B\lambda} \tag{4.20}$$

$$C_3 = \frac{4\,sin^6\alpha}{A\lambda^3} \tag{4.21}$$

$$C_4 = \frac{16\,sin^6\alpha}{3B\lambda} \tag{4.22}$$

$$C_5 = \frac{2\lambda}{3} \tag{4.23}$$

Where,

$$\lambda = \frac{r}{L} = \frac{sin^2\alpha}{2\alpha + \sin 2\alpha} \tag{4.24}$$

$$A = 2\sin\alpha\,(16\alpha^2 - 22) + 48\alpha\cos\alpha + \frac{10}{9}\sin 3\alpha - \frac{16}{3}\alpha\cos 3\alpha - \frac{2}{5}\sin 5\alpha \tag{4.25}$$

$$B = \frac{8}{45}(10\sin\alpha - 5\sin 3\alpha + \sin 5\alpha) \tag{4.26}$$

4.2.2.1. Relating the end moments and forces to the center section strain

To this point, shear forces and moments at both ends of the curved rotation sensor are calculated by knowing the stiffness parameters. The bending moment at the location of the FBG within the sensor assembly needs to be computed. Knowing the bending moments at this section leads to the derivation of the relative strain at the location of the FBG. Calculation of the bending moment at the center of the rotation sensor is achieved by applying a virtual cut at the desired point and forming the equations of equilibrium for that section.

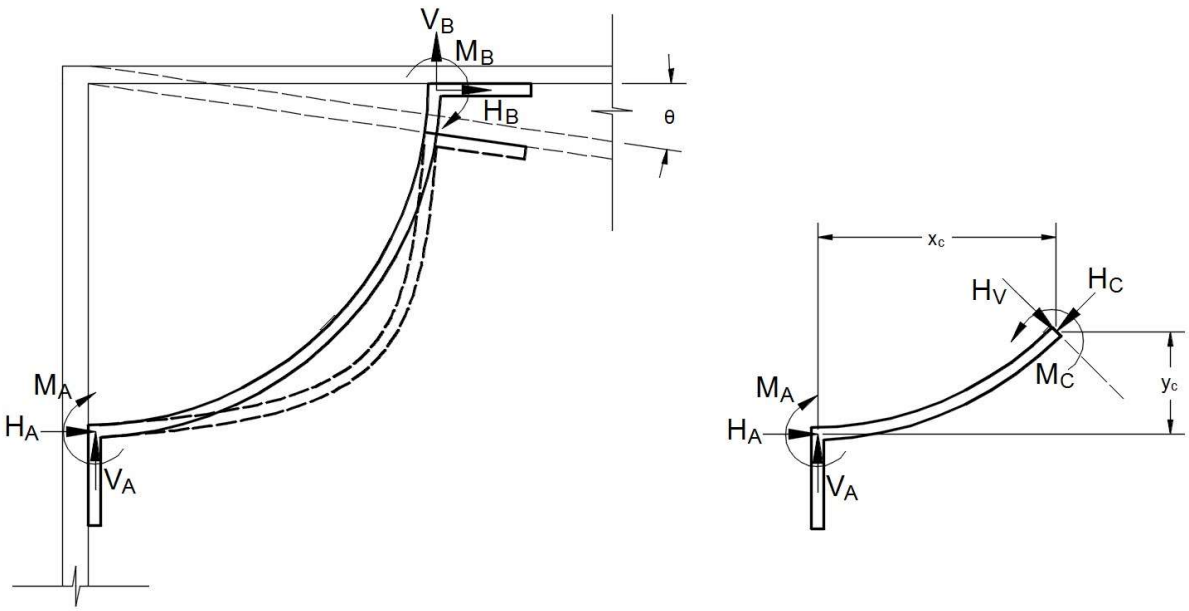

Figure 4.8 Rotation sensor displacements and free half-body diagram

Figure 4.8a illustrates the rotation sensor undergoing a displacement and rotation at point B due to the change of the rotation at a corner. Figure 4.8b shows the free body diagram of the section that is cut in the center. x_c and y_c are the horizontal and vertical distances from point C to point A. The bending moment at point C is calculated as follows:

$$M_c = V_A.x_c - H_A.y_c + M_A \qquad (4.27)$$

By knowing the section dimensions at point C, the stress distribution at that section can be expressed by the following equation:

$$\sigma_c = \frac{M_c.y}{I} \qquad (4.28)$$

Where y is the vertical distance of any arbitrary point from the neutral axis of the section and I is the moment of inertia of the section. Finally, the strain at the location of the FBG sensor, ε_c^f, is calculated as follows:

$$\varepsilon_c^f = \frac{\sigma_c}{E} \tag{4.29}$$

Where E is the modulus of the elasticity. The superscript f pertain to the strains resulting from external forces.

4.2.2.2. Temperature compensation of the rotation sensor

Since bridge weigh-in-motion monitoring requires continuous data to be recorded during different seasons with temperature fluctuations, the effect of temperature in the readings should be considered. To compensate for the effect of temperature, a cantilevered arch beam is used as part of the rotation sensor (see figure 4.4). The material and sectional properties of the temperature compensation beam is the same as the material properties of the main arch sensor. The FBG installed on the cantilevered portion of is designated as FBG sensor 2.

The calculated strain, ε_c^f, at the center of the rotation sensor is only due to the displacements and rotations at both ends. However, an additional strain, ε_C^T, resulting from the changes of temperature would effect the acquired strain in the sensor.

$$(\varepsilon_C)_1 = \left(\varepsilon_C^f\right)_1 + (\varepsilon_C^T)_1 \tag{4.30}$$

Where$(\varepsilon_C)_1$ is the total strain developed in the center of the rotation sensor where FBG sensor 1 is installed and $(\varepsilon_C^T)_1$ is the strain due to temperature developed in FBG sensor 1.

Since one end of the cantilever beam is free, no stress resulting from the end displacement and rotations will be transferred to this beam.

$$(\varepsilon_C^T)_1 = (\varepsilon_C^T)_2 \tag{4.31}$$

Therefore, by installing an FBG on this beam, pure changes of strain due to temperature is read by the second sensor. Since the temperature strains are the same in the cantilever beam and the fixed-end beam (see Equation 4.31), temperature compensation is achieved by subtracting ε_C^T measured by the cantilever beam sensor from total strains measured by the main arch sensor:

$$\left(\varepsilon_C^f\right)_1 = (\varepsilon_C)_1 - (\varepsilon_C^T)_2 \tag{4.32}$$

4.3. Calibration of the rotation sensor

The fabricated rotation sensors were also calibrated in the lab for repeatability and sensitivity analysis. Figure 4.9 depicts the calibration setup. Sensors were installed at one end of the beam by attaching one end to the lower flange of the beam and one end to the support. Changes in rotation at the location of the installed rotation sensors were determined by changing the height of the support at the opposite end of the beam by a scissor jack. This process was repeated for three cycles in order to determine if the sensor is free of hysteresis.

The vertical displacement of the end of the beam was recorded in each step by a precision dial gauge. The change in rotation at the sensor location was computed based on the length of the beam and the measured vertical displacements of the opposing end. Figure 4.10 shows the calibration results which correlates the change in rotation with changes of wavelength of the sensor. As it is shown, the sensor illustrates linear behavior with high repeatability, with a coefficient of correlation over 0.99.

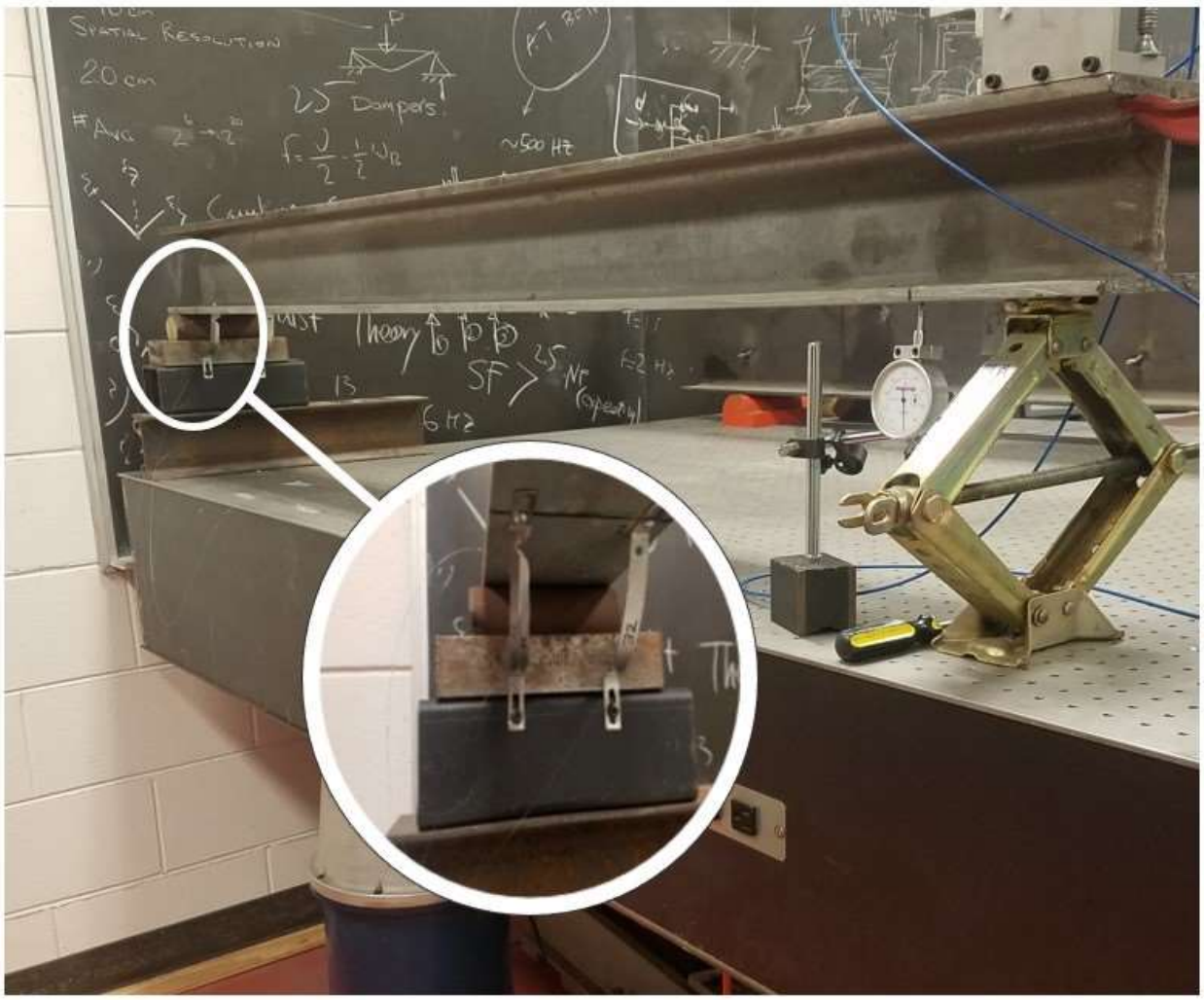

Figure 4.9 Rotation sensor calibration setup

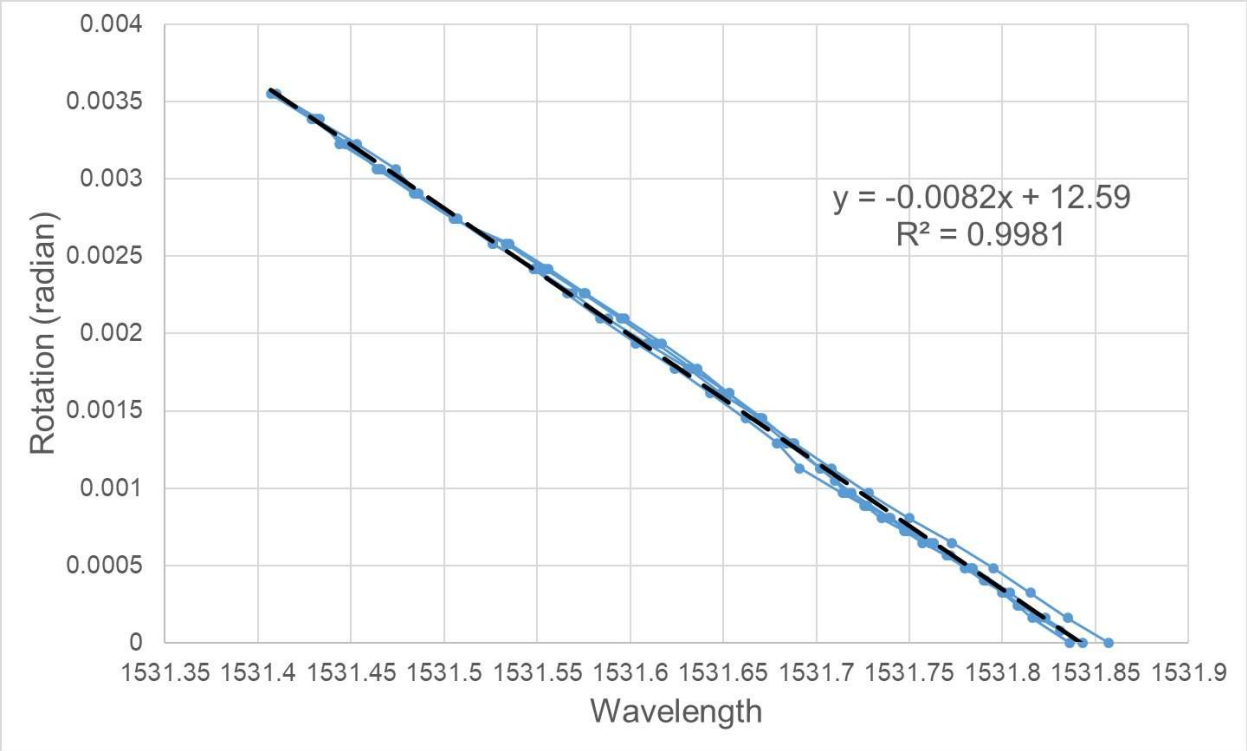

Figure 4.10 Rotation sensor calibration results

4.4. Field Tests

The rotation and wheel sensors were installed at a bridge site in Lagrange, Georgia. Following the installation of the system, a series of calibration tests were performed. The performance of the system was then evaluated by comparing the results from the proposed BWIM system with the existing WIM system at the site.

4.4.1 Description of the Bridge

The bridge with the proposed BWIM system is located about 6 km (3.7 mi) to the east of LaGrange, GA. This bridge carries the southbound traffic of Interstate 85 over Greenville road. The superstructure of this four-span bridge consists of composite steel girders. The first and last spans are simply supported. However, the two middle spans are continuous. The first and fourth spans are 15.24 m (50 ft) long and the second and third spans are 25.14 m (82.5 ft) long.

The substructure, including the piers and abutments, have a 27-degree skew from the axis perpendicular to the bridge layout line. Wide flange 36×135 steel girder beams were used for construction of the first and last spans. W36×150 steel girder beams with a 15.8×254×406 mm (5/8×10×16 in) cover plate in the middle (over the third pier) were used for the second and third spans.

The superstructure consists of six girders spaced 2.36 m (7.75 ft) from each other. A36 grade steel was used for the girders in the first and last span and A572 grade 50 steel was used for all the remaining girders in the second and third spans. Figures 4.11 and 4.12 show the bridge with its elevation and sectional views.

Figure 4.11 The subject bridge located in LaGrange, GA

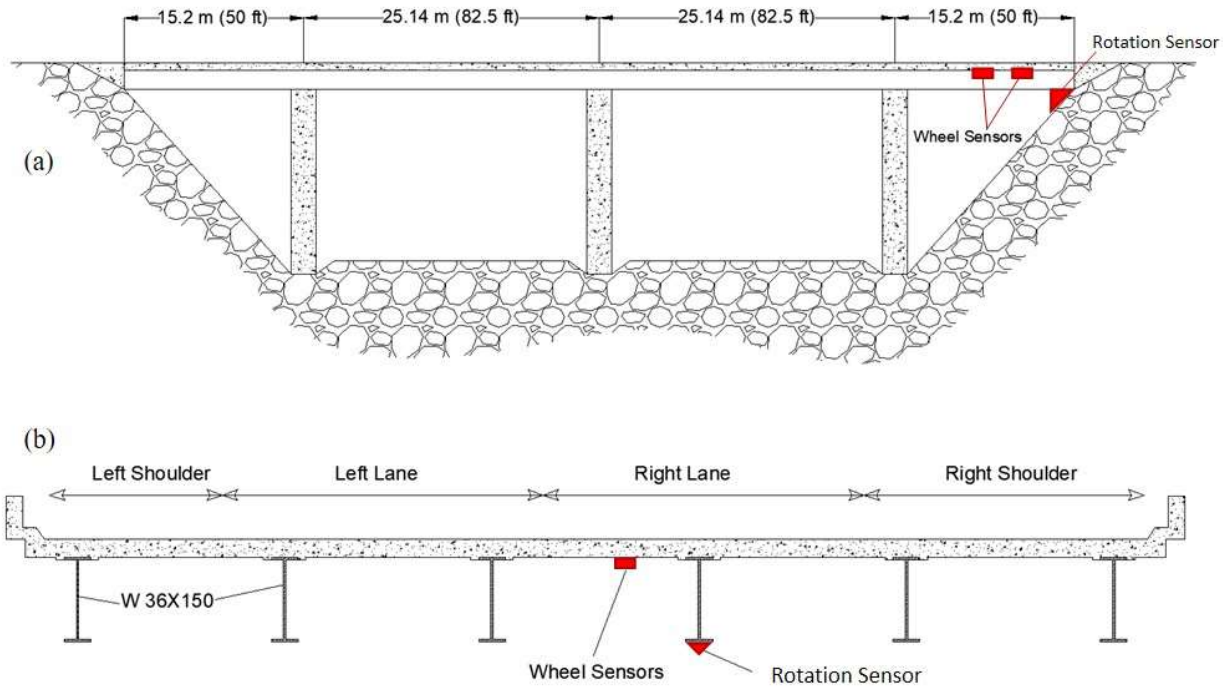

Figure 4.12 Bridge elevation and sectional view

4.4.2 Sensors and Instrumentation

The third girder from the right shoulder was selected for instrumentation because it was directly under the right lane where the majority of the heavy vehicles, including trucks, were passing over. Two wheel sensors were installed at a distance of 1.21 m (4 ft) and 2.74 m (9 ft) from the abutment. They were directly attached under the deck and between the main girders. The wheel sensors consist of FBG strain sensors which had gauge lengths of 75 mm (3 in), strain limitation of ± 2500 με and sensitivity of 1.4 pm/με. The proposed rotation sensor was installed under the girder at the abutment connecting

the girder flange to the bearings. Figures 4.14 to 4.16 depict the installed sensors with the data acquisition devices installed in the NEMA rated enclosure.

Figure 4.13 Rotation sensor installed on the bridge

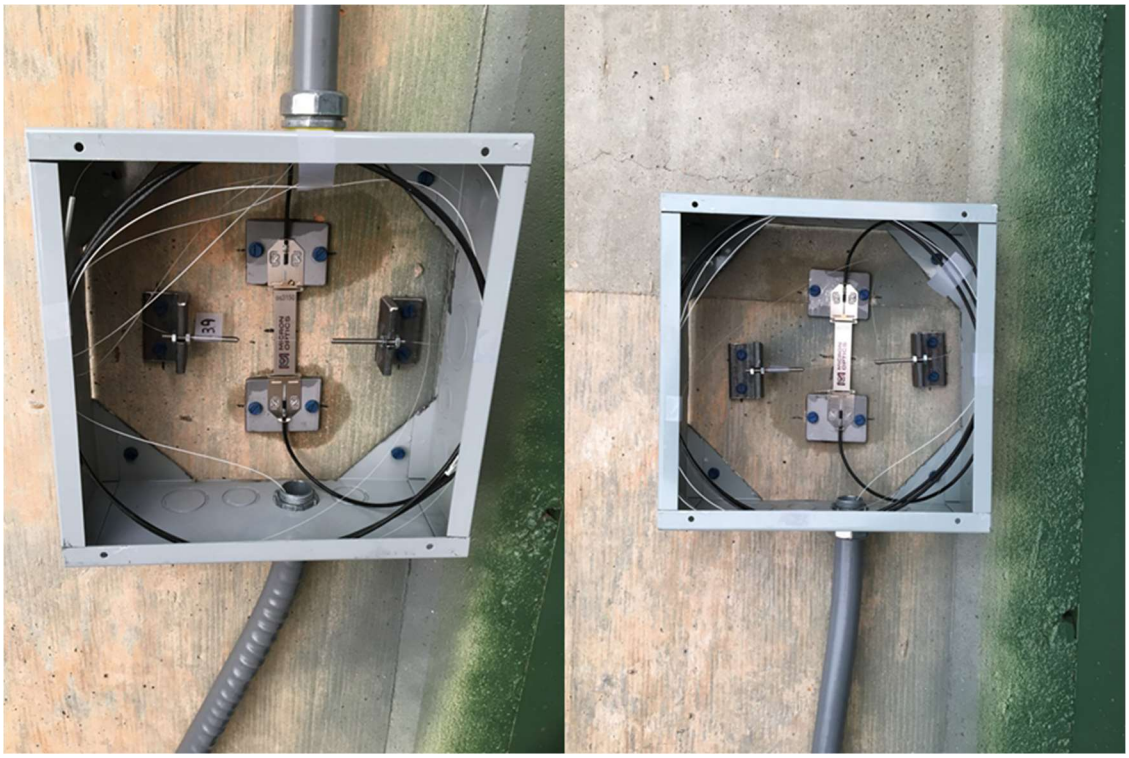

Figure 4.14 Rotation and wheel sensors

Figure 4.15 Location of wheel sensors

Figure 4.16 Site interrogation unit and processor within the NEMA enclosure

4.4.3 Test Program

The rotational influence line of the abutment is calculated from the effect of a unit load moving over the bridge. The constant parameters used to develop the rotational influence line are modulus of elasticity and moment of inertia of the section which are related to the geometric and material properties of the bridge. These two parameters can be calculated theoretically by classical mechanics. However, the more realistic approach

is to obtain them by calibration tests. The series of calibration tests take into consideration changes in material properties and composite action of the superstructure.

The test program is conducted in two phases. The first phase is the calibration tests and the second phase is the validation tests. In the calibration process, 4 trucks with known axle weights and axle spacing were passed through the desired lane and the responses of the bridge were recorded. Having known the rotation at the abutment and the axle loads, the influence line was calculated and calibrated accordingly. Table 4.1 contains the information on the calibration trucks including the axle weights and spacing.

Table 4.1 CALIBRATION TRUCKS AXLE WEIGHTS

Truck Number	1st Axle Weight (lbs)	2nd Axle Group Weight (lbs)	3rd Axle Group Weight (lbs)	Gross Vehicle Weight (GVW) (lbs)
Truck 1	11000	22500	13500	47000
Truck 2	11500	31200	28600	71400
Truck 3	10000	22200	20400	52700
Truck 4	10700	20900	14300	45900

In the second phase, a total number of 10 trucks with known axle weight and spacing were passed over the bridge. This set of runs were used to validate the accuracy of the installed system based on the calibration of the first phase.

4.4.4 Field Test Results

An example of the recorded data from all sensors for one passing truck is shown in figure 14. The rotation sensor readings are plotted on a secondary axis located on the

right side of the plot. The continuous black line pertains to the changes of rotation in radians at the abutment where the rotation sensor is installed. This line is the filtered recorded data to reduce the existing noise from the rotation sensor. The process of noise reduction was performed by applying the moving average technique over the original recorded data shown in continuous gray line. The dashed black line is the readings of wheel sensor B and the dashed gray line is the measurements of wheel sensor A.

The arrival times of the first and second axles to wheel sensors B and A are illustrated in figure 4.17 as T_{B1}, T_{B2}, T_{A1} and T_{A2} respectively. The rotations at the abutment corresponding to the indicated times are also marked in the figure.

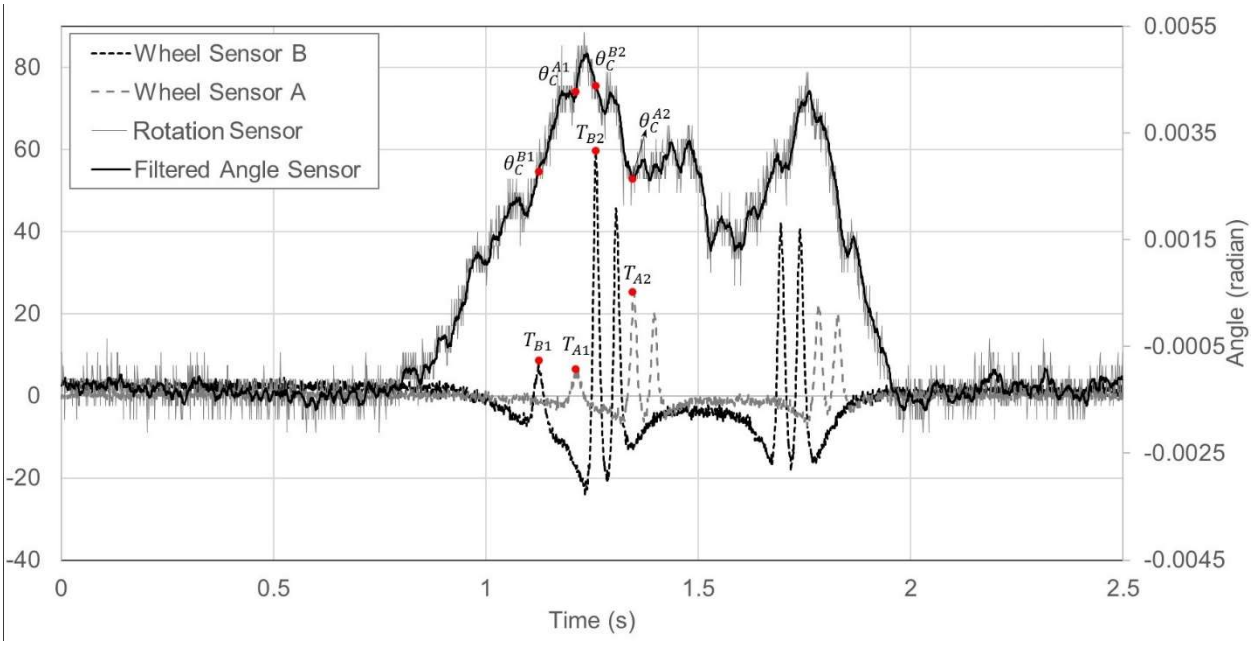

Figure 4.17 Recorded data from rotation and wheel sensors for a passing truck

Upon completion of the calibration of the BWIM system, validation of the measurements was accomplished by comparing the acquired BWIM data with the known truck weight data. The following tables includes the 10 runs used for this purpose. The individual axle weights are calculated and the results are represented as a difference in error.

Table 4.2 VALIDATION RESULTS OF THE TEST TRUCKS FOR FIRST AXLES

Pass Number	1st Axle Weight (lbs)	Measured 1st Axle Weight	Percent Error
Run 1	10740	11418.8	6.32
Run 2	11000	11050.3	0.46
Run 3	11200	9571.5	-14.54
Run 4	12800	10983.1	-14.19
Run 5	10600	12342.0	16.43
Run 6	11300	9857.1	-12.77
Run 7	12300	10448.3	-15.05
Run 8	11400	12024.0	5.47
Run 9	11100	11189.0	0.80
Run 10	11300	10494.5	-7.13

Table 4.3 VALIDATION RESULTS OF THE TEST TRUCKS FOR SECOND AXLES

Pass Number	2nd Axle Group Weight (lbs)	Measured 2nd Axle Group Weight	Percent Error
Run 1	21100	19367.7	-8.21
Run 2	18400	17139.9	-6.85
Run 3	27000	28278.5	4.74
Run 4	34700	34961.7	0.75
Run 5	28800	24937.0	-13.41
Run 6	31900	28278.5	-11.35
Run 7	33300	31620.1	-5.04
Run 8	25500	21595.4	-15.31
Run 9	15700	16026.1	2.08
Run 10	17100	17139.9	0.23

Table 4.4 VALIDATION RESULTS OF THE TEST TRUCKS FOR THIRD AXLES

Pass Number	3rd Axle Group Weight (lbs)	Measured 3rd Axle Group Weight	Percent Error
Run 1	15200	14129.8	-7.04
Run 2	17200	16558.5	-3.73
Run 3	27000	27487.6	1.81
Run 4	31500	33559.3	6.54
Run 5	29700	29916.2	0.73
Run 6	34600	33559.3	-3.01
Run 7	31200	32344.9	3.67
Run 8	25700	21415.8	-16.67
Run 9	11400	12915.4	13.29
Run 10	16700	15344.1	-8.12

Table 4.5 VALIDATION RESULTS OF THE TEST TRUCKS FOR GROSS VEHICLE WEIGHTS

Pass Number	Gross Vehicle Weight (GVW) (lbs)	Measured GVW (lbs)	Percent Error
Run 1	47100	44916.2	-4.64
Run 2	46600	44748.7	-3.97
Run 3	65300	65337.7	0.06
Run 4	79000	79504.1	0.64
Run 5	69200	67195.2	-2.90
Run 6	77700	71694.9	-7.73
Run 7	76800	74413.3	-3.11
Run 8	62600	55035.2	-12.08
Run 9	38300	40130.5	4.78
Run 10	45200	42978.5	-4.91

The average calculated errors for the first, second, third axle group and gross vehicle weight are -3.42, -5.23, -1.23 and -3.38 percent respectively. The maximum standard deviation of errors corresponds to the first axle groups with 10.9 percent. This value decreases to 6.9 and 8.4 percent for second and third axle groups. The standard deviation of gross vehicle weights is calculated as 4.64 percent.

As it is shown in the tables, the largest portion of the errors is related to the first axle weight calculation. However, this error is compensated by the other axle group measurements. Considering the final GVW calculations, an average error of -3.38 percent with standard deviation of 4.64 percent shows the acceptable accuracy of the proposed

methods. Other than run number 8, the individual errors corresponding to GVW are less than 8 percent. The results of axle space and speed detection for all the 10 runs are provided in Table 4.6.

Table 4.6 AXLE SPACING AND SPEED DETECTION RESULTS

Pass Number	Axle Space 1 (ft)	Axle Space 2 (ft)	Calculated Space 1 (ft)	Calculated Space 2 (ft)	Axle space 1 error(%)	Axle space 2 error(%)	Speed (mph)
Run 1	20	33.35	19.95	33.4	-0.25	0.15	64
Run 2	14.95	38	15.1	38.4	1.00	1.05	60
Run 3	20.4	20	20.45	20.25	0.25	1.25	67
Run 4	19.75	40.85	19.75	40.75	0.00	-0.24	58
Run 5	19.35	37.7	19.2	37.3	-0.78	-1.06	60
Run 6	19.35	37.05	19.4	37.05	0.26	0.00	64
Run 7	19.25	33.25	19.5	34.05	1.30	2.41	63
Run 8	19.4	35.05	19.8	36	2.06	2.71	68
Run 9	20	36.65	20.15	37.05	0.75	1.09	61
Run 10	19.25	36.8	19.2	36.5	-0.26	-0.82	59

The effects of tandem axles were not obvious on the rotational response of the proposed method on the bridge. However tandem axles were detected as group axles. There are several factors attributed to the recognition of tandem axles including tandem axle spacing, vehicle speed, tandem axle weight and bridge stiffness. Increasing the acquisition frequency may lead to the recognition of individual axles. However, the system noise will increase, and general accuracy of the system may decrease.

4.5. Summary of the chapter

The proposed method in this chapter pertains to a modified bridge weigh-in-motion technology. The method utilizes rotational response of the bridge at the abutment for calculation and estimation of individual and gross vehicle weights.

Changes of rotation at the abutments were measured by a fabricated new sensor called rotation sensor. The stain in the mid-section of the arc rotation sensor were related to the deformations at its both ends. Two fiber Bragg grating sensors are attached to the main beam of the rotation sensor and gives the system the sensing ability. One of the sensors is used for strains measurement and the other is used for temperature compensation. The system consists of the combination of one rotation sensor at the abutment with two wheel sensors under the deck.

The proposed modified bridge weigh in motion system was verified by testing it on a full scale bridge in LaGrange, GA. This experiment included multiple runs of calibrated trucks over the bridge for axle weight and GWV comparison. Calculated gross vehicle weights and known GVWs were compared and the results illustrated an average error and standard deviation of less than 5 percent. Classification of all truck including the axle spacing and truck speeds were achieved with an error of less than 3 percent.

Chapter 5 . CONCLUSIONS

The work presented in this thesis starts with a method corresponding to development of an application for detection of cracks in bridges by Brillouin scattering based distributed sensors. The proposed method does not require measurements in the state of the bridge that it is not subjected to dynamic or static loads. Identification of damage beyond the signal to noise limits of the instrument is achieved by normalization of the measured distributed strains during multiple positions of a truck with respect to the theoretical influence line of the bridge. Formulation of the method leads to the introduction of a damage index for identification of crack locations along the length of the Bridge. The effectiveness of the proposed method was verified by load testing of a five span continuous precast post-tensioned concrete box girder bridge. An ordinary telecommunication grade optical fiber was employed for monitoring the damage along the entire 332-meter length of the Bridge. Analysis of the load test results based on the proposed method led to the identification of five locations with anomalies. Visual inspection of the Bridge verified locations of two microcracks, and three misaligned sections at the shear keys of the box segments. Brillouin scattering based measurements are strain based and their response to cracks and other stress raisers such as misalignments between sections of the box girder are manifested by strain intensities. Therefore, they cannot differentiate between cracks and other issues unrelated to damage. Because of the inherent noise associated with Brillouin measurements, larger loads amplify the strain amplitudes and enhance the damage detection resolution of the system. The method proposed herein was not verified for implementation in single span

bridges. However, it is envisioned that the same approach can be employed for such bridges by placement of loads at multiple positions in the single span.

The proposed method in chapter 2 was further developed for application of dynamic loads in the third chapter. This method also utilizes Brillouin Optical Time Domain Analysis technique to measure distributed strains along the structure. The main advantage of this method is that traffic stoppage or lane closure is not required for proper performance of the method. Detection of micro-cracks with induced strains is achieved by calculating the strain differentials in theory and measurement field. The damage index developed in the seconds chapter is also used for detection of micro-cracks in this chapter. For random traffic loads with no information on the loading, variances of the strain differentials over time is set to be the indicator of presence of cracks. The applicability of the method was verified by dynamic load testing on a five-span continuous precast post-tensioned concrete box girder bridge and a three-span continuous steel girder bridge. Analysis of the results led to probable location of damages. Visual inspections were performed on both bridges for verification purposes. Sampling points with highest crack index values in Kishwaukee bridge corresponded to a micro-crack and three sectional misalignments. Highest values of the strains differentials in Thornton Quarry bridge were verified to be three micro cracks. However, the method failed to detect one micro crack located on Thornton Quarry bridge. The proposed method illustrated acceptable performance in detecting micro crack under dynamic loads. However, measurement pool should contain enough random traffic runs for a robust crack detection performance.

In chapter 4, a method was proposed pertaining to live load determination of bridges. This method is a modified bridge weigh-in-motion technology which utilizes rotational response of the bridge at the abutment for calculation and estimation of individual and gross vehicle weights. Measurement of rotation changes due to various GVWs are conducted by a proposed rotation sensor. The rotation sensor relates the displacements and rotations at both ends to their relative strain at the center of the sensor. The sensing capability of the arch sensor comes from the two FBGs installed under the center of the arch beams. Measurement of strains due to rotation changes are recorded with the main FBG and the temperature compensation is performed by the second FBG attached to the cantilever beam section of the rotation sensor. Calibration of the sensor is performed by multiple cyclic loading of the rotation sensor in the lab and the relation between the changes of rotation to changes of FBG wavelength is recorded with this test. The applicability of the proposed BWIM method was tested by conducting a full-scale experiment on a four span steel girder bridge in LaGrange, GA. The test included a series of truck runs for system calibration and a second series of truck runs for validation purposes. The comparison between the calculated GVWs and known GVWs indicated an average error of -3.38% with standard deviation of 4.64%. with a maximum error of 12.08%. All the trucks were classified correctly, and all the individual axles were detected by the wheel sensors. The proposed system however needs to be further tested on different types of bridges. Other factors like size, stiffness of the bridge and multiple lane loading may also effect the performance of the method.

CITED LITERATURE

Abdoli Oskoui, E., Taylor, T., & Ansari, F. (2019). Method and monitoring approach for distributed detection of damage in multi-span continuous bridges. *Engineering Structures,189*, 385-395. doi:10.1016/j.engstruct.2019.02.037

Alani, A. M., Aboutalebi, M., & Kilic, G. (2013). Applications of ground penetrating radar (GPR) in bridge deck monitoring and assessment. *Journal of Applied Geophysics,97*, 45-54. doi:10.1016/j.jappgeo.2013.04.009

Alani, A. M., Aboutalebi, M., & Kilic, G. (2014). Integrated health assessment strategy using NDT for reinforced concrete bridges. *NDT & E International,61*, 80-94. doi:10.1016/j.ndteint.2013.10.001

Algohi, B., Mufti, A., & Thomson, D. (2018). Detection of speed and axle configuration of moving vehicles using acoustic emission. *Journal of Civil Structural Health Monitoring,8*(3), 353-362. doi:10.1007/s13349-018-0281-8

Angulo-Vinuesa, X., Martin-Lopez, S., Corredera, P., & Gonzalez-Herraez, M. (2012). Raman-assisted Brillouin optical time-domain analysis with sub-meter resolution over 100 km. *Optics Express,20*(11), 12147. doi:10.1364/oe.20.012147

Ansari, F. (2009). Fiber optic sensors for structural health monitoring of civil infrastructure systems. *Structural Health Monitoring of Civil Infrastructure Systems,*260-282. doi:10.1533/9781845696825.1.260

Atkan E., Catbas, N., Grimmelsman, and Pervizpour, K., (2003). Development of a Model Health Monitoring Guide for Major Bridges., *Drexel Intelligent Infrastructure and Transportation Safety Institute*, http://www.di3.drexel.edu (read: 2007-02-20)

Azari, H., Nazarian, S., & Yuan, D. (2014). Assessing sensitivity of impact echo and ultrasonic surface waves methods for nondestructive evaluation of concrete structures. *Construction and Building Materials,71*, 384-391. doi:10.1016/j.conbuildmat.2014.08.056

Bao, T., Babanajad, S. K., Taylor, T., & Ansari, F. (2016). Generalized Method and Monitoring Technique for Shear-Strain-Based Bridge Weigh-in-Motion. *Journal of Bridge Engineering,21*(1), 04015029. doi:10.1061/(asce)be.1943-5592.0000782

Bao, X., Webb, D. J., & Jackson, D. A. (1993). 22-km distributed temperature sensor using Brillouin gain in an optical fiber. *Optics Letters,18*(7), 552. doi:10.1364/ol.18.000552

Bao, X., & Chen, L. (2011). Recent Progress in Brillouin Scattering Based Fiber Sensors. *Sensors,11*(4), 4152-4187. doi:10.3390/s110404152

Barnes, C. L., & Trottier, J. (2000). Ground-Penetrating Radar for Network-Level Concrete Deck Repair Management. *Journal of Transportation Engineering,126*(3), 257-262. doi:10.1061/(asce)0733-947x(2000)126:3(257)

Bastianini, F., Rizzo, A., Galati, N., Deza, U., & Nanni, A. (2005). Discontinuous Brillouin strain monitoring of small concrete bridges: Comparison between near-to-surface and smart FRP fiber installation techniques. *Smart Structures and Materials 2005: Sensors and Smart Structures Technologies for Civil, Mechanical, and Aerospace Systems*. doi:10.1117/12.594760

Bedon, C., & Morassi, A. (2014). Dynamic testing and parameter identification of a base-isolated bridge. *Engineering Structures,60*, 85-99. doi:10.1016/j.engstruct.2013.12.017

Brencich, A., & Sabia, D. (2008). Experimental identification of a multi-span masonry bridge: The Tanaro Bridge. *Construction and Building Materials,22*(10), 2087-2099. doi:10.1016/j.conbuildmat.2007.07.031

Brownjohn, J. M., Stefano, A. D., Xu, Y., Wenzel, H., & Aktan, A. E. (2011). Vibration-based monitoring of civil infrastructure: Challenges and successes. *Journal of Civil Structural Health Monitoring,1*(3-4), 79-95. doi:10.1007/s13349-011-0009-5

Cawley, P., & Adams, R. (1988). The mechanics of the coin-tap method of non-destructive testing. *Journal of Sound and Vibration,122*(2), 299-316. doi:10.1016/s0022-460x(88)80356-0

Chang, P. C., Flatau, A., & Liu, S. C. (2003). Review Paper: Health Monitoring of Civil Infrastructure. *Structural Health Monitoring: An International Journal,2*(3), 257-267. doi:10.1177/1475921703036169

Chatterjee, P., Obrien, E., Li, Y., & González, A. (2006). Wavelet domain analysis for identification of vehicle axles from bridge measurements. *Computers & Structures,84*(28), 1792-1801. doi:10.1016/j.compstruc.2006.04.013

Cruz, P. J., Topczewski, L., Fernandes, F. M., Trela, C., & Lourenço, P. B. (2010). Application of radar techniques to the verification of design plans and the detection of defects in concrete bridges. *Structure and Infrastructure Engineering,6*(4), 395-407. doi:10.1080/15732470701778506

Cunha, A., Caetano, E., Magalhães, F., & Moutinho, C. (2012). Recent perspectives in dynamic testing and monitoring of bridges. *Structural Control and Health Monitoring,20*(6), 853-877. doi:10.1002/stc.1516

Davis, A. G. (2003). The nondestructive impulse response test in North America: 1985–2001. *NDT & E International,36*(4), 185-193. doi:10.1016/s0963-8695(02)00065-8

Deesomsuk, T., & Pinkaew, T. (2010). Evaluation of effectiveness of vehicle weight estimations using bridge weigh-in-motion. *The IES Journal Part A: Civil & Structural Engineering,3*(2), 96-110. doi:10.1080/19373260903520137

Duffó, G. S., & Farina, S. B. (2009). Development of an embeddable sensor to monitor the corrosion process of new and existing reinforced concrete structures. *Construction and Building Materials,23*(8), 2746-2751. doi:10.1016/j.conbuildmat.2009.04.001

Dumoulin, C., Karaiskos, G., Sener, J., & Deraemaeker, A. (2014). Online monitoring of cracking in concrete structures using embedded piezoelectric transducers. *Smart Materials and Structures,23*(11), 115016. doi:10.1088/0964-1726/23/11/115016

Elsener, B., Andrade, C., Gulikers, J., Polder, R., & Raupach, M. (2003). Half-cell potential measurements—Potential mapping on reinforced concrete structures. *Materials and Structures,36*(7), 461-471. doi:10.1007/bf02481526

Estes, A. C., & Frangopol, D. M. (2003). Updating Bridge Reliability Based on Bridge Management Systems Visual Inspection Results. *Journal of Bridge Engineering,8*(6), 374-382. doi:10.1061/(asce)1084-0702(2003)8:6(374)

Feng, D., & Feng, M. Q. (2015). Model Updating of Railway Bridge Using In Situ Dynamic Displacement Measurement under Trainloads. *Journal of Bridge Engineering,20*(12), 04015019. doi:10.1061/(asce)be.1943-5592.0000765

Feng, X., Zhou, J., Sun, C., Zhang, X., & Ansari, F. (2013). Theoretical and Experimental Investigations into Crack Detection with BOTDR-Distributed Fiber Optic Sensors. *Journal of Engineering Mechanics,139*(12), 1797-1807. doi:10.1061/(asce)em.1943-7889.0000622

Garboczi, E., Schwartz, L., & Bentz, D. (1995). Modeling the influence of the interfacial zone on the DC electrical conductivity of mortar. *Advanced Cement Based Materials,2*(5), 169-181. doi:10.1016/1065-7355(95)90001-2

Gentile, C. (2006). Modal and structural identification of a R.C. arch bridge. *Structural Engineering and Mechanics,22*(1), 53-70. doi:10.12989/sem.2006.22.1.053

Glisic, B., & Inaudi, D. (2003). Integration of long-gage fiber optic sensor into a fiber-reinforced composite sensing tape. *Smart Structures and Materials 2003: Smart Sensor Technology and Measurement Systems*. doi:10.1117/12.484262

Glisic, B., & Inaudi, D. (2010). Distributed Fiber-Optic Sensing and Integrity Monitoring. *Transportation Research Record: Journal of the Transportation Research Board,2150*(1), 96-102. doi:10.3141/2150-12

Glišić, B., & Inaudi, D. (2007). Fibre Optic Methods for Structural Health Monitoring. doi:10.1002/9780470517819

Goldfeld, Y., & Klar, A. (2013). Damage Identification in Reinforced Concrete Beams Using Spatially Distributed Strain Measurements. *Journal of Structural Engineering,139*(12), 04013013. doi:10.1061/(asce)st.1943-541x.0000795

Grosse, C., Reinhardt, H., Krüger, M., Beutel, R. (2013) Application of Impact-Echo Techniques for Crack Detection and Crack Parameter Estimation in Concrete, ICF11, Italy

Hashim, H., Ibrahim, Z., & Razak, H. A. (2013). Dynamic characteristics and model updating of damaged slab from ambient vibration measurements. *Measurement, 46*(4), 1371-1378. doi:10.1016/j.measurement.2012.11.043

He, W., Deng, L., Shi, H., Cai, C. S., & Yu, Y. (2017). Novel Virtual Simply Supported Beam Method for Detecting the Speed and Axles of Moving Vehicles on Bridges. *Journal of Bridge Engineering,22*(4), 04016141. doi:10.1061/(asce)be.1943-5592.0001019

Helmi, K., Taylor, T., & Ansari, F. (2014). Shear force–based method and application for real-time monitoring of moving vehicle weights on bridges. *Journal of Intelligent Material Systems and Structures,26*(5), 505-516. doi:10.1177/1045389x14529612

Hoła, J., & Schabowicz, K. (2010). State-of-the-art non-destructive methods for diagnostic testing of building structures – anticipated development trends. *Archives Of Civil And Mechanical Engineering*, *10*(3), 5-18. doi: 10.1016/s1644-9665(12)60133-2

Ismail, Z., Ibrahim, Z., Ong, A. Z., & Rahman, A. G. (2012). Approach to Reduce the Limitations of Modal Identification in Damage Detection Using Limited Field Data for Nondestructive Structural Health Monitoring of a Cable-Stayed Concrete Bridge. *Journal of Bridge Engineering,17*(6), 867-875. doi:10.1061/(asce)be.1943-5592.0000353

Jacob, B., & Loo, H. V. (2013). Weigh-in-motion for enforcement in Europe. *International Conference on Heavy Vehicles HVParis 2008,*25-38. doi:10.1002/9781118623305.ch1

Kishida, K., Li, C., & Nishiguchi, K. (2005). Pulse pre-pump method for cm-order spatial resolution of BOTDA. *17th International Conference on Optical Fibre Sensors*. doi:10.1117/12.624259

Kishida, K., Li, C., Mizutani, T., & Takeda, N. (2008). PPP-BOTDA for 2 cm spatial resolution in fiber optics distributed sensing. *Proceedings of SPIE*. doi:10.1117/12.801315

Lansdell, A., Song, W., & Dixon, B. (2017). Development and testing of a bridge weigh-in-motion method considering nonconstant vehicle speed. *Engineering Structures,152*, 709-726. doi:10.1016/j.engstruct.2017.09.044

Law, S. S., Chan, T. H., & Zeng, Q. H. (1999). Moving Force Identification—A Frequency and Time Domains Analysis. *Journal of Dynamic Systems, Measurement, and Control,121*(3), 394. doi:10.1115/1.2802487

Li, C. H., Guzik, A., and Kishida, K. (2010) The high-performance BOTDA based systems for distributed strain sensing. *The 3rd International Forum on Opto-electronic Sensor-based Monitoring in Geo-engineering*, Suzhou, China, 1-10.

Lydon, M., Taylor, S. E., Robinson, D., Mufti, A., & Brien, E. J. (2015). Recent developments in bridge weigh in motion (B-WIM). *Journal of Civil Structural Health Monitoring,6*(1), 69-81. doi:10.1007/s13349-015-0119-6

Manning, D. G., & Masliwec, T. (1990). Application of Radar and Thermography to Bridge Deck Condition Surveys. *Bridge Management,*305-317. doi:10.1007/978-1-4899-7232-3_27

Matta, F., Bastianini, F., Galati, N., Casadei, P., & Nanni, A. (2008). Distributed Strain Measurement in Steel Bridge with Fiber Optic Sensors: Validation through Diagnostic Load Test. *Journal of Performance of Constructed Facilities,22*(4), 264-273. doi:10.1061/(asce)0887-3828(2008)22:4(264)

Meng, D., Ansari, F., & Feng, X. (2015). Detection and monitoring of surface micro-cracks by PPP-BOTDA. *Applied Optics,54*(16), 4972. doi:10.1364/ao.54.004972

Motamedi, M. H., Feng, X., Zhang, X., Sun, C., & Ansari, F. (2012). Quantitative investigation in distributed sensing of structural defects with Brillouin optical time domain reflectometry. *Journal of Intelligent Material Systems and Structures,24*(10), 1187-1196. doi:10.1177/1045389x12470309

Moses, F. (1979). Weigh-in-motion system using instrumented bridges. *Transportation Engineering Journal,* 105(3), 233–249.

Moses, F., and Ghosn, M. (1983). Instrumentation for weight trucks in motion for high bridge loads. *Final Rep. No. FHWA/OH-83/001, Federal Highway Administration*, Ohio Dept. of Transportation, Columbus, OH.

Mufti, A., Thomson, D., Inaudi, D., Vogel, H. M., & Mcmahon, D. (2011). Crack detection of steel girders using Brillouin optical time domain analysis. *Journal of Civil Structural Health Monitoring,1*(3-4), 61-68. doi:10.1007/s13349-011-0006-8

Mufti, A., Oshima, T., Bakht, B., Mohamed A. Mohamedien, M., A., (2006) SHM Glossary of Terms: Definitions, *Homepage of International Society for Structural Health Monitoring of Intelligent Infrastructure*.

Nazarian, E., Ansari, F., Zhang, X., & Taylor, T. (2016). Detection of Tension Loss in Cables of Cable-Stayed Bridges by Distributed Monitoring of Bridge Deck Strains. *Journal of Structural Engineering,142*(6), 04016018. doi:10.1061/(asce)st.1943-541x.0001463

Obrien, E. J., Quilligan, M. J., & Karoumi, R. (2006). Calculating an influence line from direct measurements. *Proceedings of the Institution of Civil Engineers - Bridge Engineering,159*(1), 31-34. doi:10.1680/bren.2006.159.1.31

O'Brien, E. J., Hajializadeh, D., Uddin, N., Robinson, D., and Opitz, R. (2012). Strategies for axle detection in bridge weigh-in-motion systems. *Proceedings of the 6th International Conference on Weigh-in-Motion*, Wiley, Hoboken, NJ, 79–88.

Ojio, T., and Yamada, K. (2002). Bridge weigh-in-motion systems using stringers of plate girder bridges. *Pre-Proceedings of the Third International Conference on Weigh-In-Motion*, 209-218.

Park, S., Stubbs, N., Bolton, R., Choi, S., & Sikorsky, C. (2001). Field Verification of the Damage Index Method in a Concrete Box-Girder Bridge via Visual Inspection. *Computer-Aided Civil and Infrastructure Engineering,16*(1), 58-70. doi:10.1111/0885-9507.00213

Peters, RJ. (1986) Culway – an unmanned and undetectable highway speed vehicle weighing system. *Proceedings of the 13th AARB conference*, vol. 13(6), 70–83.

Pinkaew, T. (2006). Identification of vehicle axle loads from bridge responses using updated static component technique. *Engineering Structures,28*(11), 1599-1608. doi:10.1016/j.engstruct.2006.02.012

Qin, L., Lu, Y., & Li, Z. (2010). Embedded Cement-Based Piezoelectric Sensors for Acoustic Emission Detection in Concrete. *Journal of Materials in Civil Engineering,22*(12), 1323-1327. doi:10.1061/(asce)mt.1943-5533.0000133

Regier, R., & Hoult, N. A. (2014). Distributed Strain Behavior of a Reinforced Concrete Bridge: Case Study. *Journal of Bridge Engineering,19*(12), 05014007. doi:10.1061/(asce)be.1943-5592.0000637

Rens, K., Wipf, T., & Klaiber, F. (1997). Review of Nondestructive Evaluation Techniques of Civil Infrastructure. *Journal Of Performance Of Constructed Facilities*, *11*(4), 152-160. doi: 10.1061/(asce)0887-3828(1997)11:4(152)

Robert-Nicoud, Y., Raphael, B., Burdet, O., & Smith, I. F. (2005). Model Identification of Bridges Using Measurement Data. *Computer-Aided Civil and Infrastructure Engineering,20*(2), 118-131. doi:10.1111/j.1467-8667.2005.00381.x

Rowley, C. W., Obrien, E. J., Gonzalez, A., & Žnidarič, A. (2008). Experimental Testing of a Moving Force Identification Bridge Weigh-in-Motion Algorithm. *Experimental Mechanics,49*(5), 743-746. doi:10.1007/s11340-008-9188-3

Scarella, A., Salamone, G., Babanajad, S. K., Stefano, A. D., & Ansari, F. (2017). Dynamic Brillouin Scattering–Based Condition Assessment of Cables in Cable-Stayed Bridges. *Journal of Bridge Engineering,22*(3), 04016130. doi:10.1061/(asce)be.1943-5592.0001010

Scott, M., Rezaizadeh, A., Delahaza, A., Santos, C., Moore, M., Graybeal, B., & Washer, G. (2003). A comparison of nondestructive evaluation methods for bridge deck assessment. *NDT & E International,36*(4), 245-255. doi:10.1016/s0963-8695(02)00061-0

Sekiya, H., Kubota, K., & Miki, C. (2018). Simplified Portable Bridge Weigh-in-Motion System Using Accelerometers. *Journal of Bridge Engineering,23*(1), 04017124. doi:10.1061/(asce)be.1943-5592.0001174

Spencer, B. F., & Cho, S. (2011) Wireless smart sensor technology for monitoring civil infrastructure: technological developments and full-scale applications. *Proceedings of the World Congress on Advances in Structural Engineering and Mechanics*. Seoul, Republic of Korea

Stradiotto, N. R., Yamanaka, H., & Zanoni, M. V. (2003). Electrochemical sensors: A powerful tool in analytical chemistry. *Journal of the Brazilian Chemical Society,14*(2), 159-173. doi:10.1590/s0103-50532003000200003

Taki, M., Soto, M. A., Bolognini, G., & Pasquale, F. D. (2013). Study of Raman amplification in DPP-BOTDA sensing employing Simplex coding for sub-meter scale spatial resolution over long fiber distances. *Measurement Science and Technology,24*(9), 094018. doi:10.1088/0957-0233/24/9/094018

Villalba, V., Villalba, S., & Casas, J. (2012). Application of OBR fiber optic technology in the structural health monitoring of the Can Fatjó Viaduct (Cerdanyola del Vallés - Spain). *Bridge Maintenance, Safety, Management, Resilience and Sustainability Bridge Maintenance, Safety and Management,*498-501. doi:10.1201/b12352-64

Wang, T., & Merrill, T. F. (1988). Stiffness Coefficients of Noncircular Curved Beams. *Journal of Structural Engineering,114*(7), 1689-1699. doi:10.1061/(asce)0733-9445(1988)114:7(1689)

Wardhana, K., & Hadipriono, F. C. (2003). Analysis of Recent Bridge Failures in the United States. *Journal of Performance of Constructed Facilities,17*(3), 144-150. doi:10.1061/(asce)0887-3828(2003)17:3(144)

Yehia, S., Abudayyeh, O., Nabulsi, S., & Abdelqader, I. (2007). Detection of Common Defects in Concrete Bridge Decks Using Nondestructive Evaluation Techniques. *Journal of Bridge Engineering,12*(2), 215-225. doi:10.1061/(asce)1084-0702(2007)12:2(215)

Yi, T., Li, H., & Gu, M. (2013). Experimental assessment of high-rate GPS receivers for deformation monitoring of bridge. *Measurement,46*(1), 420-432. doi:10.1016/j.measurement.2012.07.018

Yu, L., & Chan, T. H. (2007). Recent research on identification of moving loads on bridges. *Journal of Sound and Vibration,305*(1-2), 3-21. doi:10.1016/j.jsv.2007.03.057

Yu, Y., Cai, C., & Deng, L. (2016). State-of-the-art review on bridge weigh-in-motion technology. *Advances in Structural Engineering,19*(9), 1514-1530. doi:10.1177/1369433216655922

Zhao, H., Uddin, N., Shao, X., Zhu, P., & Tan, C. (2014). Field-calibrated influence lines for improved axle weight identification with a bridge weigh-in-motion system. *Structure and Infrastructure Engineering,11*(6), 721-743. doi:10.1080/15732479.2014.904383

Zhao, X., Lu, J., Han, R., Kong, X., Wang, Y., & Li, L. (2012). Application of Multiscale Fiber Optical Sensing Network Based on Brillouin and Fiber Bragg Grating Sensing Techniques on Concrete Structures. *International Journal of Distributed Sensor Networks,8*(10), 310797. doi:10.1155/2012/310797

Zhu, X., & Law, S. (2006). Moving load identification on multi-span continuous bridges with elastic bearings. *Mechanical Systems and Signal Processing,20*(7), 1759-1782. doi:10.1016/j.ymssp.2005.06.004

Znidaric A, Kalin J, Lavric I. (2002) Bridge Weigh-in-Motion Measurements on Short Slab Bridges without Axle Detectors. *Pre-proceedings of the third international conference on weigh-in-motion*, 231–239.

Žnidarič, A., Turk, G., & Zupan, E. (2015). Determination of strain correction factors for bridge weigh-in-motion systems. *Engineering Structures,102*, 387-394. doi:10.1016/j.engstruct.2015.08.026

APPENDIX

Here, I present the written permission from the journal of Engineering Structures, for Chapter 2, where I have used my published paper.

Copyright Clearance Center RightsLink®

Home | Create Account | Help

ENGINEERING STRUCTURES

Title: Method and monitoring approach for distributed detection of damage in multi-span continuous bridges

Author: Elias Abdoli Oskoui,Todd Taylor,Farhad Ansari

Publication: Engineering Structures

Publisher: Elsevier

Date: 15 June 2019

© 2019 Elsevier Ltd. All rights reserved.

LOGIN

If you're a copyright.com user, you can login to RightsLink using your copyright.com credentials.

Already a RightsLink user or want to learn more?

Please note that, as the author of this Elsevier article, you retain the right to include it in a thesis or dissertation, provided it is not published commercially. Permission is not required, but please ensure that you reference the journal as the original source. For more information on this and on your other retained rights, please visit: https://www.elsevier.com/about/our-business/policies/copyright#Author-rights

BACK | CLOSE WINDOW

Copyright © 2019 Copyright Clearance Center, Inc. All Rights Reserved. Privacy statement. Terms and Conditions.
Comments? We would like to hear from you. E-mail us at customercare@copyright.com

VITAE

Elias Abdoli Oskoui

Education

2015-2019	**Ph.D. in Civil Engineering**; Structural Engineering Department of Civil and Materials Engineering, University of Illinois at Chicago, Chicago, IL
2010-2012	**Master of Science in Civil Engineering**; Earthquake Engineering Department of Civil Engineering, University of Tehran, Tehran, Iran
2006-2010	**Bachelor of Science in Civil Engineering**; Structural Engineering Department of Civil Engineering, University of Tabriz, Tabriz, Iran

Professional Experience

2015-2019	**Graduate Research Assistant**; Smart Sensors and NDT Laboratory University of Illinois at Chicago, Chicago, IL
2015-2018	**Graduate Teaching Assistant**; Statics (CME 201), Non-Destructive Testing of Concrete Structures (CME 536), Structural Analysis II (CME 409), Design of Steel Structures (CME 301), Engineering Hydrology (CME 427) University of Illinois at Chicago, Chicago, IL
2012-2014	**Structural Designer**; Takin Saz Azma Tabriz, Iran

Publications

- Song, Q., **Abdoli Oskoui, E**., Taylor, T., & Ansari, F. (2018). Visual saliency–based image binarization approach for detection of surface microcracks by distributed optical fiber sensors. *Structural Health Monitoring*, doi:10.1177/1475921718797323
- **Abdoli Oskoui, E**., Taylor, T., & Ansari, F. (2019). Method and Monitoring Approach for Distributed Detection of Damage in Multi-Span Continuous Bridges. *Engineering Structures*. *189*, 385-395. doi:10.1016/j.engstruct.2019.02.037
- **Abdoli Oskoui, E**., Taylor, T., & Ansari, F. (Submitted). Method and Sensor for Monitoring Weight of Trucks in Motion Based on Bridge Girder End Rotations. *Structure and Infrastructure Engineering*.
- **Abdoli Oskoui, E.**, Kani, I.M. (2013). A Modified Equivalent Frame Method for the Analysis of the Flat slabs and Slabs on beams simultaneously subjected to lateral and gravity loads, *4th International Conference on Concrete & Development*, Tehran, Iran
- **Abdoli Oskoui, E.**, Kani, I.M. (2012). An Improved Equivalent Frame Method for the Analysis of Two-way Slab Systems Subjected to Gravity and Lateral Loads, *10th International Congress on Advances in Civil Engineering*, Ankara, Turkey